IRIS SEGMENTATION AND RECOGNITION BASED ON DEEP LEARNING IN THE PRESENCE OF DISEASES

2022
MASTER THESIS
COMPUTER ENGINEERING

Abbadullah .H SALEH

Thesis Advisor
Assist. Prof. Dr. Oğuzhan MENEMENCİOĞLU

IRIS SEGMENTATION AND RECOGNITION BASED ON DEEP LEARNING IN THE PRESENCE OF DISEASES

Abbadullah .H SALEH

T.C.
Karabuk University
Institute of Graduate Programs
Department of Computer Engineering
Prepared as
Master Thesis

Thesis Advisor
Assist. Prof. Dr. Oğuzhan MENEMENCİOĞLU

KARABUK
July 2022

I certify that in my opinion the thesis submitted by Abbadullah .H SALEH titled "IRIS SEGMENTATION AND RECOGNITION BASED ON DEEP LEARNING IN THE PRESENCE OF DISEASES" is fully adequate in scope and in quality as a thesis for the degree of Master of Computer Engineering.

Assist. Prof. Dr. Oğuzhan MENEMENCİOĞLU .....
Thesis Advisor, Department of Computer Engineering

This thesis is accepted by the examining committee with a unanimous vote in the Department of Computer Engineering as a Master of Science thesis. July 4, 2022

Examining Committee Members (Institutions)	Signature
Chairman : Assoc. Prof. Dr. Fatih NAR (AYBU)	.....
Member : Assist. Prof. Dr. Adnan Saher M. AL-AJEELI (KBU)	.....
Member : Assist. Prof. Dr. Oğuzhan MENEMENCİOĞLU (KBU)	.....

The degree of Master of Science by the thesis submitted is approved by the Administrative Board of the Institute of Graduate Programs, Karabuk University.

Prof. Dr. Hasan SOLMAZ .....
Director of the Institute of Graduate Programs

"I declare that all the information within this thesis has been gathered and presented in accordance with academic regulations and ethical principles, and I have, according to the requirements of these regulations and principles, cited all those which do not originate in this work as well."

Abbadullah .H SALEH

ABSTRACT

M. Sc. Thesis

IRIS SEGMENTATION AND RECOGNITION BASED ON DEEP LEARNING IN THE PRESENCE OF DISEASES

Abbadullah .H SALEH

Karabuk University
Institute of Graduate Programs
The Department of Computer Engineering

Thesis Advisor:
Assist. Prof. Dr. Oğuzhan MENEMENCİOĞLU
July 2022, 131 pages

Two main steps are involved in any iris recognition system: iris segmentation and iris recognition. A lot of iris segmentation and recognition systems have been introduced in recent decades. Too little research has focused on eye pathology cases and their effects on iris segmentation and recognition systems. In the current study, a new deep learning-based iris recognition system is introduced in the case of eye disease. A novel dynamic circular Hough transform algorithm is designed and implemented in the iris segmentation step. The transfer learning approach is used to apply three different deep learning models (GoogleNet, ResNet50, and ResNet101) through the recognition step. Three separate datasets are used. The first one is the Warsaw Bio-Base V1 collection which contains 684 iris images of people with various eye disorders. The second dataset is the Warsaw Bio-Base V2 dataset, which has 1793 iris scans with more complex eye cases and a larger number of photos. The third dataset is the CASIA V3

Interval Iris dataset, which has 2639 healthy iris photos. Experiments are conducted under different training and evaluation scenarios.

During those scenarios, many training considerations are taken into account: three deep learning models, different splitting criteria; colored and grayscale iris images; segmented and original iris images, and transfer learning as two layers of training. MATLAB 2020a is used to build all the needed software. Besides that, like deep learning and image processing etc. some toolboxes are used. Many ways are used to check the accuracy of the result models, such as training accuracy, validation accuracy, test accuracy, confusion matrix, TPR, FNR, PPR, FDR, and training duration. The ground truth of iris segmentation is built, and the results indicate a low FPR of 0.79% and an FNR of 5.49% for the Warsaw Bio-Base V1 dataset. Results indicate that GoogleNet has low computational time in all cases, but lower performance compared to ResNet models. However, the best recognition accuracy in scenario No. (6), where iris recognition accuracy is 98.5% and 99% by ResNet50 and ResNet101 respectively for only Warsaw Bio-Base Version one and exact results when only CASIA V3 Interval Iris is utilized. Additionally, the ResNet50 achieved the greatest accuracy for the Warsaw V2 at 97.26 %. In contrast, using mentioned datasets (Warsaw Plus CASIA), the ResNet50 achieved a 98% of iris test accuracy. The impact of eye diseases on iris segmentation and recognition is being investigated and evaluated. The findings revealed that eye diseases, in some cases, have a considerable impact on iris segmentation, particularly in the case of mixed diseases, pupil abnormalities, eye trauma, blindness, some retinal detachments, and bloody eye concerns. The results also show that several eye problems, such as cataracts, glaucoma, blurry conditions, some lens abnormalities, and some corneal problems, have no effect on iris segmentation when they exist separately. When it comes to iris recognition, eye illness has a smaller impact when it comes to iris segmentation. Some cases of blindness are easily recognized. The ocular scenario in which the iris is covered, or its structure is modified partially or wholly is the most impactful challenge to iris recognition. The results show that some unique circumstances can be easily incorporated into iris recognition systems. According to the results, some eye problems can make it hard for iris recognition to work. This should be checked out and fixed before using biometric systems.

Key Words **:** Eye diseases, image processing, CNN, transfer learning.

Science Code **:** 92418

ÖZET

Yüksek Lisans Tezi

HASTALIKLARIN VARLIĞINDA SEGMENTASYON VE DERİN ÖĞRENME İLE İRIS TANIMA

Abbadullah .H SALEH

Karabük Üniversitesi
Lisansüstü Eğitim Enstitüsü
Bilgisayar Mühendisliği Anabilim Dalı

Tez Danışmanı:
Dr. Öğr. Üyesi Oğuzhan Menemencioğlu
Temmuz 2022, 131 sayfa

Herhangi bir iris tanıma sisteminde iris segmentasyonu ve iris tanıma olmak üzere iki ana adım yer alır. Son yıllarda birçok iris segmentasyonu ve tanıma sistemi tanıtılmıştır. Çok az sayıda araştırma, göz patolojisi vakalarına ve bunların iris segmentasyonu ve tanıma sistemleri üzerindeki etkilerine odaklanmıştır. Mevcut çalışmada, göz hastalığı olan durumlar için, yeni bir derin öğrenme tabanlı iris tanıma sistemi tanıtılmaktadır. İris segmentasyon adımında yeni bir dinamik dairesel Hough dönüşüm algoritması tasarlanmış ve gerçekleştirilmiştir. Tanıma adımında, üç farklı derin öğrenme modelini (GoogleNet, ResNet50 ve ResNet101) uygulamak için transfer öğrenme yaklaşımı, kullanılmaktadır. Üç ayrı veri seti kullanılmıştır. Birincisi çeşitli göz bozuklukları olan 684 kişinin iris görüntüsünü içeren Warsaw Bio-Base V1 veri setidir. İkincisi, daha karmaşık göz vakaları ve daha fazla sayıda fotoğraf içeren 1793 iris taramasına sahip Warsaw Bio-Base V2 veri setidir. Üçüncüsü, 2639 sağlıklı

iris fotoğrafına sahip CASIA V3 Interval Iris veri setidir. Deneyler, farklı eğitim ve değerlendirme senaryoları altında yapılmıştır.

Bu senaryolar sırasında birçok eğitim konusu dikkate alınır: üç derin öğrenme modeli, farklı bölme kriterleri; renkli ve gri tonlamalı iris görüntüleri; bölümlere ayrılmış & orijinal iris görüntüleri ve öğrenimi iki eğitim katmanı olarak aktarılmıştır. MATLAB 2020a, gerekli tüm yazılımları oluşturmak için kullanılmıştır. Bunun yanında Derin öğrenme ve görüntü işleme gibi bazı araçlar kullanılmıştır. Eğitim doğruluğu, geçerlilik doğruluğu, test doğruluğu, hata matrisi, TPR, FNR, PPR, FDR ve eğitim süresi gibi sonuç modellerinin doğruluğunu kontrol etmek için birçok yol kullanılmıştır. İris segmentasyonunun veri doğruluğu oluşturulmuştur ve sonuçlar, Warsaw Bio-Base V1 veri seti için %0,79'luk düşük bir FPR ve %5,49'luk bir FNR'yi göstermektedir. Sonuçlar, GoogleNet'in her durumda düşük hesaplama süresine sahip olduğunu ancak ResNet modellerine kıyasla daha düşük performansa sahip olduğunu göstermektedir. Ancak, iris tanıma doğruluğunun ResNet50 ve ResNet101 tarafından sırasıyla yalnızca Warsaw Bio-Base Sürüm 1 için %98,5 ve %99 olduğu senaryo No. (6)'daki en iyi tanıma doğruluğu ve yalnızca CASIA Interval V3 kullanıldığında kesin sonuçlar elde edilmektedir. Bunlara ek olarak, ResNet50 %97,26 ile Warsaw V2 için en yüksek doğruluğu elde edilmiştir. Buna karşılık, birleştirilmiş veri kümelerini (Warsaw artı CASIA) kullanan ResNet50, %98'lik bir iris tanıma oranı elde etmiştir. Göz hastalıklarının iris segmentasyon ve tanıma üzerindeki etkisi araştırılmış ve değerlendirilmiştir. Bulgular, göz hastalıklarının, bazı durumlarda, özellikle karışık hastalıklar, göz bebeği anormallikleri, göz travması, körlük, bazı retina dekolmanları ve kanlı göz rahatsızlıkları durumunda iris segmentasyonu üzerinde önemli bir etkiye sahip olduğunu ortaya koymaktadır. Sonuçlar ayrıca katarakt, glokom, bulanıklık durumları, bazı lens anormallikleri ve bazı kornea rahatsızlıkları gibi çeşitli göz problemlerinin ayrı ayrı bulunduklarında iris segmentasyonu üzerinde hiçbir etkisi olmadığını göstermektedir. İris tanıma söz konusu olduğunda, göz hastalığının iris segmentasyonuna nazaran etkisi daha az bir orandadır. Bazı körlük vakaları kolayca tanınır. İrisin kaplandığı veya yapısının kısmen veya tamamen değiştirildiği oküler senaryo, iris tanıma için en etkili zorluktur. Sonuçlar, bazı benzersiz koşulların iris tanıma sistemlerine kolayca dahil edilebileceğini göstermektedir. Sonuçlara göre, bazı

göz problemleri iris tanımanın çalışmasını zorlaştırabilir. Biyometrik sistemleri kullanmadan önce bu kontrol edilmeli ve düzeltilmelidir.

Anahtar Kelimeler **:** Göz hastalıkları, görüntü işleme, CNN, transfer öğrenme.
Bilim Kodu **:** 92418

ACKNOWLEDGMENT

I would like to thank Allah, the Most Merciful, for giving me the opportunity to study master's and complete my thesis period. I hope that this thesis will contribute to the service of eye patients and support engaging them in biometric recognition systems. Gratitude should also go to the thesis supervisor, Assist Prof. Doctor Oğuzhan Menemencioğlu since this endeavor would not have been possible without his generous support for the editing help, late-night feedback sessions, and moral support. My sincere thanks to the Karabuk University staff, professors, and doctors who impacted and inspired me. Thanks, should also go to my family, especially my wife and daughter. Their belief in me has kept my spirits and motivation high during this process.

I dedicate my thesis with gratitude to our motherland Iraq and the wonderful Turkey, which welcomed our scientific experiment and assisted in providing every possibility to graduate in this magnificent manner.

CONTENTS

Page

Page

Page

LIST OF FIGURES

Page

Page

LIST OF TABLES

Page

Page

SYMBOLS AND ABBREVITIONS INDEX

ACHTM	:	Adaptive Circular Hough Transform
CHT	:	Circular Hough Transform
CNN	:	Convolutional Neural Network
MBIS	:	Morphological-Based Iris Segmentation
CM	:	Confusion Matrix
DL	:	Deep Learning
TSR	:	True Segmented Result
FSR	:	False Segmented Result
TP	:	True Positives
TN	:	True Negatives
FP	:	False Positives
FN	:	False Negative
TPR	:	True Positive Rate
FNR	:	False Negative Rate
PPR	:	Positive Predictive Rate
FDR	:	False Discovery Rate

PART 1

RESEARCH OVERVIEW

1.1. INTRODUCTION

Nowadays, human recognition is one of the most challenging issues related to computer science applications. Traditional human authentication approaches like passwords and cards can be stolen or corrupted. Attackers can steal passwords and cards in addition to losing or forgetting them. On the other hand, biometrics are more secure techniques for human identification and have many unique features, making them suitable for human recognition [1].

Unfortunately, there are two basic problems with these biometrics. They are changing through time, so people need to update their samples over time. The second problem is that they need special equipment to acquire samples of some biometrics. The good news is that some biometrics (like the face) are non-intrusive, but it still includes potential problems like changing over time and providing inevitable error rates. Human-face has many distinctive features, including the face parts locations, the distance between face parts, face contour, etc. Besides that, the projection of 3D face images into 2D images creates new problems such as illumination and pose variations, occlusion, scaling, rotation, etc. [2,3]. Other biometrics like iris, for example, have distinctive features called iris patterns, and they are more accurate and have fewer variations problems. Some biometrics change over time (like the face), while others do not (like iris, ear, and fingerprint). While fingerprint, palm print, and face are exposed to changes due to accidents (burns, wounds, etc.) [4], others like iris, ear, and footprint are affected less. However, identical twins' problem is also considered a critical issue in human recognition systems; fortunately, some biometrics like iris and DNA do not suffer from this problem.

The only problem with iris is that it requires special tools for acquiring images. Iris recognition has been denoted as accurate, reliable, and highly confident biometrics, especially when dealing with large datasets. Iris is a unique high rich-data biometric containing distinctive features. Besides that, the iris has an almost fixed shape over time and is robust against all image variations [5].

Although iris is one of the most accurate biometrics [6], it is affected by diseases that impact the ability of the recognition systems. [7].

1.2. AIMS

This research aims to:

1- Develop a new iris recognition system in the presence of eye diseases.
2- Enhance iris segmentation by using a new approach extracting only iris patterns and removing noise (eyelash and eyelid).
3- Improve the performance of iris recognition in the presence of disease by using deep learning networks.

1.3. IMPORTANCE AND CONTRIBUTION

People with eye diseases are usually excluded from iris recognition systems; this will be solved by:

1- Using the second iris in case of one-eye disease
2- Extracting the best iris patterns
3- Reduce the noisy non-iris regions in the final segmented iris
4- Using deep learning networks that enhance the iris recognition process.

Identify the effect of each disease on iris recognition so that we can know the individuals with eye diseases who are capable of participating in iris recognition systems. The research will also compare the same models in the case of eye diseases and healthy individuals

1.4. PROBLEM STATMENT

The iris recognition in case of disease is a critical and essential part of iris recognition systems.

Iris image variations such as illumination variations, left-right iris, occlusion by eyelashes and eyelids, and pose variations affect the performance of iris recognition systems. So, we need to treat them in order to get high performance.

1.5. HYPOTHESES

The current research introduces the recognition system with the following hypotheses:

1- The suggested iris pattern-based segmentation method will enhance the accuracy.
2- Deep learning neural networks are the best choice for iris recognition in the case of iris diseases.
3- The performance of the iris recognition system is affected differentially in terms of different eye diseases.
4- Using a preprocessing illumination compensation step will enhance the performance of the segmentation stage.

1.6. BLOCK DIAGRAM

Figure (1.1) illustrates the general stages of the system. Two main stages are involved in the proposed iris recognition system: Training and test. In the training stage, three steps are applied: the preprocessing of iris dataset images (enhancement, illumination correction, some morphological operations, etc.), the iris segmentation, and the recognition (training) based on deep neural networks. The same steps of the test stage will be applied, but the difference is that, in the recognition step, we will apply the test operations in which the trained model will be examined using test samples, and the evaluation metrics will be computed to evaluate the proposed iris recognition models.

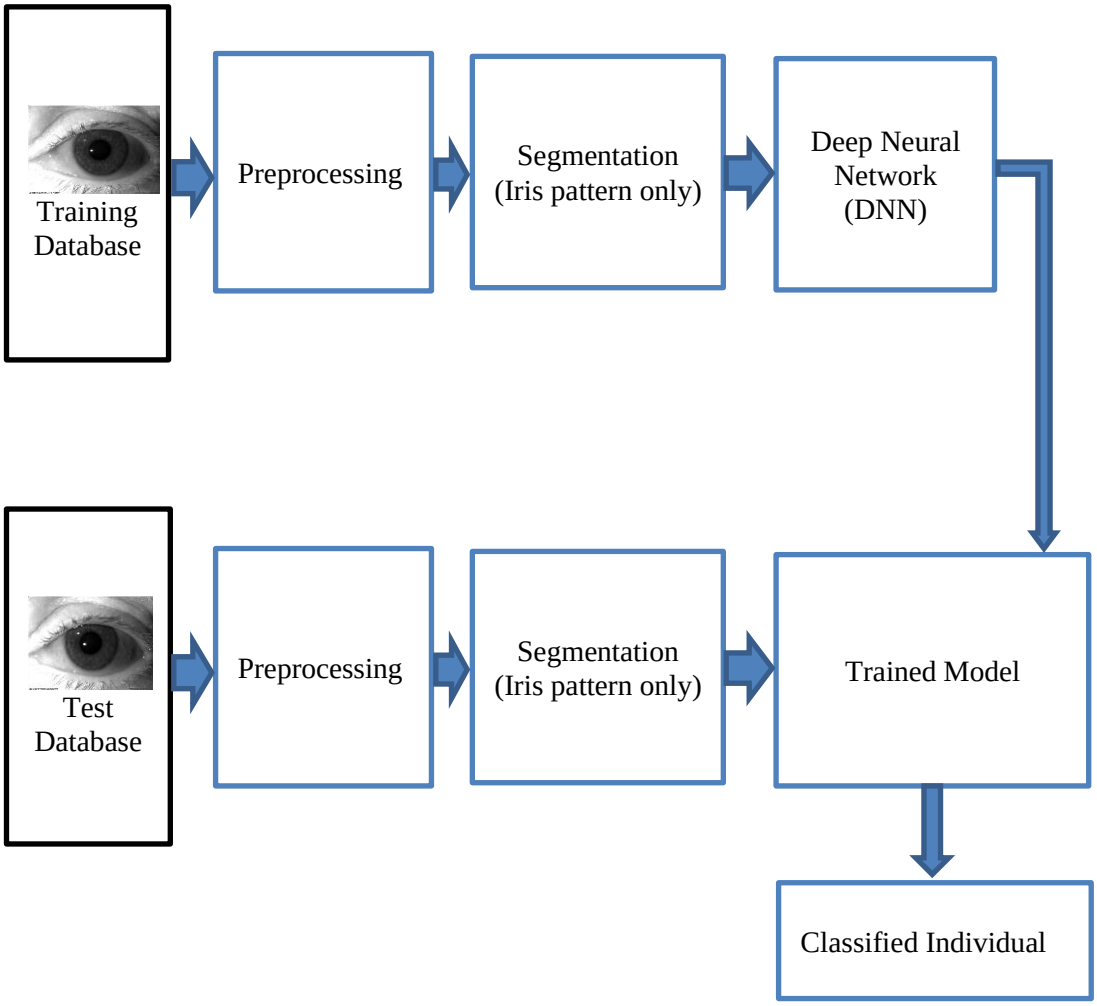

Figure 1.1. Block diagram of the proposed iris recognition system.

The rest of the thesis will be organized as follows: in chapter 2, the related work and previous research will be discussed. Chapter 3 includes the proposed methodologies and the used materials. Results will be included in chapter 4, while chapter 5 will contain the discussion and conclusion.

PART 2
BACKGROUND

2.1. INTRODUCTION

Iris recognition is a sub-field of human biometrics that has been frequently used in human recognition activities. The iris patterns differ even for identical twins, and their unique features allow scientists to develop very accurate and robust iris recognition systems [8].

Eye conditions such as diseases, occlusion, camera-related, image degradation, and many other factors significantly affect iris segmentation and recognition [9–11]. Some studies mentioned that the effect of these factors differed between the iris segmentation and recognition [9]. However, eye diseases are the most challenging conditions in which the eye structure and iris may affect at different levels [11,12].

Many pieces of research have been introduced in the field of iris recognition. All these researches were based on either one dataset or multiple datasets [13]. Some of these datasets contained normal conditions [14], while others dealt with eye diseases [11,12]. However, these datasets differ in many aspects like source camera type, spectrum type, image dimensions, image formats, challenges (disease, occlusion, illumination variation, pose variations, etc.), number of images, and number of individuals [13].

2.2. IRIS SEGMENTATION

Many studies have been introduced in iris segmentation, and many approaches have been designed and evaluated. The attention to iris segmentation studies has increased significantly over the last ten years [15].

Mayya and Saii [6] proposed an iris segmentation method using pupil and iris localization, and then they normalized the iris into polar coordinates. They applied experiments on the CASIA iris dataset, including 250 individuals getting 98% accuracy. However, their approach included some false positives. Kaur et al. [16] used the Hough transform and normalization on four public datasets: CASIA-IrisV4-Interval, IITD.v1, UBIRIS.v2 and UPOL. The main problem of this previous approach is that the segmented iris circle contains noisy parts (eyelids) in most cases.

Zernike moments and Gabor filter, along with the iris pattern methods, were proposed by Naji et al. [17]. They extracted the iris regions with the slightest noise (eyelash and eyelid) based on segmenting the iris region into eight sub-regions and studying the statistical information within each region. They removed all high noise sub-regions and merged the resulting iris sub-regions into a unified 120*120 matrix. They applied their experiments on two datasets CASIA v1 and their own collected dataset, but the problem is that their method removes parts of the iris in all cases.

In another recent research, Li et al. [18] proposed a new method of iris segmentation using K-means to retrieve the outer border of the iris and Residual U-Net for semantic segmentation. They applied their results to the CASIA-Iris-Thousand dataset. Experiments were applied on the CASIA thousand dataset and got intersection over union (IoU) of 98.9% and 97.7% of iris outer and inner boundary detection. The main problem of this approach is the computational time.

Recently, Trokielewicz et al. [19] used 76 cases of Warsaw-Bio-Base-Disease for iris segmentation and the deep CNN classifier to segment iris. They obtained 3.11% as an Equal Error Rate EER for their selected dataset. CNN is a powerful technique to segment eye images; however, it takes more computational time than traditional methods. For Cataract sugary, Sokolova et al. [20] proposed a new method for the automatic segmentation of iris to help the physician detect pupil and iris ROIs. They used 82 annotated iris images with cataract disease and applied many machine learning algorithms. The masked R-CNN algorithm was applied for the segmentation part. The experiments were done using the Intersection over Union (IoU) and mean average precision (mAP), and they proved that the segmentation result of the deep networks

with the entirely trained layers was better than the head-only trained ones. The results also indicated that the bounding boxes derived from the predicted segmentation method were better than the masked R-CNN ones.

Agha and Jan [21] designed a low computational iris localization system. First, they used the order statistic filtering to eliminate the lightning reflection; then, the edge detection based on the coarse-to-fine method was applied to detect eye edges. The edges that correspond with the lowest gray level in a circular neighborhood were chosen as the pupil regions. After that, the iris region around the pupil is detected using a canny edge detector. The experiments were applied on many datasets and got 99.7%, 98.35%, 99.3%, 99.13%, 97.56%, 98.89%, 98% and 98.56% as segmentation accuracy of CASIA V1.0, CASIA-IrisV3-Lamp, CASIA-IrisV3-Interval, MMU V1.0, MMU 2.0, UBIRIS V1.0, IITD V1.0, CASIA-IrisV3-Twins datasets respectively. As in many other studies, the main problem of their method was that they obtained the iris as a specific circle, including some other false positive regions outside the iris, especially when the image included some occlusion. Using the search harmony algorithm, Malinowski and Saeed [22] presented a size-independent iris recognition method. The pupil was detected using the Blob detection algorithm. The edge approximation based on Harmony search is used to detect eyelid boundaries even in noise and degradation. The eyelashes and shadows were removed by the variation and average methodology. The experiments were applied to the UBIRIS.V1, MMU.V1, and MILES databases. They obtained 98.14%, 90%, and 99.8% as segmentation accuracy of UBIRIS. V1, MMU.V1, and MILES, respectively. In 2022, Nachar and Inaty [23] used a fuzzy-based model for iris segmentation. A new method called "edge contour EC" was used to segment the iris by defining the edge features of the crypts, stripes, and spots. Experimental tests showed that the iris localization accuracy was 99.85% on a subset of CASIA, IITD Delhi, UBIRIS v2, and MICHE datasets.

In this research, we introduce a novel iris segmentation method in which a specific type of people who have eye disease is targeted to study the effect of disease on the iris segmentation system, so we will extract the iris patterns only without noisy parts like eyelids as possible without removing any part of iris patterns. Table (2.1) includes a detailed comparison of some previous iris segmentation studies.

Table 2.1. Comparison of the previous iris segmentation-related work.

Nu.	Study	Methods	Dataset/ Data size	Dataset Challenge	Performance/ Remarks
1	Daugman 1993 [24]	Integro-differential operator (IDO)	Special Dataset/ (No size definition)	No challenge mentioned	ACC=98%
2	Wildes et al. 1994 [25]	Hough Transform (HT) and Edge Detection	Special Dataset/ (No size definition)	No challenge mentioned	ACC=99.5%
3	Ma et al. 2002 [26]	Pupil localization using coarse localization, Edge detection, HT	CASIA V1/ 2096 images	No challenge mentioned	Not mentioned
4	Koh et al. [27]	Active countering, Hough transform	CASIA V3/ 100 images	Nonlinear deformations , eyelash occlusion	ACC=99%, with false positives
5	Mayya and Saii 2016 [6]	Pupil localization with Daugman's method	CASIA V1/ 250 individuals	Occlusion/Illumination and pose variation	98% with false positives
6	Kaur et al. 2018 [16]	Pupil and iris localization using HT	CASIA-IrisV4-Interval, IITD.v1, UBIRIS.v2 and UPOL/ Data size: 1500 images of 50 individuals	Occlusion/ reflections/ distantly acquired under less constrained environments	High true positive rate but high false positives rate
7	Naji et al. 2020 [17]	Iris pattern detection using division method	CASIA V4	Occlusion by eyelid and eyelashes	Bad segmentation (too many false positives and false negatives)
8	Trokielewicz et al., 2020 [19]	CNN	Warsaw-Bio-Base-V1-Disease/ 76 individuals	Eye diseases	EER=3.11 with normalization, 2.55% without normalization, With computational time. Many individuals were excluded from the original dataset.
9	Sokolova et al. 2020 [20]	predicted segmentation, Masked R-CNN	82 annotated iris image of cataract surgery	Cataract disease	Small data size

Nu.	Study	Methods	Dataset/ Data size	Dataset Challenge	Performance/ Remarks
10	Agha and Jan 2020 [21]	Coarse-to-fine method, Canny edge detector,	CASIA V1.0, CASIA-IrisV3-Lamp, CASIA-IrisV3-Interval, MMU V1.0, MMU 2.0, UBIRIS V1.0, IITD V1.0, CASIA-IrisV3-Twins	Reflections, Eyeglasses, Occlusion, Eyelashes	ACC: CASIA V1=99.7% CASIA IrisV3-Lamp =98.35% CASIA-IrisV3-Interval =99.3% MMU V1.0=99.13% MMU 2.0=97.56% UBIRIS V1=98.89% IITD V1=98% CASIA-IrisV3-Twins =98.56% Results include False positives.
11	Li et al. 2021 [18]	K-means, Semantic segmentation by U-Net	CASIA-Iris-Thousand	Sunglasses existence	IoU= 98.9% and 97.7% of outer and inner boundary detection with computational time
12	Francese et al. 2021 [28]	The Daug-man and Canny edge detection algorithms	238 images	Coloboma eye condition	15.79% and 47.37% of eye images containing Coloboma were correctly segmented
13	Hu et al. 2021 [29]	Masek, RTV-L, OSIRIS, IrisSeg, DeepLab and U-Net	CASIA-Iris-Degradation Version 1.0/ 15 individuals with 3577 iris images	different illumination, off-angle large scale, occlusion, glass existence, Nonideal states	ACC (U-Net)= 95.17%
14	Malinowski and Saeed 2022 [22]	Blob detection, Harmony search	UBIRIS. V1, MMU.v1 and MILES	Occlusion, Eyelashes	ACC UBIRIS V1: 98.14%,MMU V1: 90%, MILES: 9.8%
15	Nachar and Inaty 2022 [23]	Fuzzy-based model, edge contour (EC)	A subset of CASIA, IITD Delhi, UBIRIS v2,and MICHE datasets	Reflections, off-focus, blurring, gaze deviation, occlusion	ACC=99.85%

2.3. IRIS RECOGNITION

In the research of Roizenblatt et al.[30], an iris recognition methodology is applied after cataract surgery. The research used 55 eye images obtained from 55 individuals. The Hamming distance is used for the matching part. The results indicated that there were 6 cases in which the recognition failed. Pierscionek et al. [31] introduced an iris recognition system based on their own collected dataset. Their iris dataset directly acquired the iris region (not the eye) so that there was no segmentation step since the iris ROI was already acquired. The dataset was collected from only 27 healthy individuals. Furthermore, the pupil's center is located manually to normalize the iris. The study discussed only the iris localization problem without any evaluation metrics. Aslam et al. [32] applied the iris recognition process in the case of ocular diseases. They studied the effect of eye pathology on the iris recognition process. The study included 54 individuals with anterior segment disease. The researchers followed the methodology of comparing the iris templates before and after the treatment of eye disease using the Hamming distance approach. The results proved that the performance of iris identification is affected by some eye diseases (corneal edema, iridotomies, and conjunctivitis) significantly.

Minaee and Abdolrashidi [33] introduced an iris recognition deep learning system based on ResNet50. They used the IIT Delhi iris database containing 2240 eyes of 224 individuals and got an accuracy of 95.5%. Trokielewicz et al.[10] were the pioneer of iris recognition in the case of eye diseases. They studied the effect of Cataract eye disease on the performance of iris recognition systems. They collected a dataset of 1288 eye images of 37 individuals from the Medical University of Warsaw. Three different built-in iris recognition systems were used in that study, like VeriEye, MIRLIN, and BiomIrisSDK. The experiments showed some worse results of the unhealthy samples. The false non-match rate also increased significantly.

In 2015, they continued their work and used three built-in software (MIRLIN, VeriEye, and OSIRIS) for iris recognition[11]. They used a subset of the Warsaw Bio-Base V1 dataset, including 1353 images of 219 individuals. The subset was partitioned into four parts (Healthy, Clear, Geometry, Tissue, and Obstructions), and then the

Failure to Enroll Rate (FTR) was computed. The worst results were 18.36% and 5.13% for the Obstructions and Geometry, respectively. Hsiao et al. [34] used the U-net model for the semantic segmentation of iris ROI. The cropped iris was enhanced using histogram equalization and Gabor filter. An EfficientNet model was applied on the enhanced-cropped irises of the CASIA v1 dataset, and the obtained accuracy was 98%.

Omran and AlShemmary [35] proposed an iris recognition system based on three stages. They first determined the iris and pupil ROIs, and then the iris ROI was transformed from the Cartesian coordinates to the polar ones (the normalization step). The basic architecture of the classifier was the convolutional neural network and softmax function. The experiments were applied on the IITD V1 iris database and obtained identification rates of 97.32% and 96.43% in the case of original and normalized images, respectively.

Karn et al. [36] used the Total Relative Variation (RTV) method for the iris segmentation step. In comparison, they applied the probabilistic collaborative approach for the recognition part. They also normalized the iris images using an iris localization approach. The experiments were applied on CASIA-IrisV4-Lamp and IIT Delhi.V1 databases (7800 images of 390 individuals were chosen as a subset). The proposed methodology got a 99.96% test accuracy with 0.04% FPR on the CASIA subset, while the IIT Delhi V1 dataset resulted in a 99.99% test accuracy and 0.01% FPR. Multi-objective feature extraction and deep learning CNN networks were merged in a study by Babu and Khayum [37]. Their study consisted of many steps, including preprocessing, segmentation, optimal ORB feature selection, and optimal recognition. Filtering and enhancement operations were applied in the first step, while for iris segmentation, they used the circular Hough transform to localize iris regions. The optimized CNN deep network was used in the last stage for the recognition aim. The experiments were applied on the IIT Delhi (IITD) and MMU iris datasets. They obtained 99.5%, 0.002%, and 0.907% accuracy, FPR, and FNR, respectively. The main problem of their approach was in the segmentation part, where the false positives parts of non-iris accepted regions were high. In 2017, Trokielewicz et al. [38] proposed a new iris recognition system in case of ocular pathologies. They used a collected dataset of 2996 eye images collected from 230 individuals. The study included more

than 20 eye diseases and their effect on the performance of iris recognition. They used built-in software (MIRLIN, VeriEye, OSIRIS, and IriCore) and included four principles. The first principle was the effect of eye conditions on the enrollment process. The second was the effect of eye conditions in which there were no non-visible changes in the eye structure on increasing the dissimilarities between eye samples of the same individuals. The third was the effect of eye diseases that changed eye geometry on the similarity of the same-eye samples. The final principle dealt with segmentation errors. The experiments were applied on 1353 images of 219 individuals, and they concluded that the FTE error rates were higher in the case of geometrical eye conditions. The automatic iris segmentation process was the most effective cause of iris recognition errors. Obstructions-related eye diseases were the main eye conditions that affected the entire iris recognition built-in systems.

In 2021, Francese et al. [28] studied the effect of Coloboma eye condition on the performance of iris recognition and, specifically, the iris segmentation and localization process. The results showed that only 15.79% and 47.37% of eye images containing Coloboma conditions were correctly segmented. They evaluate the effect of this condition on Daugman's algorithm and canny edge detector. For recognition, the ResNet model achieved a 99.79% accuracy on a dataset consisting of only 238 eyes. Their dataset size was too small and needed to enlarge.

Combining the NASNet deep learning network and the morphological image feature extraction algorithms, Soni et al. [39] designed an iris recognition system using Circular Hough Transform (CHT). They used the CASIA interval dataset containing 1344 iris images. They concluded that the model validation accuracy was 100%, with 0.0262 as a loss. They used no test dataset, and the entire dataset size was small. Borkar and Salankar [40] discussed the different approaches used in iris recognition systems. They used their iris images collected from a specific camera without defining the dataset's size or format. They first applied the iris segmentation process then the matching was done using the Hamming distance. Their experiments had no specific evaluations or metrics.

Sujana and Reddy [41] proposed an iris identification system based on CNN deep networks. They applied iris segmentation using the Hough transform and Canny edge detector. The experiments were applied on 108 individuals of the CASIA v1 and IITD datasets achieving 95.4% and 98% accuracy.

Recently in 2022, Jia et al. [42] proposed a deep-based system of iris recognition based on the ConvNet deep neural network. They used the multi-level interaction method to correlate the iris features of many convolutional layers. The essential enhancement of their methodology was the masking approach that excluded the noise and improved performance. Their experiments were applied on ND-IRIS 0405, CASIA-IrisV4-Thousand, and CASIA IrisV4-Lamp datasets. They collected 9,578, 1092, and 5321 iris images for training, validation, and testing. The proposed methodologies achieved FARs of 5.49% on ND-IRIS-0405, 10.41% on CASIA-IrisV4-Thousand, and 5.8% on CASIA-IrisV4-Lamp.

Hu et al. [29] created a new dataset called CASIA-Iris-Degradation Version 1.0 (DV1), consisting of iris images taken of 15 individuals under a less cooperative acquisition system. The dataset included different degradation levels like different illumination, off-angle large scale, occlusion, some glass existence cases, and non-ideal states. The final dataset size was 3577 iris images. The researchers applied the experiments in two steps; segmentation and recognition; meanwhile, they used well-known open-source methods in both stages. Masek, RTV-L, OSIRIS, IrisSeg, DeepLab, and U-Net used segmentation systems. They used iris recognition systems were Masek, OM, UniNet, MaxoutCNN, AFINet, and DGR. U-Net segmentation approach was the best one with a precision of 95.17%, while UniNet was the best recognition system with an EER of 13.13%. The fastest segmentation algorithm was U-Net (12.37 frame per second (fps) as average time), while the MaxoutCNN was the fastest recognition system with 312.01 fps. The study concluded that all those open-source systems were not robust against all conditions in the created dataset.

Iris recognition using transfer learning of VGG and MobileNet V2 networks and the non-linear scaling methods was introduced in a Ph.D. study [43]. The experiments were applied on a subset of IIT Delhi and MMU.2 datasets (1957 images of 195

individuals). The results indicated an enhancement in CNN performance after using the non-linear scaling. For the MMU2 dataset, the acquired accuracies of the MobileNet V2 network were 86% and 90% for validation and test sets without any non-linear scaling, but by using the non-linear scaling, the accuracies became 86% and 84%, respectively. However, for the IIT Delhi dataset, non-scaling increased the validation accuracy from 82.79% to 84.774%. The same result was obtained for the test set, where the accuracy was enhanced by 1.8%. On the other hand, and for the VGG network, the results indicated enhancement in performance after using the non-linear scaling with factor γ = 0.8, but the results went worse when using γ = 1.2. Although the study listed too many results in the case of using non-linear scaling, the experiments still have no proof of the importance of using non-linear scaling since it was terrible in some test scenarios.

Table 2.2. Comparison of the previous iris recognition-related work.

Nu.	Study	Methods	Dataset/ Data size	Dataset Challenge	Performance/ Remarks
1	Roizenblatt et al. 2004 [30]	Hamming distance	55 eye images	Cataract surgery	There were 6 cases in which the recognition failed
2	Pierscionek et al. 2008 [31]	No segmentation, iris localization	Their own dataset/ 27 healthy individuals	No challenge	Not mentioned
3	Aslam et al. 2009 [32]	Hamming distance	54 individuals	Ocular diseases (anterior segment disease)	The performance of iris identification is affected by ocular diseases
4	Trokielewicz et al. 2014 [10]	VeriEye, MIRLIN, and BiomIrisSDK	1288 eye images of 37 individuals of Warsaw University	Eye diseases	Worse results of the unhealthy samples
5	Trokielewicz et al. 2015 [11]	VeriEye, MIRLIN, and Biom-IrisSDK	Warsaw Bio-Base V2/ 1353 images of 219 individuals	Healthy, Clear, Geometry, Tissue and Obstructions eye conditions	FTR (Obstructions of MIRLIN) =18.36% FTR (Obstructions of OSIRIS) =8.21% FTR (Geometry of VeriEye) =5.13%. The poor performance reasons due to the segmentation errors.

Nu.	Study	Methods	Dataset/ Data size	Dataset Challenge	Performance/ Remarks
6	Trokielewicz et al. 2017 [38]	MIRLIN, VeriEye, OSIRIS and IriCore	1353 images of 219 individuals and excluded 11 distinct irises.	20 eye diseases	Obstructions-related eye diseases were the main eye conditions that affected the entire iris recognition. The segmentation errors cause a performance drop.
7	Wang and Kumar 2019 [44]	CNN with residual network learning	ICE2006 (35 eyes), CASIA V4 distance (142 individuals, WVU Non-ideal	Off-angles, with blur, sensor noise, and the occlusions	ICE2006: 97.1% CASIA: 87.5% WVU: 96.1%
8	Minaee and Abdolrashidi 2019 [33]	ResNet50	IIT Delhi/ 2240 eyes of 224	No challenge mentioned	ACC=95.5%
9	Chen et al. 2020 [45]	CNN with T -Center loss and SoftMax	ND-IRIS-0405, CASIA-Thousand, and IITD	Reflection Eyeglasses	TPR (ND-IRIS-0405) =97.87% TPR (CASIA-Thousand) =92.54% TPR (IITD) =97.43% High complexity
10	Omran and AlShemmary 2020 [35]	Pupil localization, Iris normal-ization, CNN	IITD V1	No challenge mentioned	ACC (Original Images) = 97.32% ACC (Normalized Images) = 96.43%
11	Karn et al. 2020 [36]	Relative Total Variation (RTV)	CASIA-IrisV4-Lamp and IIT Delhi.V1/ 7800 images of 390 individuals	Reflections, blur, Occlusion	ACC (CASIA)=99.96% FPR (CASIA)=0.04% ACC (IIT)=99.99% FPR (IIT)=0.01%
12	Hsiao et al. 2021 [34]	U-net for segmentatio, EfficientNet for recognition	CASIA v1	No challenge mentioned	ACC=98%
13	Francese et al. 2021 [28]	ResNet	238 images	Coloboma eye condition	ACC=99.79%

Nu.	Study	Methods	Dataset/ Data size	Dataset Challenge	Performance/ Remarks
14	Soni et al. 2021 [39]	NASNet, Circular Hough Transform (CHT), and morphological features	CASIA interval/ CASIA interval	Not mentioned	ACC=100%, Loss=0.062. Small data size, no test set
15	Borkar and Salankar 2021 [40]	Hamming distance	Their own dataset	Not mentioned	No specific evaluations or metrics
16	Hu et al. 2021 [29]	Masek, OM, UniNet, MaxoutCN, AFINet, and DGR	CASIA-Iris-Degradation Version 1.0/ 15 individuals	Different illumination, off-angle, occlusion, glass existence, Nonideal states	FPS(MaxoutCNN) =312.01. EER (UniNet)= 13.13 All used recognition systems were not robust against all conditions.
17	Babu and Khayum 2022 [37]	HT for segmentation, CNN for recognition	IIT Delhi (IITD) and MMU	No challenge mentioned	ACC= 99.5% FPR= 0.02% FNR = 0.907% Too false positives in segmentation step.
18	Jia et al. 2022 [42]	ConvNet with a masking approach	ND-IRIS 0405, CASIA-IrisV4-Thousand, and CASIA IrisV4-Lamp/ 9,578, 1092, and 5321 iris images for training, validation, and test	Noise	FAR (CASIA Thousand) =10.41%. FAR (CASIA Lamp) =5.8%. FAR (ND-IRIS-0405) =5.49%.
19	Shah (Ph.D. study) 2022 [43]	Non-linear scaling, VGG and MobileNet V2	A subset of IIT Delhi and MMU.2 datasets/ 1957 images of 195 individuals	No Challenge mentioned	MMU2: Without Non-linear scaling: Val-ACC=86%, Test-ACC=90%. With Non-linear scaling: Val-ACC=86%, Test-ACC=84%. IIT: Without Non-linear scaling: 82.79%. With Non-linear scaling: 84.774%.

Nu.	Study	Methods	Dataset/ Data size	Dataset Challenge	Performance/ Remarks
20	Parzianello and Czajka 2022 [46]	CNN-based segmentation Siamese network-based feature extraction	NDPSID/ 1171 images	Textured contact lenses	EER=10.6%

2.4. RELATED STUDIES CONCLUSION

Some previous studies used too small datasets, while others used datasets with no challenge. Some studies considered challenges like variations, occlusion, reflection, noise, etc. Too few studies dealt with eye diseases (Some of them focused on a specific disease, while others dealt with too small data size). Some of them studied the effect of eye diseases on iris segmentation only, while others used well-known built-in systems to study the effect of such diseases. The current study is the first one that deals with all image variations (occlusion, illumination, pose, noise, reflection) and 20 different eye diseases datasets.

PART 3

MATERIALS AND METHODS

3.1. MATERIALS

3.1.1. Datasets

Three different datasets are proposed in this research. The first two datasets contain several eye diseases, while the third one has no explicit diseases. Warsaw Bio-Base V1 dataset consists of 684 iris images of 53 individuals with different eye diseases for both left and right images [12,66]. On the other hand, the Warsaw Bio-Base V2 dataset includes 1793 iris images corresponding to 115 individuals with different eye diseases (some of them exist in V1, and there are other new diseases) [11,12,67]. Some iris images of Warsaw Bio-Base V1 and V2 are taken through two or three sessions. Each picture in both datasets has a resolution of (640 x 480) pixels which is stored in BMP format. CASIA Interval V3 is the third used iris dataset, including 2639 iris images of 249 individuals in the JPG format along with a (320 x 280) pixel resolution with normal eye conditions; the dataset is built with Cross-session iris images (two sessions for most individuals) [14].

3.1.2. Software

This research employs the following software:

1- Matlab 2020a includes the Deep learning toolbox and image processing toolbox. On a PC with a 64-bit operating system, an x64 processor, 16.0 GB of RAM:(15.8 GB useable), and an Intel (R) Core (TM) i7-10750H CPU @ RAM 2.60 GHZ 2.59 GHz. NVIDIA Ge-Force GTX 1660 Ti with 6 GB memory.

2- Pre-trained deep learning open source packages like; GoogleNet, ResNet50, and ResNet101.

3.2. THE PROPOSED METHODS

This section will introduce an in-depth explanation and description of the methods that have been proposed and utilized. First, we will describe our suggested segmentation methods; then, the proposed recognition models will be presented.

3.2.1. Iris Segmentation Methods

In the segmentation stage, two different developed methods are suggested. The first one is the Morphological-Based Iris Segmentation (MBIS) method, while the second is the Adaptive Circular Hough Transform Segmentation method (ACHTM).

For both methods, an illumination correction preprocessing step is performed in order to get iris images in the best form for segmentation. Figure (3.1) shows steps of the suggested illumination correction algorithm.

The proposed illumination correction approach infers the illumination variation function of the iris images, then applies the opposite function to them, resulting in an illumination-corrected version of all dataset images.

For each original iris image, the illumination variation adds darkness to columns from the right border to the final column (for left eyes). The opposite illumination correction function is constructed by adding incremental values (starts from 1 until the right border of the eye is reached) as shown in equation (3.1).

$$Correctimg = Originalimg + Correction\_Function$$

$$\text{Correction\_Function}(:,i)=\begin{Bmatrix} 0 \text{ if } 0<i<col-1, \\ L \text{ otherwise where } L=1,2,3,\ldots \end{Bmatrix} \quad (3.1)$$

To detect the right iris border of each image, a pupil localization process is done by threshold using a low threshold. Then, the opening, clear border, and region filling steps are needed to obtain the pupil region. After that, the iris right's border is inferred by using the radius of the pupil.

On the other hand, for right eye images, the image is first flipped left-right, and then the previous illumination process is applied. Where $Correct\ img$ is the illumination-corrected iris image $Orgial\ img$, is the original iris image, $Correction\_Function$ is the illumination correction function, i denotes the image column number, col is the column number of the right border of the iris, L is the incremental gray value. Figure 3.1 shows an example of the illumination correction on an iris image.

Figure 3.1. Illumination correction steps on a sample of the iris dataset.

3.2.1.1. Iris Segmentation MBIS Method

Some previous iris segmentation methods use predefined masks and a normalization stage which includes many false positives. While others extract only specific parts of the iris, including iris patterns, which suffer from high false negatives. In the suggested MBIS method, we propose using a morphology-based methodology supported by the illumination correction method to define only the iris region and exclude all other non-iris regions (eyelash and eyelid). In this way, we minimize the false positives and

negatives as much as possible. Figure (3.2) illustrates the detailed steps of the proposed MBIS segmentation method. The original eye image is corrected using the illumination correction method in the first step. Then, a close morphological operation is applied using a 50-radius disk structural element. This step fuses the gray levels inside the image consisting of unified illumination regions (mask image). The mask image is subtracted from the corrected image, and then a threshold operation is applied on the subtraction result. Holes-filling operation is then applied to remove the small undesired pixels getting the final iris image. Using these morphological operations, removes the eyelashes and eyelids as much as possible. The final mask is applied on the original image to get the final iris ROI.

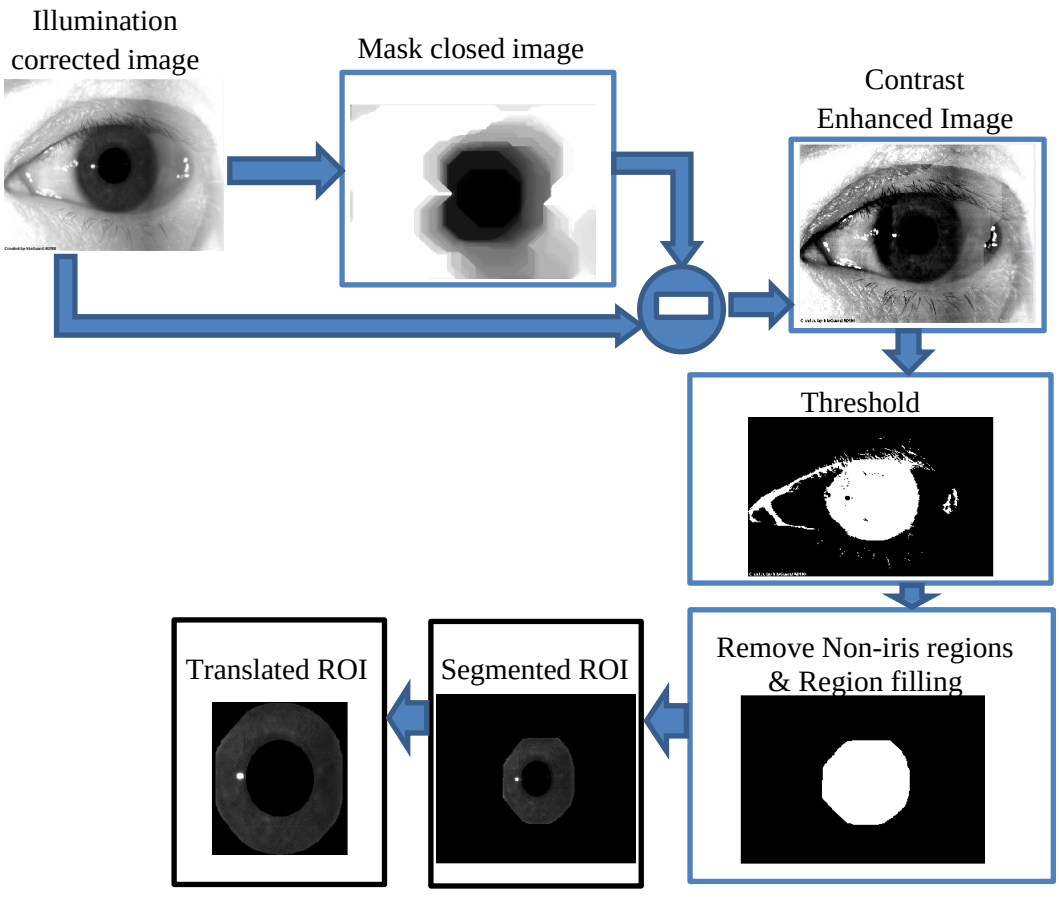

Figure 3.2. MBIS steps.

The final segmented iris image is then translated to get only the iris region and minimize the background area.

3.2.1.2. Iris Segmentation ACHTM Method

The mask subtraction and threshold steps for ACHTM proposed method are the same as the previous MBIS method. After applying the subtraction and threshold steps, the morphological operation (opening) is applied to remove outliers (undesired pixels). After that, the Circular Hough Transform (CHT) is applied to get the potential circular regions (expected iris region) of the threshold image. The detected circle represents the iris region from which the center and radius of the iris region are calculated. This segmented circle is also used to extract the corresponding iris region of the eye image.

There are many previous Hough-based iris segmentation methods [47,48]. Still, the problem with those studies was that they used a specific range for the Hough circle radius. This fixed radius affects the performance of the Hough algorithm, making it detects circles in a specific range (bad in practice, especially in case of different poses and unspecific image acquiring environment). In contrast, in our suggested segmentation method, the Hough Circle Radius Range (HCRR) is computed as the pupil's major axis length (MApup) multiplied by two and displaced by ± MApup/4 pixels.

This method will enhance the Hough transform performance and produce the right iris circles, as equation (3.2) illustrates.

$$\mathrm{HCRR} = 2 * \mathrm{MApup} \pm \mathrm{MApup}/4 \tag{3.2}$$

In some cases, the result iris may contain undesired parts of eyelids. Since eyelids have more brightness than the iris area, the study proposes to remove the high gray-level pixels of the resulting image to eliminate those outliers. This step is done by computing the mean value μ of gray levels inside the iris ROI and thresholding the iris image using μ. Some morphological operations (region filling) are needed to fill gaps to the mask image then the mask image is applied on the original image to get the final iris ROI, as shown in figure 3.3.

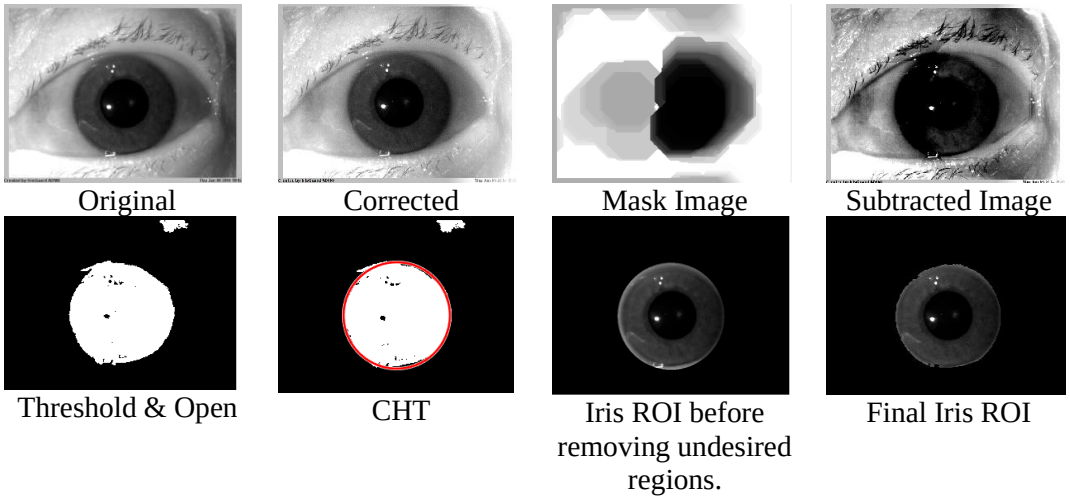

Figure 3.3. Steps of the ACHTM method.

3.2.2. Iris Recognition Methodologies

There are many iris recognition methods introduced in the previous studies. In the current study, three DL models are suggested. GoogleNet, ResNet50, and ResNet101 are the proposed models by which we will apply the iris recognition part based on a very well-known methodology called transfer learning.

3.2.2.1. Transfer Learning

Transfer learning is a powerful solution for transferring knowledge within machine learning methodologies. Transfer learning itself is a machine learning approach that solves the problem of transferring knowledge from a source domain to the target domain. For example, learning the piano for someone who has already learned the violin is easier than for another who has not practiced any instrument before [49].

Transfer learning aims to reduce the number of labeled samples required to learn the target model in the target domain [49,50].

In some cases, transfer learning fails to transfer knowledge due to the low similarity between the source and the target domain (for example, learning how to ride a bicycle does not help in learning how to play a musical instrument); thus, current research also introduces the two layers of transfer learning, where the first layer represent the model which pre-trained on the related samples on the different dataset, for example, CASIA V3 Interval Iris (healthy samples of the iris) then transfer learning to the domine on the second target dataset, for instance, Warsaw Bio-Base (diseased Irises).

According to our knowledge, it is the first work focused on Iris diseased datasets based on two layers approach, as shown in figure 3.4.

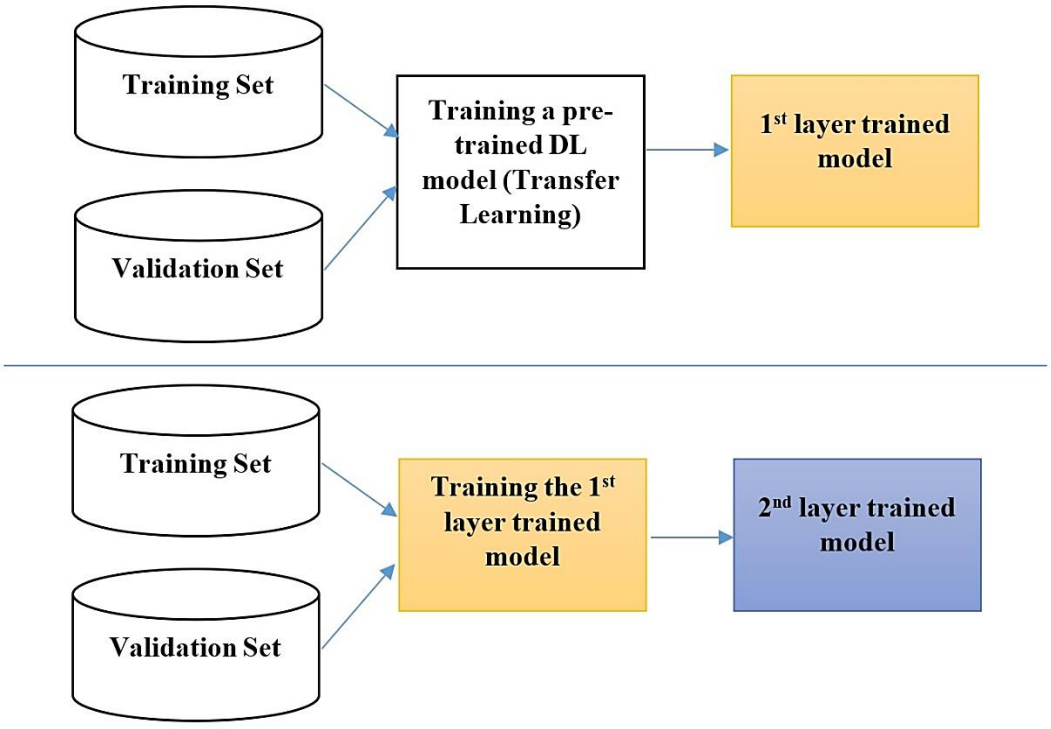

Figure 3.4. Two Layers Transfer Learning Diagram

From another point of view, the similarity between the source and target domain is not always valuable for transfer learning since they can be misleading (transfer learning of different languages) [49].

Transfer learning has been used widely in recognition applications. Urdu character recognition using CNN based on transfer learning of GoogleNet [51], feature transfer learning of face recognition [52,53], and iris recognition based on Alex pre-trained model [54].

If the tasks of the source and target domain are similar, then it is called the transductive transfer learning [53]. On the other hand, if the tasks of source and target domains are different, then the transfer learning is called inductive learning [55]. For both types, transfer learning can be applied on instances or features. Instance-based learning searches for those samples that are very closed between source and target domains in order to reuse them in the target domain. However, feature-based transfer learning allows training samples from different feature spaces reducing effort for the learning classifier [55].

In the current research, we focus on using feature-based inductive transfer learning of three pre-trained deep learning models (GoogleNet, ResNet50, and ResNet101).

3.2.2.2. Deep Learning (DL)

For many years, old Machine Learning ML trials to solve complicated problems using enhancement on the traditional methods had failed. DL methods achieve high performance in many applications like image recognition, big data analysis, natural language processing, speech recognition, etc. [56]. The main training algorithm of the deep neural network is the backpropagation, in which the training is applied in two stages (forward step to compute error and backward step to modify weights and learn). The most common image recognition deep learning network is the convolutional neural network (CNN).

3.2.2.3. Convolutional Neural Network (ConvNets)

ConvNet is a deep learning network consisting of two layers: convolution and pooling. Each convolution layer has units called feature maps which store the result of convolution applied to the input image of the convolution layer [56]. In each layer, many filters (kernels) are applied to the input image, and then the Relu non-linear function is applied

to add some non-linearity. The results are called activation maps. The next layer is the max-pooling layer, in which the dimensions of the convolution are reduced to minimize computational time. The output of this combination (Conv-Relu-Pooling) is passed to the next combination of layers. The values of each filter (kernel) represent the weights of the networks, which will be changed through training until reaching the best values (learning) [57].

At the end of the convolution-pooling combination, there must be a fully connected layer (FC) before computing the last output (within the classification layer). FC aims to reshape the feature map into a single vector, so if we want to get features instead of classes, we can take the output of this layer. A dropout layer is sometimes used to drop a percentage of neurons (units) of the FC layers to avoid overfitting. The activation function of the last layer is the softmax which produces output as probabilities of all classes, and the class with the highest probability will be chosen. ConvNet architecture is illustrated in figure (3.4).

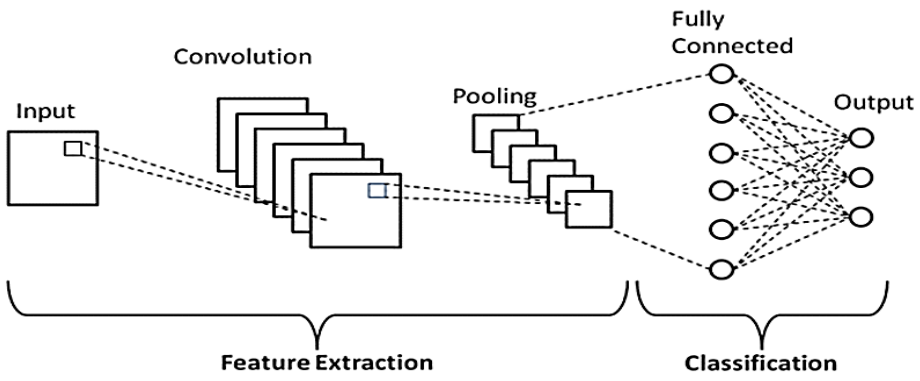

Figure 3.5. Illumination correction steps on a sample of the iris dataset.

3.2.2.4. Some Deep Learning Keywords

Padding and Stride [56]: When applying the filter kernel on the image inside the convolution layer, two principles must be defined, which are the padding and the stride. The padding is required to process the pixels on the border of the image since they do not match the entire kernel, and the image must be padded. If we choose not to pad the image,

then the activation map resulting of the convolution will be smaller than the original. If we pad the image using zeros, the padding value will be P=Floor((F-1)/2), where F is the kernel size. The size of the input and output in case of padding will be the same as shown in figure (3.5).

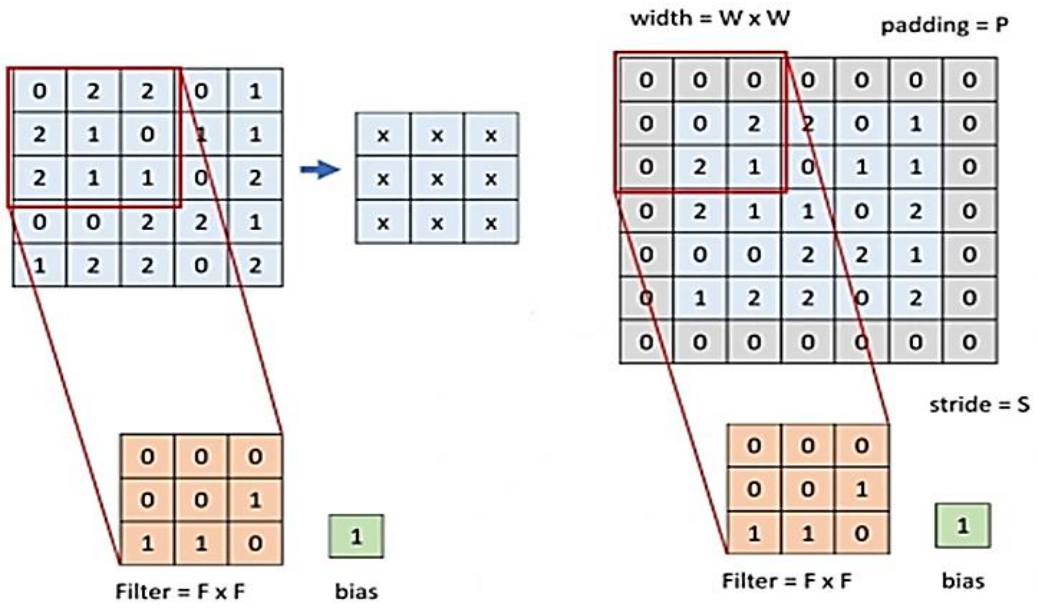

Figure 3.6. Convolution with zero-padding [58].

On the other hand, Stride is the sliding parameter by which the window of the kernel is moving horizontally and vertically from the pixel to the next one. The size of the convolution is (W – F + 2P) / S + 1; where W is the image size, F is the kernel size, P is the padding, and S is the stride. If we have an image of size 100x100 with kernel 7x7, padding of 3 and stride of 3, then the convolution result will be of size (100 – 7 + (2)(3)) / 3 + 1 = 34×34.

3.2.2.5. GoogleNet [64]

GoogleNet is a deep learning convolutional neural network with 22 layers and five pooling layers, first proposed by Szegedy et al. in the ILSVRC14 challenge. The main aim of this deep network was to minimize computational time by using hardware resources efficiently.

The input of GoogleNet is an image of size 224*224. The main component of this network is the inception layer, in which the computations are done in a parallel way. The first convolutional layer consists of two filters of size 7*7, which reduces the input image and extracts valuable information. In the second convolutional layer, the input is minimized by a factor of 4, while it is reduced by a factor of 8 before the first inception layer. At the first inception layer, the image size is 28*28*256, which means that the image size is reduced, but we have 256 activation maps. Figure (3.7) shows the architecture of the nine inception layers within GoogleNet. The 1x1 convolution is useful for dimensionality reduction. Between some inception layers, a max-pooling layer is used to down-sample the input and minimize the amount of data that will be delivered to the next layer. There are four layers at the end of GoogleNet architecture as shown in figure (3.8) (Global average pooling, dropout, linear, and classification). The global average pooling layer acts as a fully connected layer in which the feature vector is transformed to a vector of size 1x1x1024. The dropout layer is used to prevent overfitting by dropping 40% of the network's neurons. The linear layer contains 1000 elements corresponding to the 1000 classes of the ImageNet dataset. The last layer is the softmax layer, in which the probability distribution of each class (of the 1000 classes).

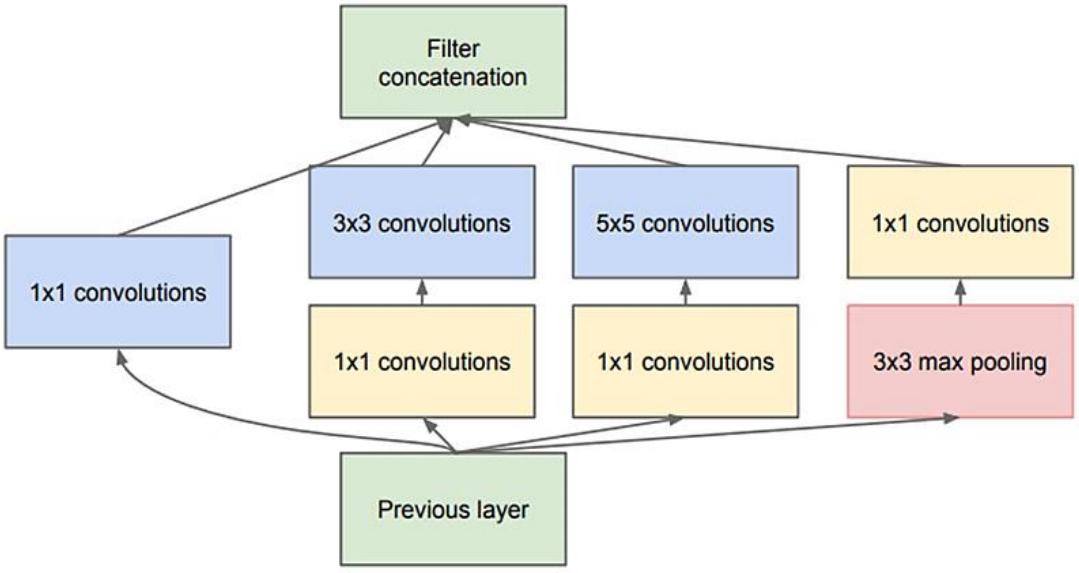

Figure 3.7. Inception layer inside GoogleNet [59,60].

type	patch size/ stride	output size
convolution	7×7/2	112×112×64
max pool	3×3/2	56×56×64
convolution	3×3/1	56×56×192
max pool	3×3/2	28×28×192
inception (3a)		28×28×256
inception (3b)		28×28×480
max pool	3×3/2	14×14×480
inception (4a)		14×14×512
inception (4b)		14×14×512
inception (4c)		14×14×512
inception (4d)		14×14×528
inception (4e)		14×14×832
max pool	3×3/2	7×7×832
inception (5a)		7×7×832
inception (5b)		7×7×1024
avg pool	7×7/1	1×1×1024
dropout (40%)		1×1×1024
linear		1×1×1000
softmax		1×1×1000

Figure 3.8. Architecture of GoogleNet [59].

3.2.2.6. ResNet [65]

Residual Nets (ResNet50) is a deep learning network with 50 layers. The input image size is 224*224, and the network classifies it into one of 1000 different classes. ResNet is trained on more than one million images of 1000 categories of the well-known dataset ImageNet. ResNet consists of 48 convolutional layers, one max-pooling, and one average pooling (FC) layer. This network solves the previous deep learning problem of overfitting when the model gets too deep, and the training error increases.

To solve this problem, He et al. [61] introduced a new architecture called the residual units, which are connections that performs the identity mappings (Figure (3.9)).

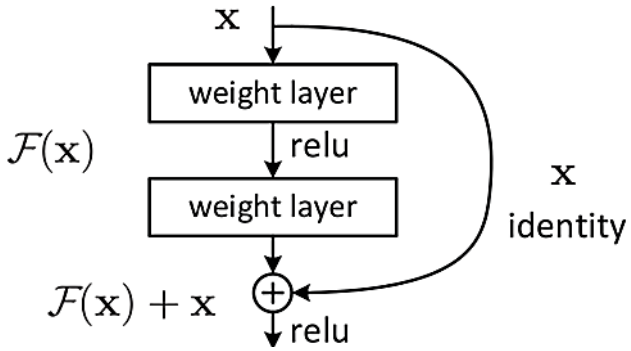

Figure 3.9. Residual units [61].

Additional parameters will be added to the model making it more powerful by adding the identity original value X to the output of each two layers (with Relu nonlinear function between them), so the nonlinear layers will fit the mapping of F(x): =H(x)-x, and the original mapping becomes F(x)+x. This extra connection adds no computational complexity to the model. Figure (3.10) shows that the training problem is solved using the Residual units (the deeper model is, the better performance).

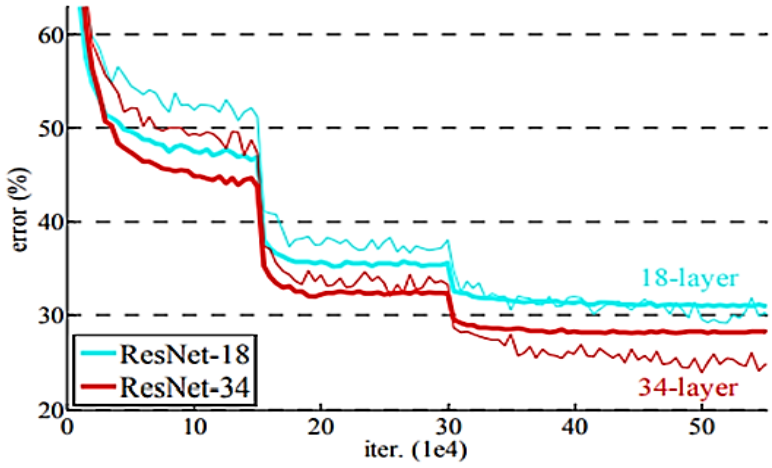

Figure 3.10. Two different ResNet and their corresponding performance [61].

Figure (3.11) illustrates the architecture of ResNet with 34 layers deep. For ResNet50 architecture, three layers inside the residual units (not two as previous original ResNet) as shown in figure (3.12).

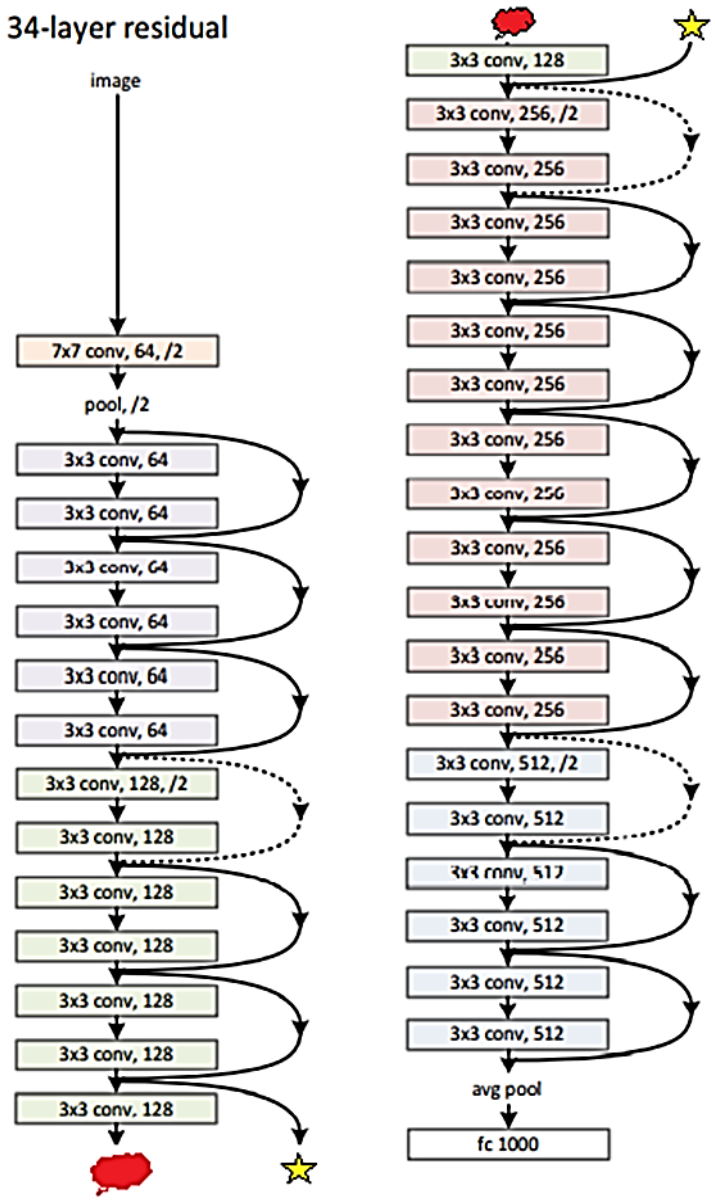

Figure 3.11. ResNet with 34 layers deep [61].

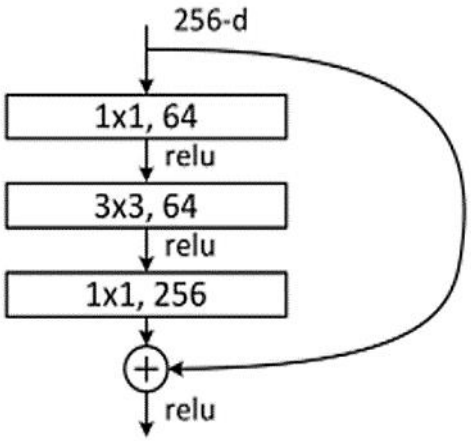

Figure 3.12. ResNet50 residual unit[61].

The architecture of ResNet50 is:

1- A convolutional layer with 64 different kernels (filters) of size 7x7 with a stride of size 2.
2- Max pooling layer with a stride of 2.
3- Three convolutional layers with the same architecture: 64 kernels of size 1x1 followed by 64 kernels of size 3x3, then 256 kernels of size 1x1. As a result, we get nine layers deep.
4- Four convolutional layers with the same architecture: 128 kernels of size 1x1, 128 kernels of size 3x3, and 512 kernels of size 1x1 getting 12 layers deep.
5- 256 kernels of size 1x1, 256 kernels of size 3x3, and 1024 kernels of size 1x1 repeated six times, constituting 18 layers deep.
6- The last convolutional combinations are 1x1, 512 kernels, 3x3, 512 kernels, and 1x1, 2048 kernels. This will produce nine layers deep.
7- The last fully connected layer is the average pooling layer consisting of 1000 nodes ending with the softmax classification function (this gives us one layer).
8- The sum of all previous layers is 50 layers deep, so we get the ResNet50.

Figure (3.13) shows the difference between ResNet50 and ResNet101 architectures.

layer name	output size	50-layer	101-layer
conv1	112×112	7×7, 64, stride 2	
conv2_x	56×56	3×3 max pool, stride 2 $\begin{bmatrix} 1\times1, 64 \\ 3\times3, 64 \\ 1\times1, 256 \end{bmatrix} \times3$	$\begin{bmatrix} 1\times1, 64 \\ 3\times3, 64 \\ 1\times1, 256 \end{bmatrix} \times3$
conv3_x	28×28	$\begin{bmatrix} 1\times1, 128 \\ 3\times3, 128 \\ 1\times1, 512 \end{bmatrix} \times4$	$\begin{bmatrix} 1\times1, 128 \\ 3\times3, 128 \\ 1\times1, 512 \end{bmatrix} \times4$
conv4_x	14×14	$\begin{bmatrix} 1\times1, 256 \\ 3\times3, 256 \\ 1\times1, 1024 \end{bmatrix} \times6$	$\begin{bmatrix} 1\times1, 256 \\ 3\times3, 256 \\ 1\times1, 1024 \end{bmatrix} \times23$
conv5_x	7×7	$\begin{bmatrix} 1\times1, 512 \\ 3\times3, 512 \\ 1\times1, 2048 \end{bmatrix} \times3$	$\begin{bmatrix} 1\times1, 512 \\ 3\times3, 512 \\ 1\times1, 2048 \end{bmatrix} \times3$
	1×1	average pool, 1000-d fc, softmax	
FLOPs		3.8×10^9	7.6×10^9

Figure 3.13. ResNet50 Vs. ResNet101 [61].

As Figure (3.13) shows, the number of FLOPs operations is 3.8*109 and 7.6*109 of ResNet50 and ResNet101, respectively.

3.2.2.7. GoogleNet and ResNet Comparison

Table (3.1) includes a comparison between the three deep learning models (GoogleNet, ResNet50, and ResNet101) [59,61–63]

Table 3.1. Deep Learning Architecture comparison.

	GoogleNet	ResNet50	ResNet101	Input size
No. Parameters	4 M	25.6 M	44.5 M	224x224
No. Layers (Depth)	22	50	101	224x224
Top5- error rate or ImageNet Validation dataset	7.89%	5.25%	4.60%	224x224

As shown in table (3.1), we can conclude that GoogleNet has the least number of parameters with the minimum computations. However, ResNet101 has the best accuracy, and ResNet50 is better than GoogleNet from an accuracy point of view and better than ResNet101 from computational time.

3.2.2.8. The Proposed Transfer Learning Models

In our study, the pre-trained models (GoogleNet, ResNet50, and ResNet101) will be modified to fit our goal (The iris recognition process). For each training scenario in our study, a specific number of classes will be obtained, different from the original classes of ImageNet (1000 classes). The idea is to modify the network architecture in order to fit the number of classes of our problem. Two layers in each model will be replaced by new ones: the fully connected (average pooling) layer and the classification layer. The FC layer's new size will be the number of classes of a specific scenario (for example, if the number of individuals in the iris dataset is 50, then the FC layer will be of size 50x1). After modifying the FC layer, the classification layer will also be modified to classify the input image into one of the new classes (50, for example). GoogleNet and ResNets software pre-trained models are available at MathWorks from these links. We need to download and use them in our recognition system [64,65].

3.3. PERFORMANCE EVALUATION

The following measures are instructed for evaluating our segmentation and recognition methodologies [69].

1- Segmentation Accuracy expresses the accuracy of the iris segmentation process and how close it is to detect the iris without any non-iris parts.
2- TP is the number of predictions in which the model succeeded in recognizing the correct individual based on an iris test image; for example, the iris test image is related to individual 1, and the model predicted that correctly.
3- FP is the number of predictions in which the model failed to recognize the correct individual based on an iris test image; for example, the iris test image is not related to any of the trained individuals, but the model predicted that it is related for some individual.
4- TN is the number of predictions in which the model succeeded in identifying the wrong iris test images; for example, the iris test image is not related to any of the trained individuals, and the model predicted that correctly.
5- FN is the false-negative predictive value. The number of predictions in which the model failed to recognize the wrong iris test images, for example, the iris test image is related to individual 1 of the trained datasets, but the model predicted that it is not related to any individual.
6- TPR is the proportion of correctly accepted samples out of all related test samples.
7- FNR is the proportion of incorrectly rejected iris samples out of all related test samples.
8- PPR is the portion of correctly classified iris samples out of all samples inside the predicted class.
9- FDR is the portion of incorrectly classified iris samples out of all inside the predicted class.
10- Classification Accuracy, which expresses the accuracy of the iris recognition process. The accuracy will be computed of training, validation, and test sets.

Figure (3.14) below illustrates the confusion matrix detailed calculations, including the way to compute TPR, FNR, PPR, and FDR of a classification problem consisting of three classes.

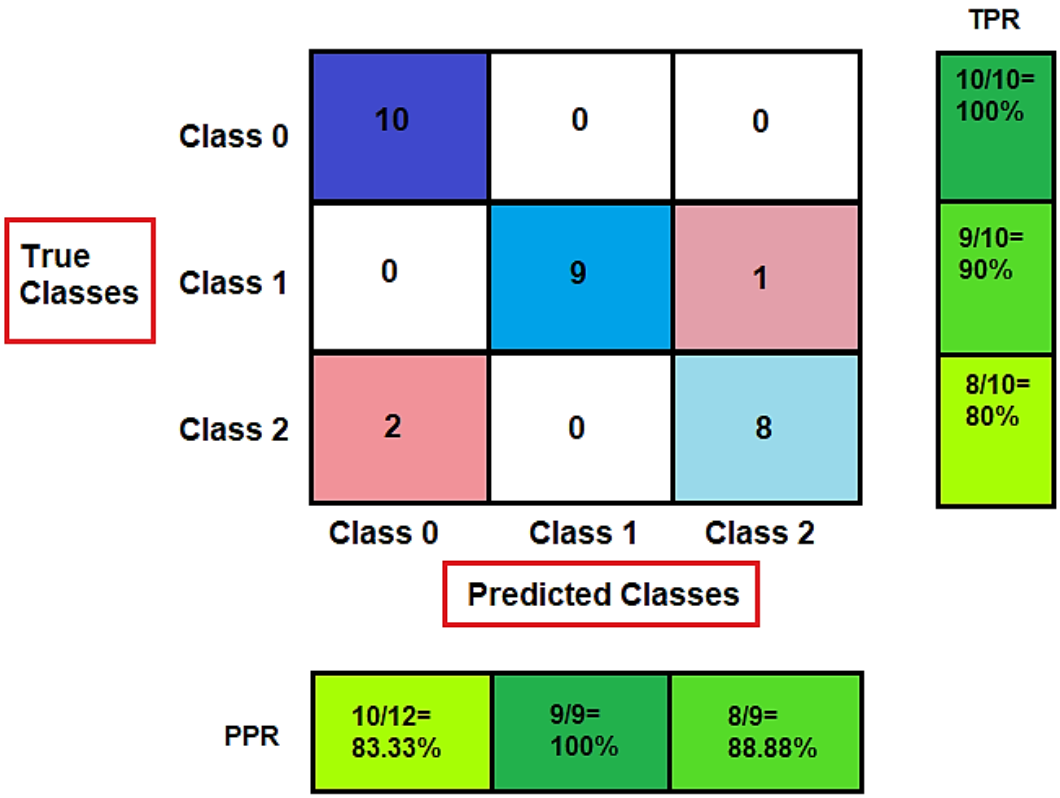

Figure 3.14. Confusion Matrix (CM) explanation [69].

TPR is the ratio of the blue values (i,i) of each row i^{th} of the CM to the sum of this row's values. On the other hand, PPR is the ratio of the blue values of each column i^{th} to the sum of this column's values. FNR and FDR are the opposite values of TPR and PPR, respectively. The high TPR proves the system's sensitivity against false negatives, while the high PPR refers to a low number of false positives.

PART 4

RESULTS

4.1. INTRODUCTION

In this chapter, many training and test scenarios will be applied on the proposed datasets. Two main results will be introduced: the segmentation and recognition results.

4.2. SEGMENTATION RESULTS

The true segmentation rates TSRs are 90.5%, 87.62%, and 98.03% for Warsaw V1, Warsaw V2, and CASIA, where the total samples are 684 of Warsaw v1, 1793 of Warsaw v2, and 2639 of CASIA datasets.

4.2.1 Warsaw V1 Dataset Segmentation Results

The Warsaw V1 dataset includes 684 medical cases of individuals with different diseases for both left and right eyes. Table Appendix (A.1) contains detailed information of each disease case's True and False segmentation.

4.2.2 Detailed Segmentation Results

Figure (4.1) includes the statistical segmentation results of the left and right eyes. Some pupil diseases have effects on the segmentation result while others do not. However, in some mixed-diseases cases containing distortion or deforming of iris, segmentation errors arose.

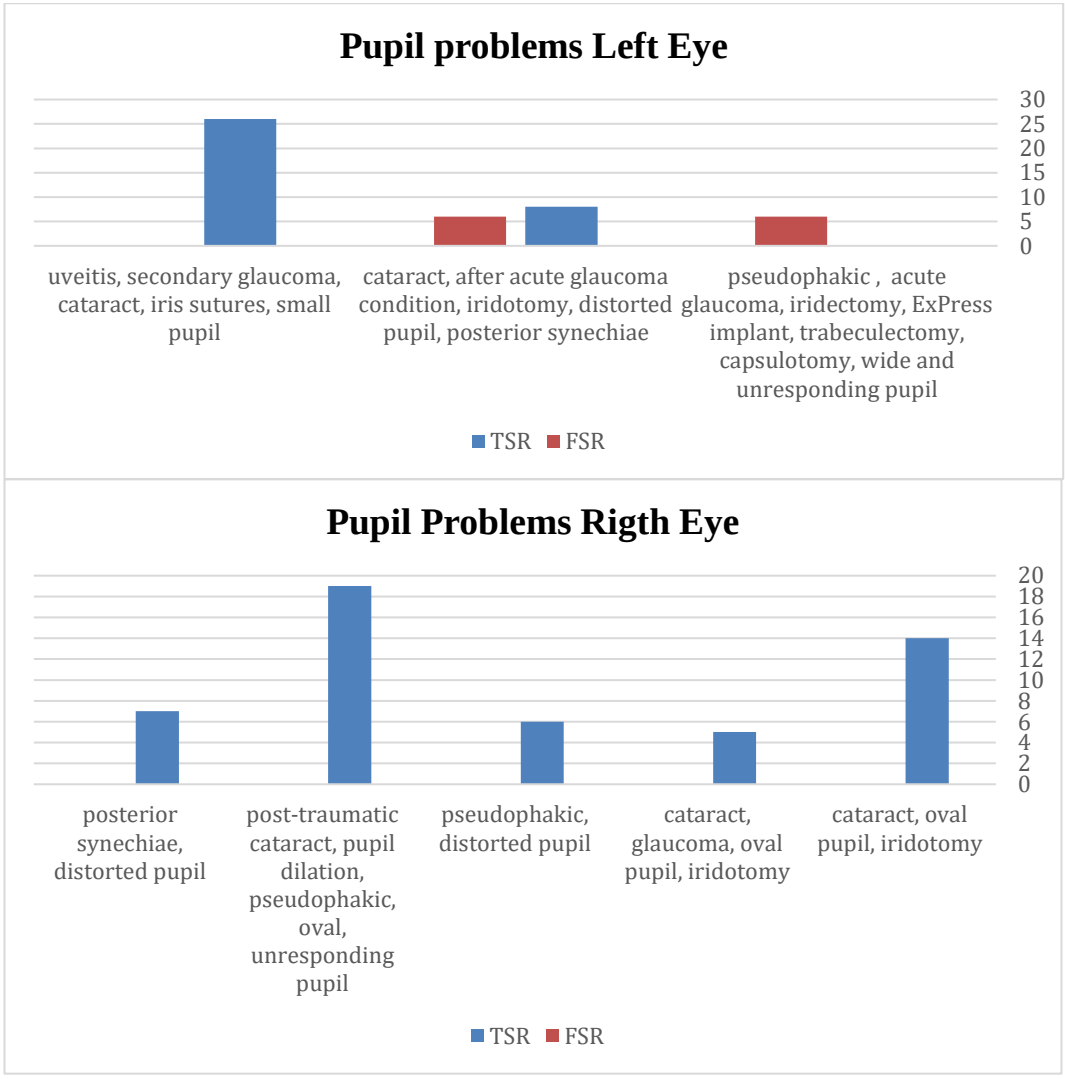

Figure 4.1. Segmentation results in case of pupil diseases.

For retinal diseases, the detachment and retinal diseases corresponding with blindness affect the segmentation process significantly, as shown in figure (4.2).

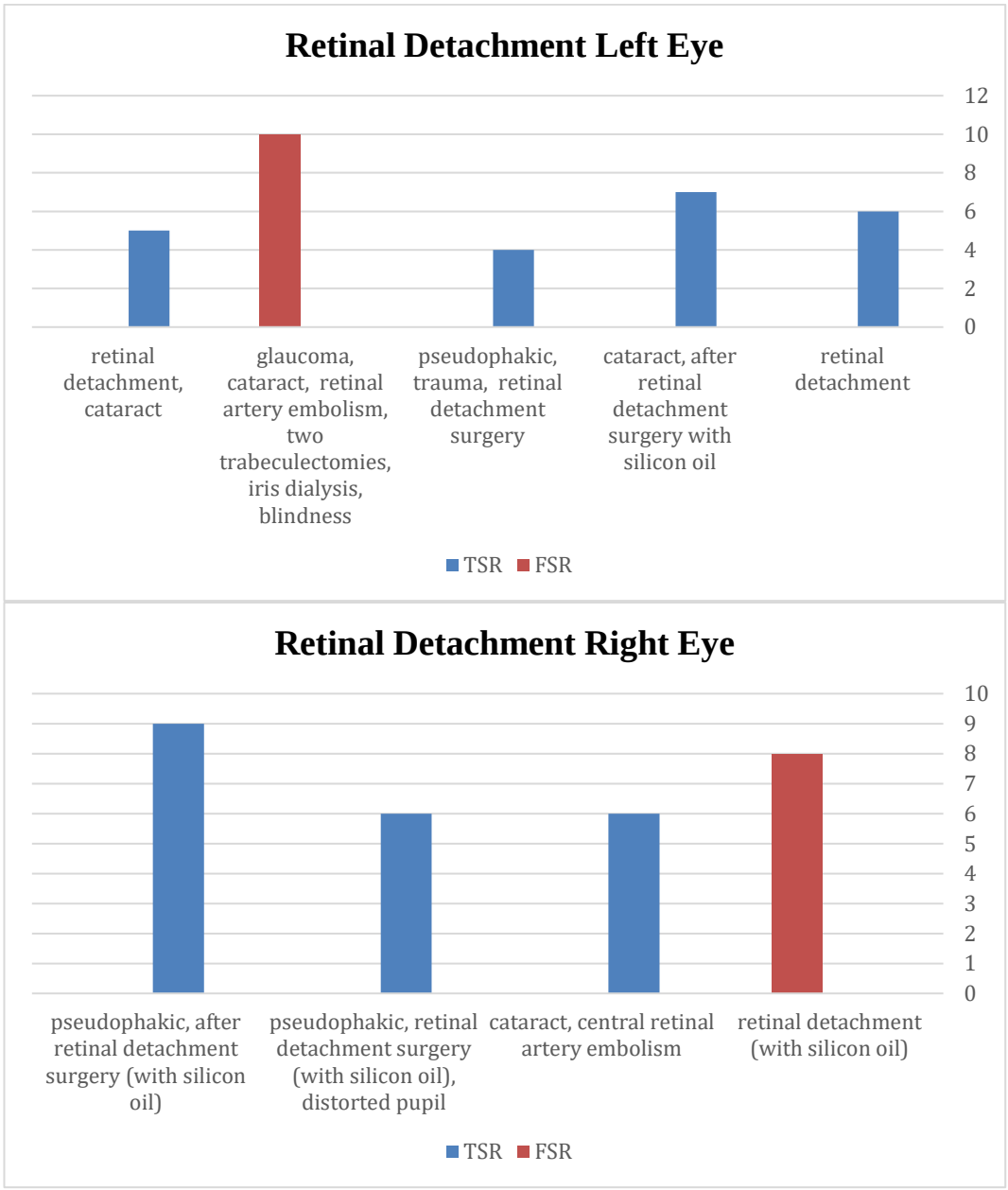

Figure 4.2. Segmentation results in case of Retinal diseases.

In both Corneal and Trauma problems, the diseases do not affect the segmentation process, as shown in figures (4.3) and (4.4).

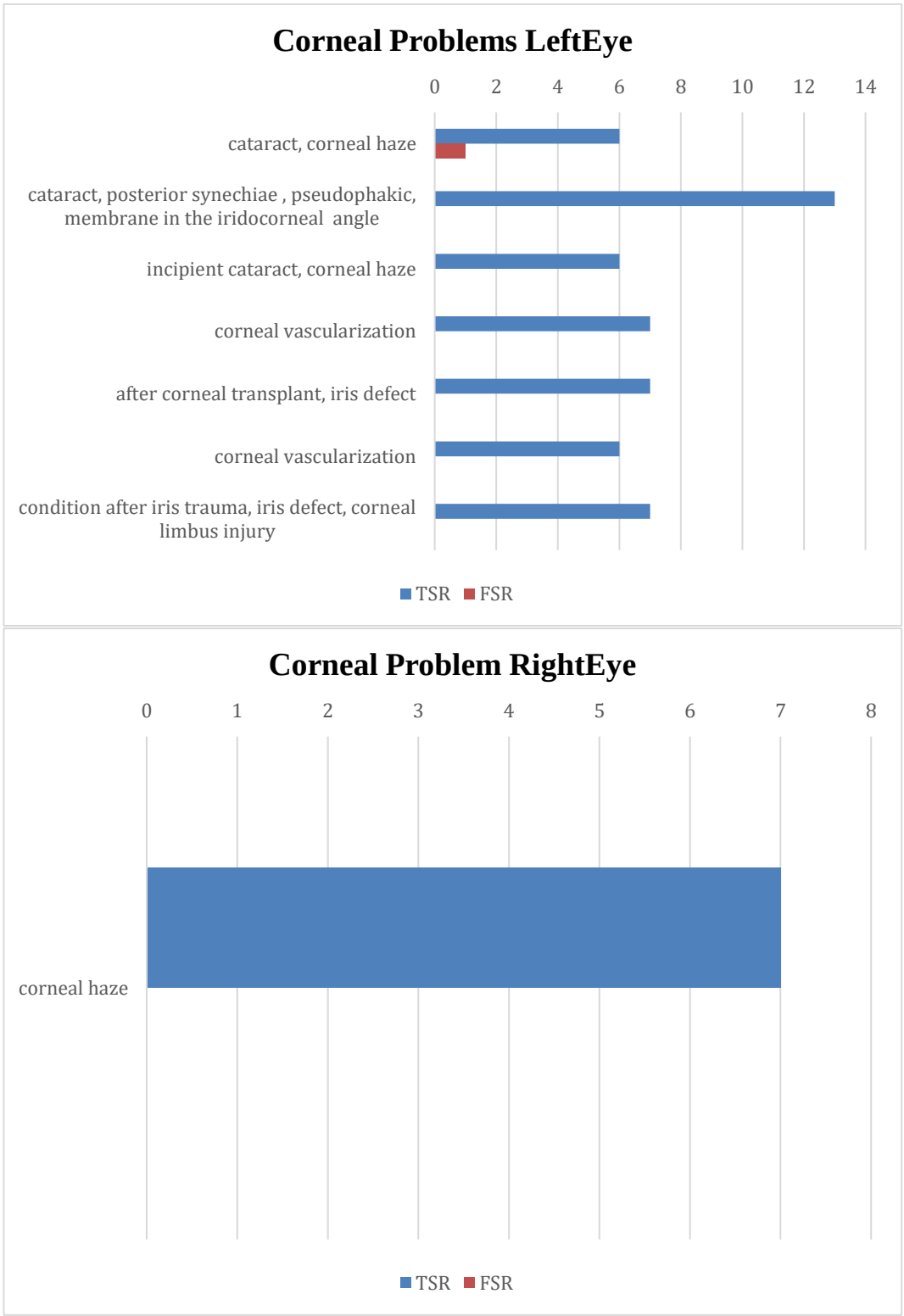

Figure 4.3. The segmentation results in case of Corneal diseases.

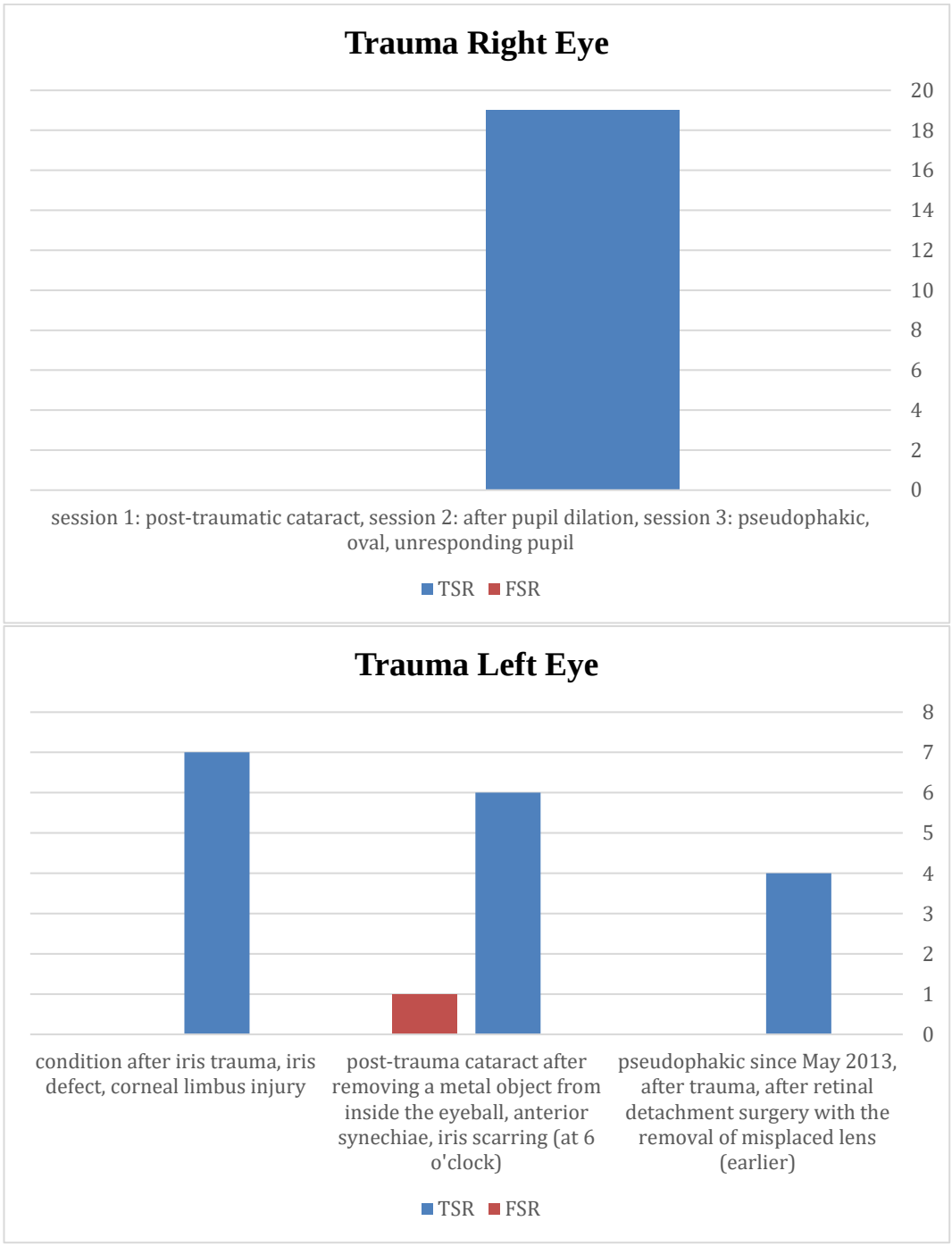

Figure 4.4. The segmentation results in case of Trauma.

Some cases include iridectomy problems accompanying other diseases. The segmentation errors in these cases are not related to iridectomy itself rather, they are caused by other diseases, as figure (4.5) illustrates.

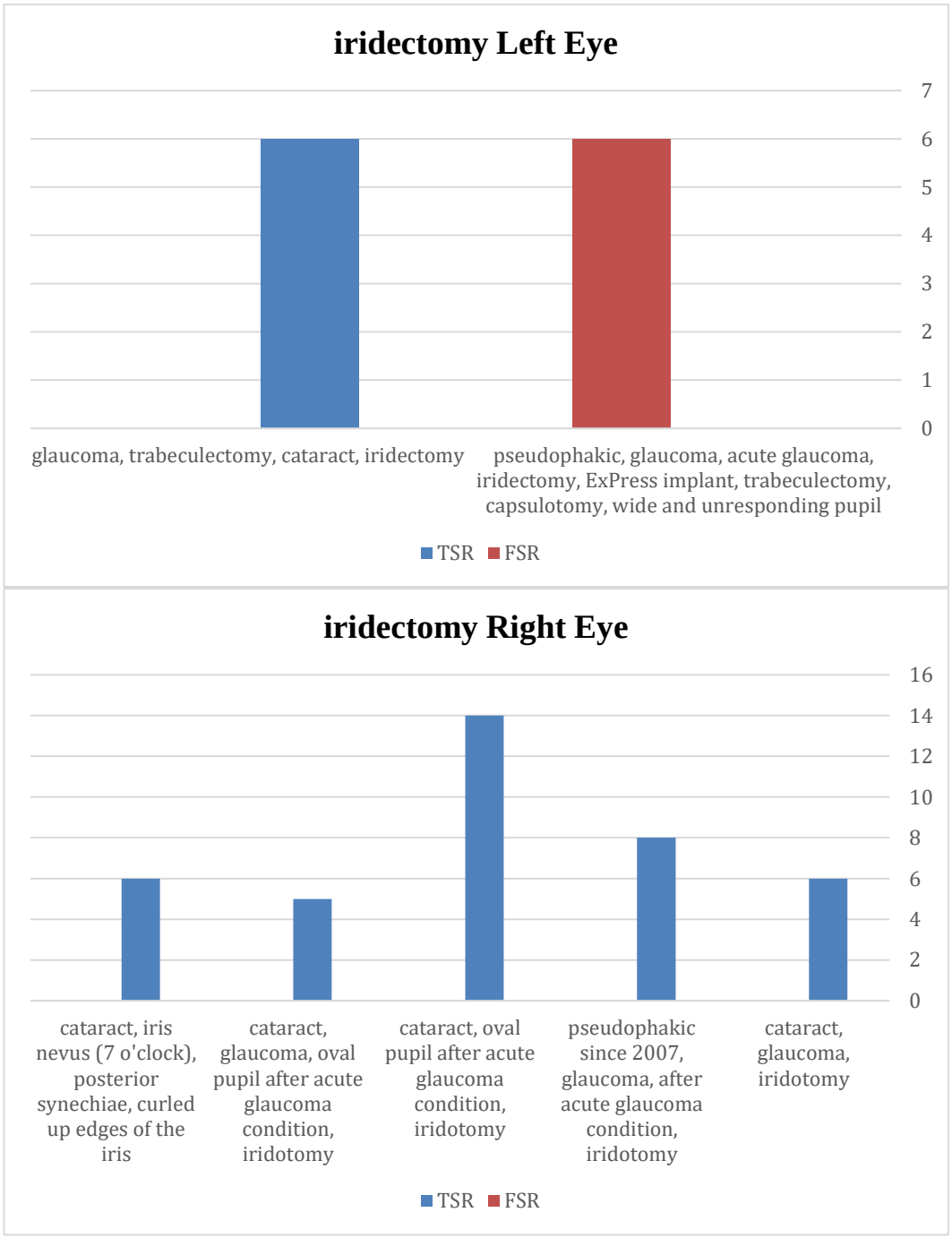

Figure 4.5. The segmentation results in case of iridectomy.

The posterior synechiae disease can cause problems for iris segmentation in both single and mixed diseases cases. However, as figure (4.6) shows, the posterior iris Synechiae can cause more problems than the anterior type.

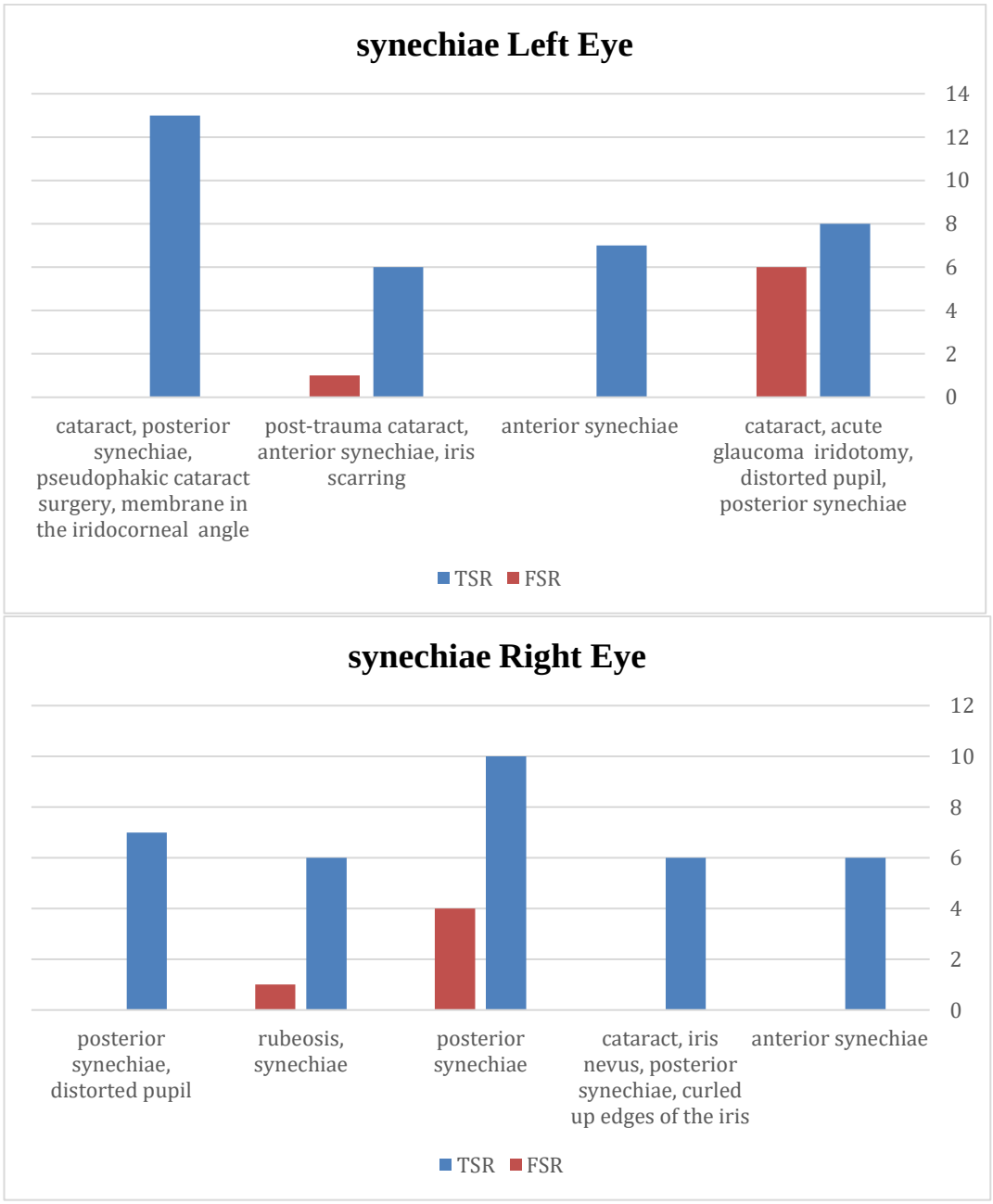

Figure 4.6. The segmentation results in case of Synechiae diseases.

The blindness disease affects the segmentation process awfully. Figures (4.7) illustrate this conclusion.

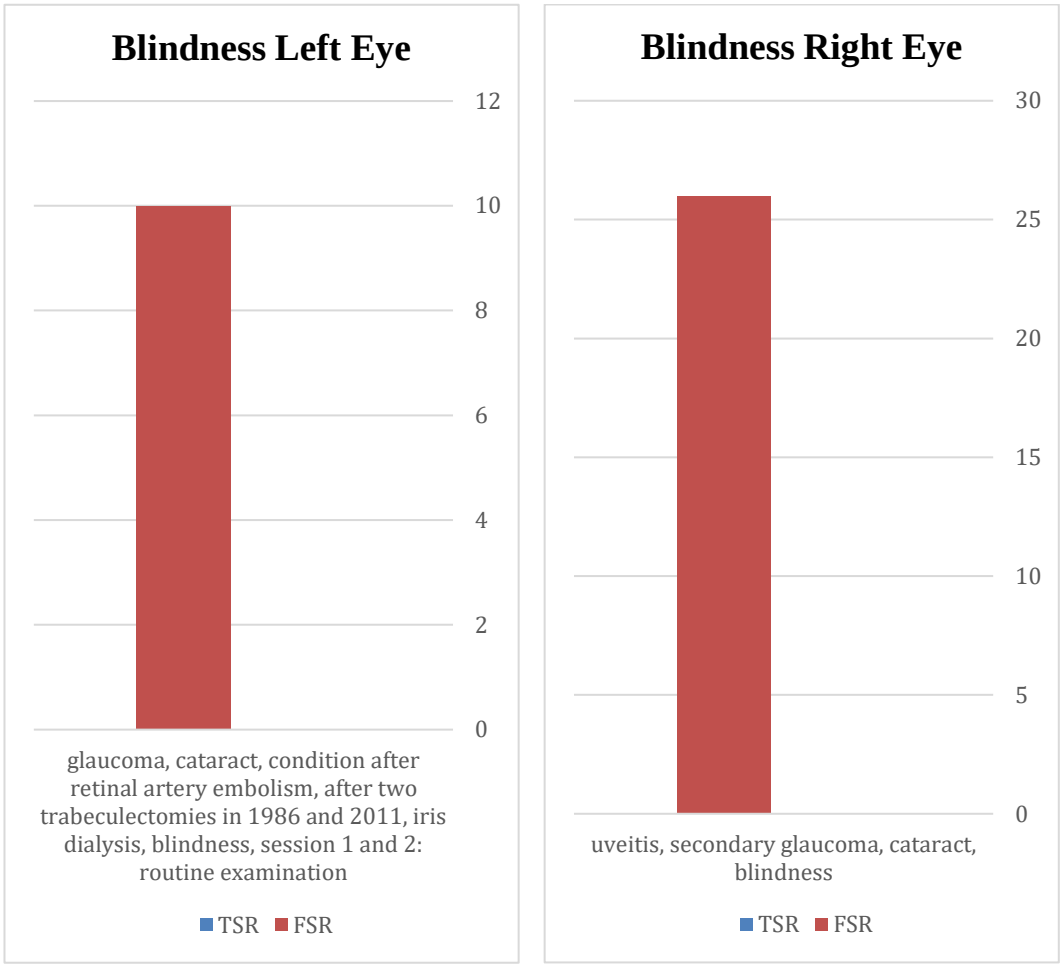

Figure 4.7. The segmentation results in case of Blindness.

The most common diseases (Cataract and Glaucoma) are described in figures (4.8) and (4.9), respectively. For Both diseases, the single disease situation has no effects on the segmentation process. Still, in the case of mixed disease (Blindness, posterior synechiae, corneal haze, distorted pupil, iridotomy, etc.), there are some situations in which the iris segmentation may get affected.

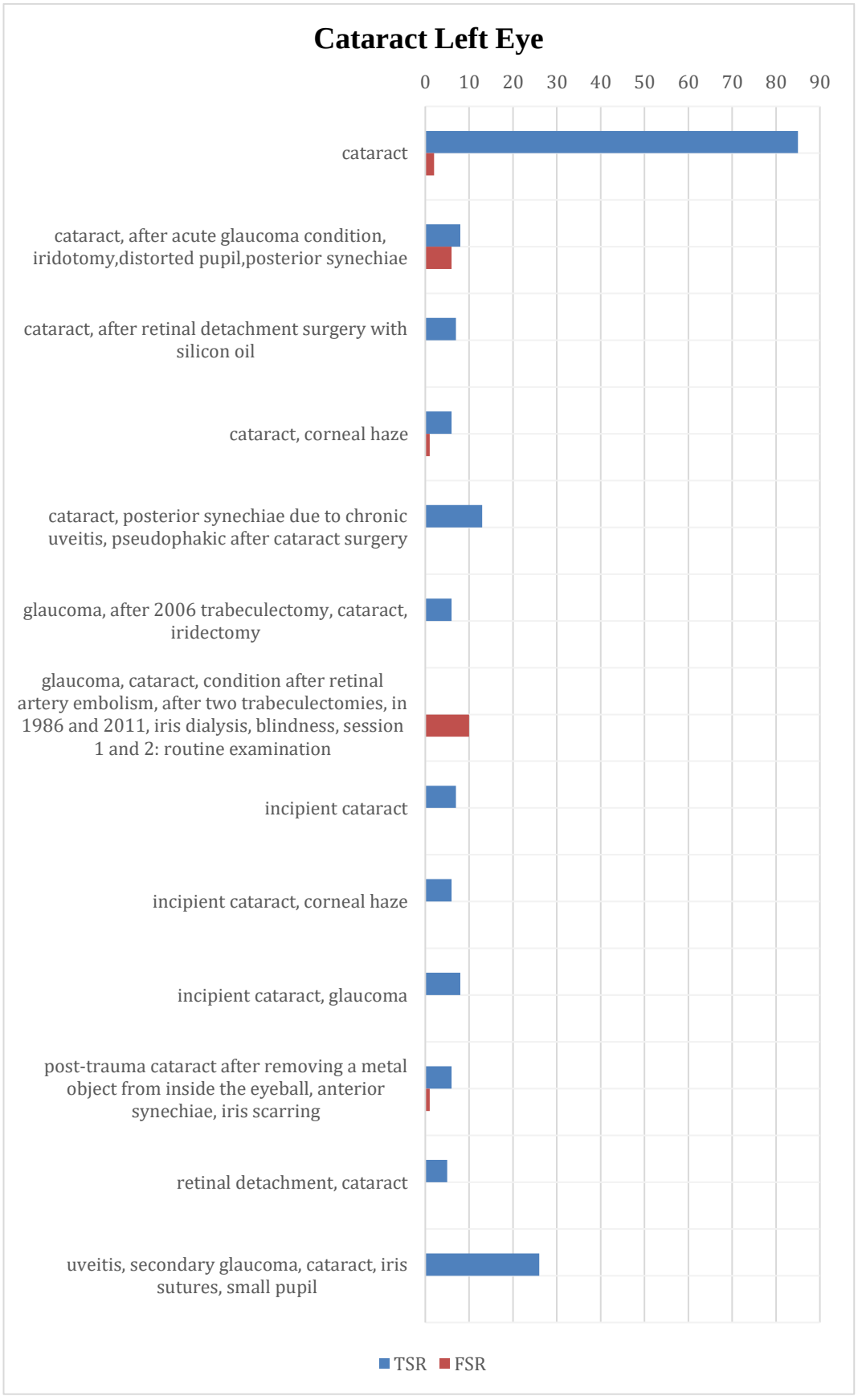

Figure 4.8. (A) The segmentation results in case of Cataract diseases of Left Eye.

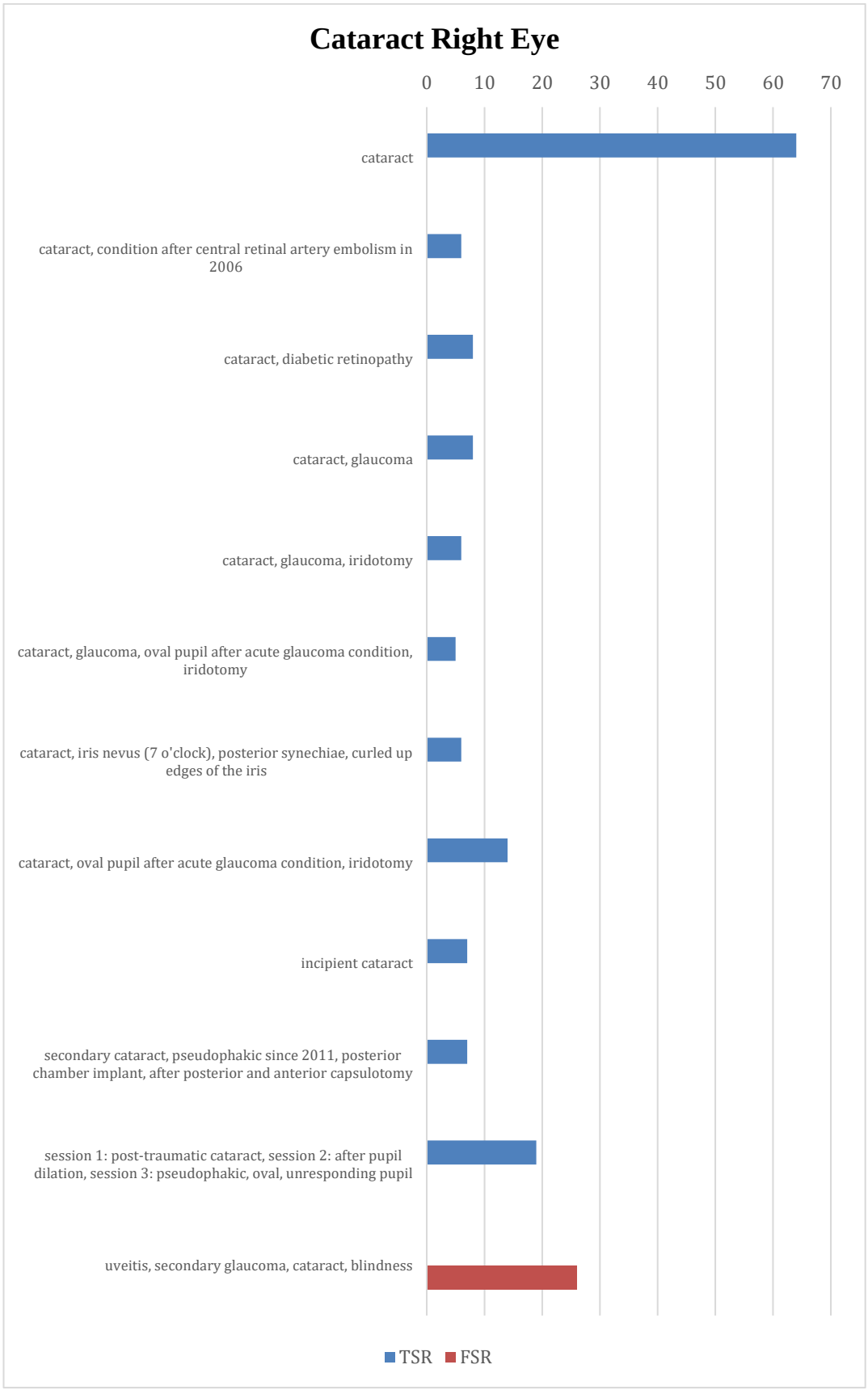

Figure 4.8. (B) The segmentation results in case of Cataract diseases of Right Eye.

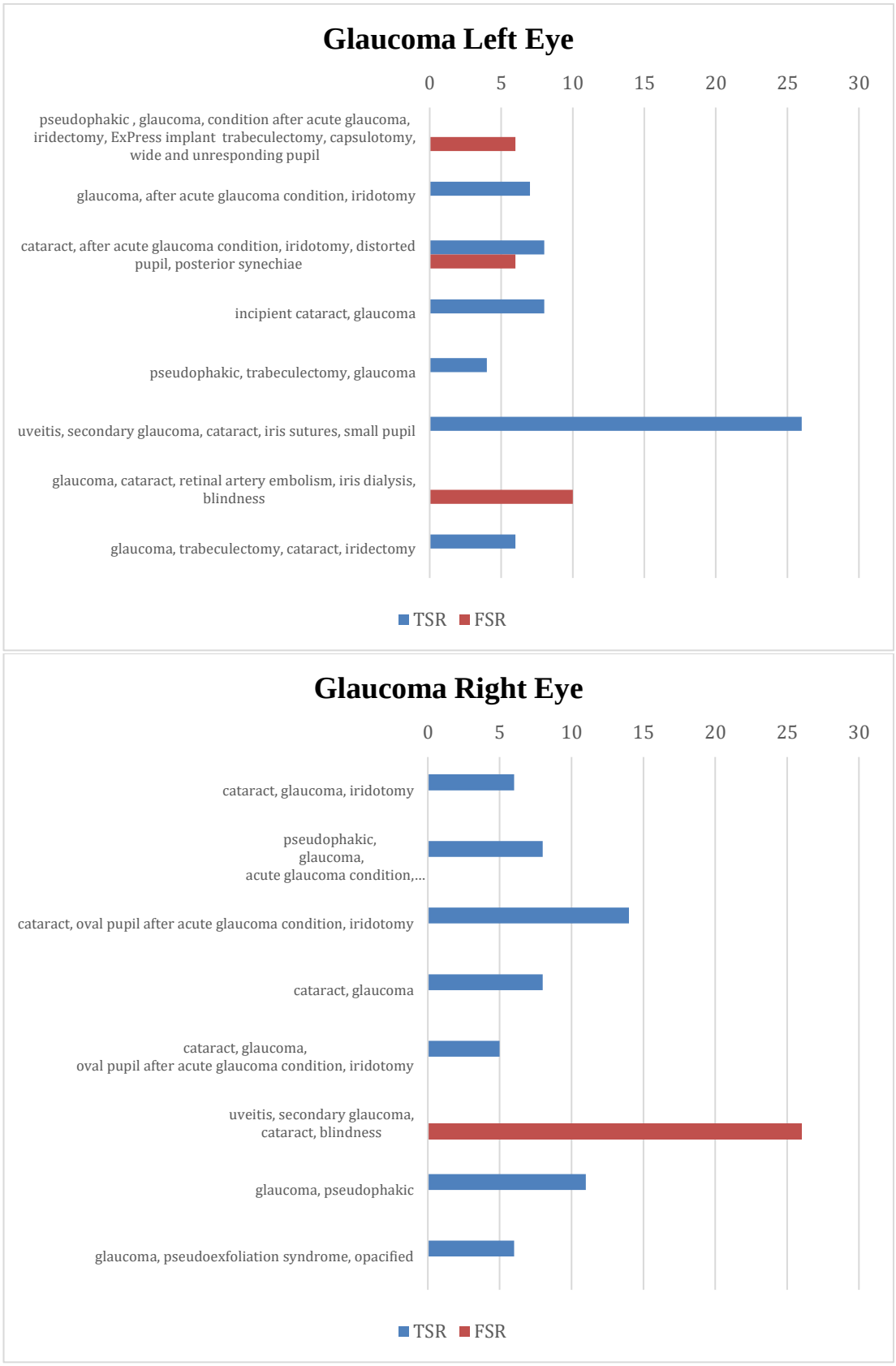

Figure 4.9. The segmentation results in case of Glaucoma diseases.

4.2.3. Warsaw V2 Dataset Segmentation Results

The Warsaw V2 dataset includes 1793 medical cases of individuals with different diseases for both left and right eyes. Table Appendix (A.2) includes detailed information of each disease case's True and False segmentation.

Two categories are inferred for the Warsaw V2 segmentation; the first category of diseases is similar to the Warsaw V1 diseases, while the second category contains new diseases that do not appear in the V1 dataset.

4.2.4. Similar V1 Diseases

In the case of a distorted pupil, the other accompanying diseases (such as eye trauma, cataract, iridotomy, adhesion, etc.) can cause some segmentation errors, as shown in Figure (4.10). Includes the statistical segmentation results of the left and right eyes in case of Pupil diseases.

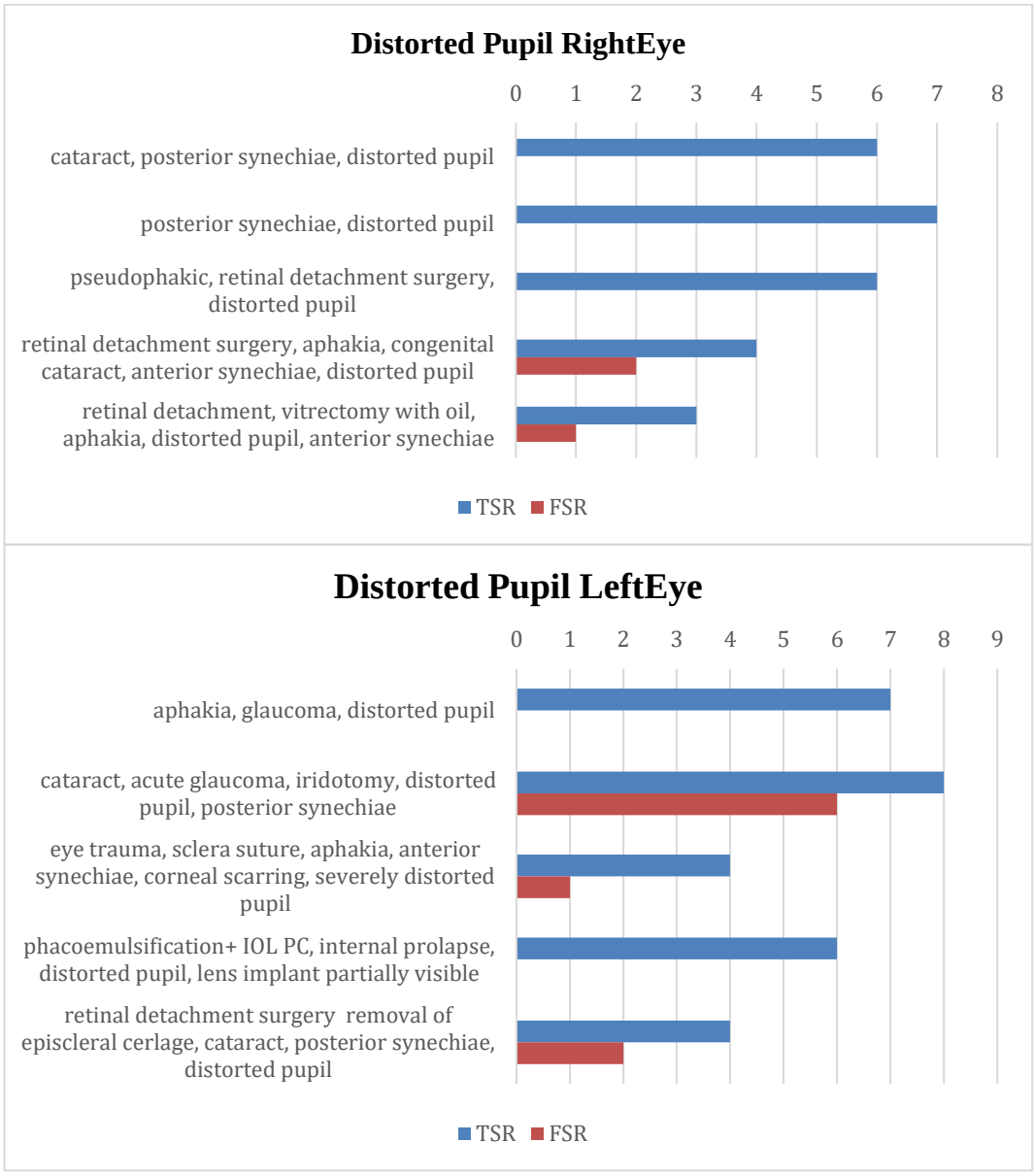

Figure 4.10. The segmentation results in case of Pupil diseases.

For healthy eyes, the segmentation process has no errors, as illustrated in following figure (4.11).

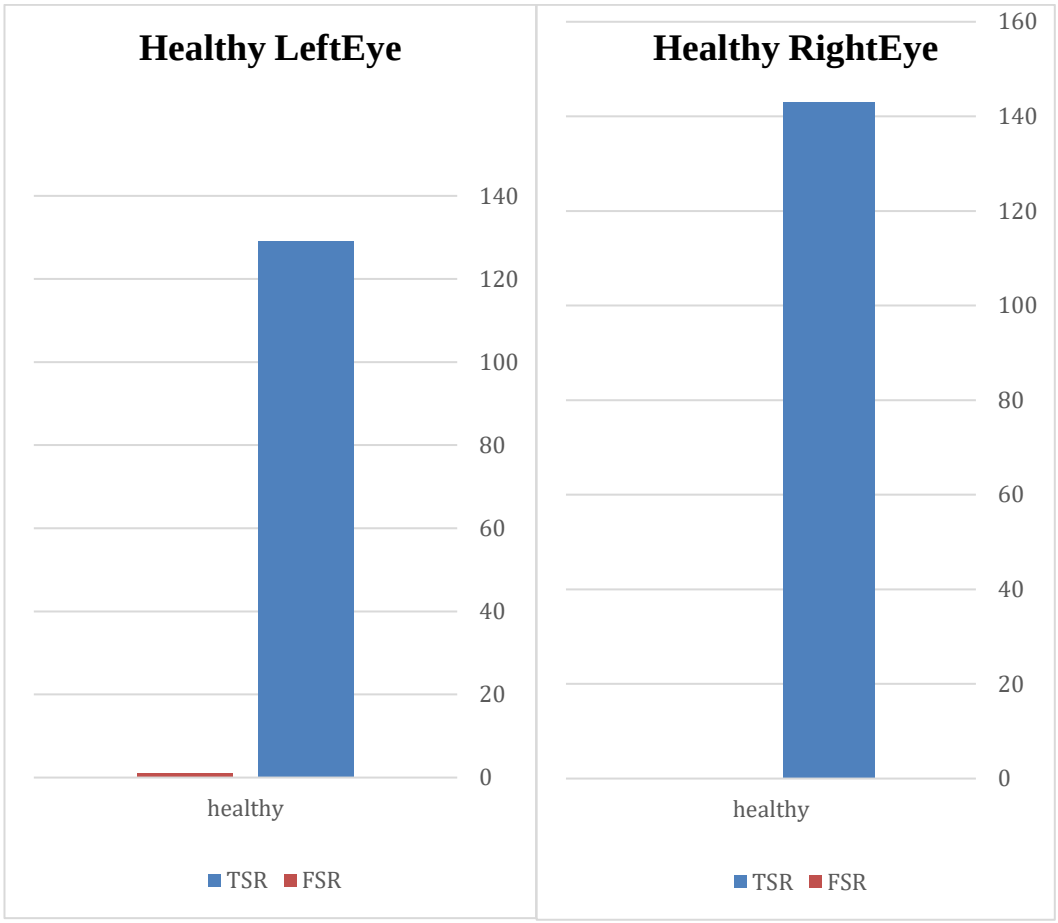

Figure 4.11. The segmentation results of healthy eyes.

The blood in the eyes (which is a temporary situation of eye diseases) causes fundamental problems for iris segmentation. Figure (4.12) shows the segmentation results of both left and right eyes in the case of "bloody eyes."

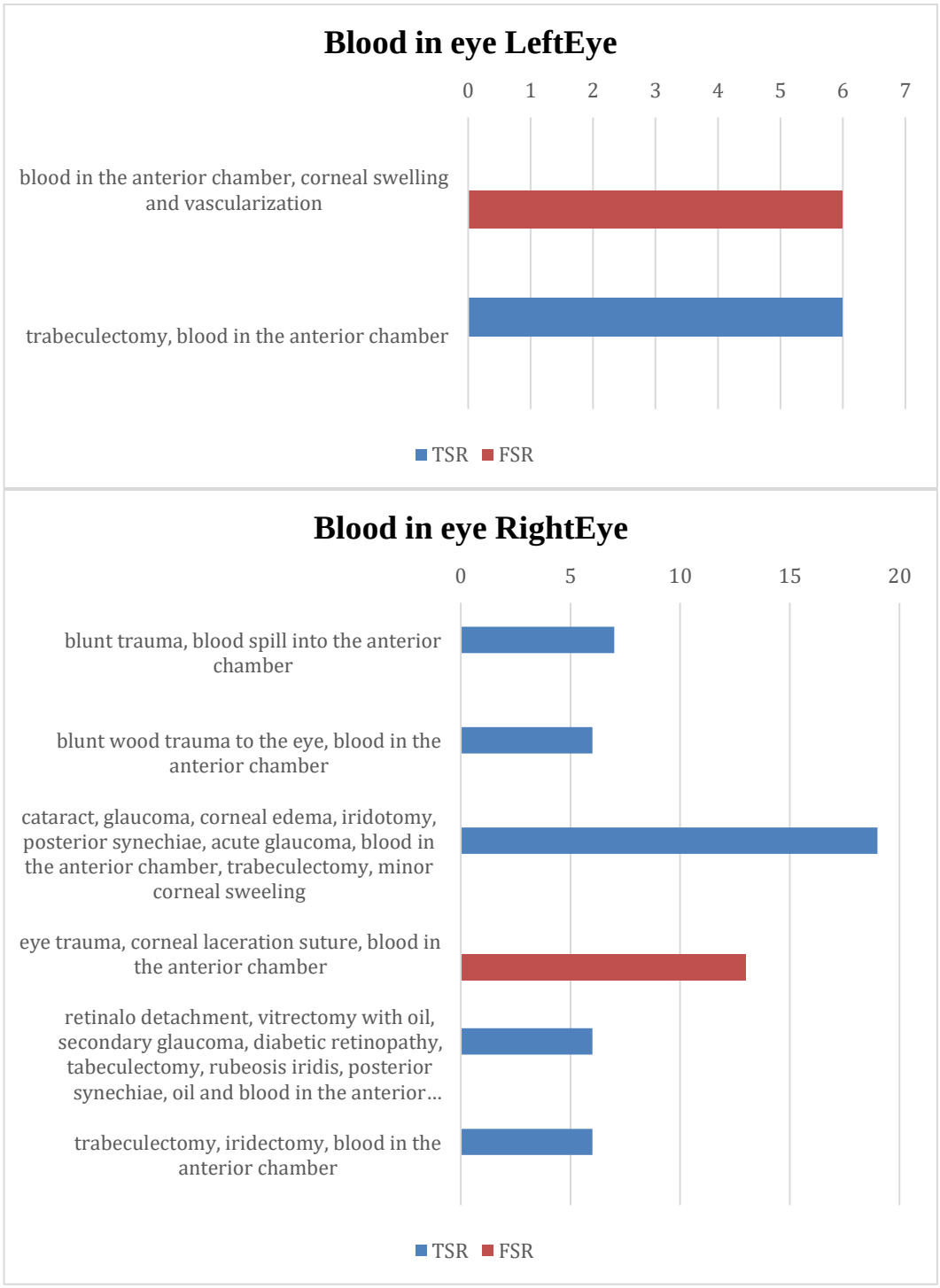

Figure 4.12. The segmentation results of bloody eyes.

Retinal detachment problem is an essential eye disease in which the iris segmentation is usually affected. Figure (4.13) shows the right and wrong cases in which Retinal detachment exists either individually or mixed with other accompanying diseases.

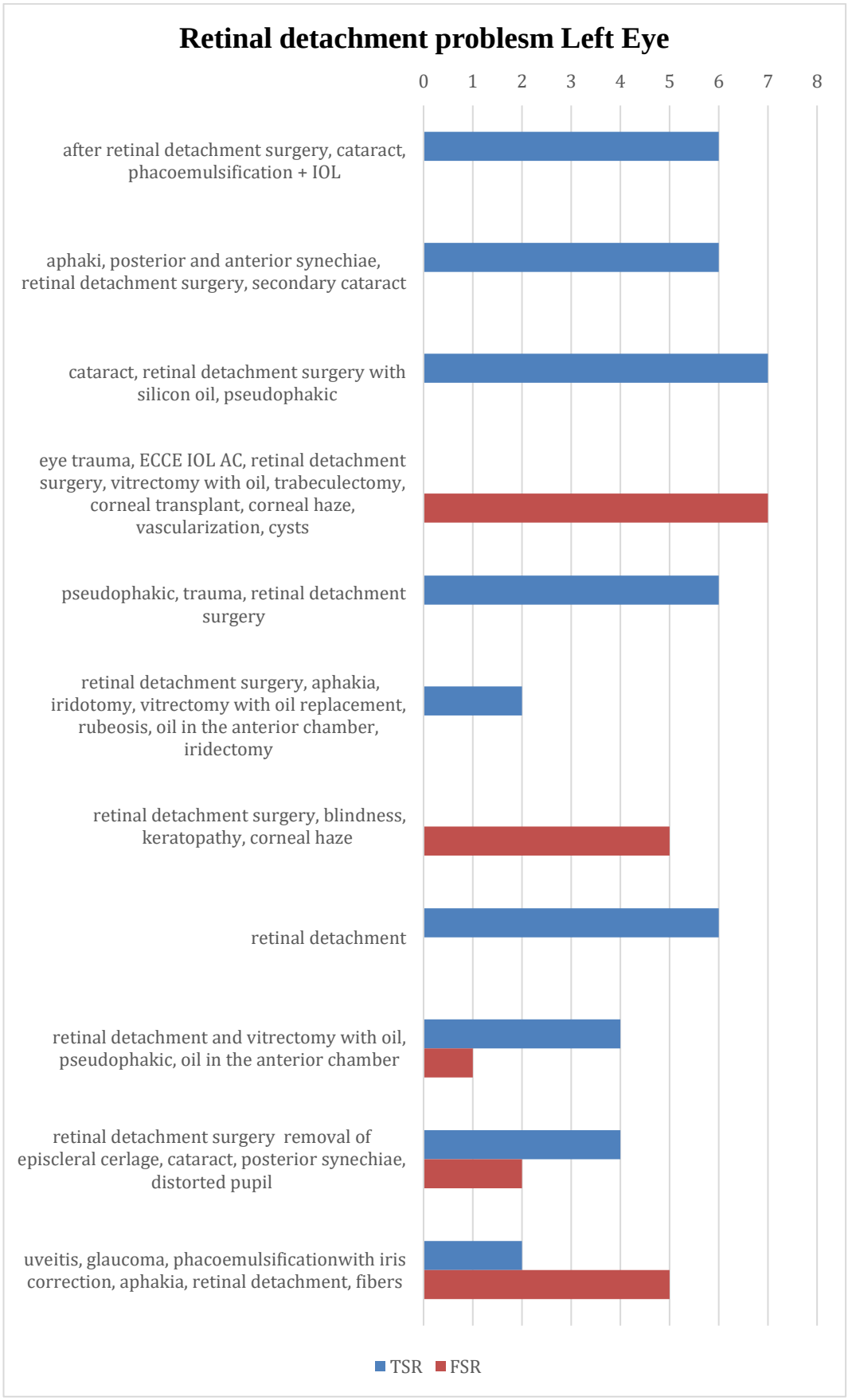

Figure 4.13. (A) The segmentation results of Retinal Detachment Left Eye.

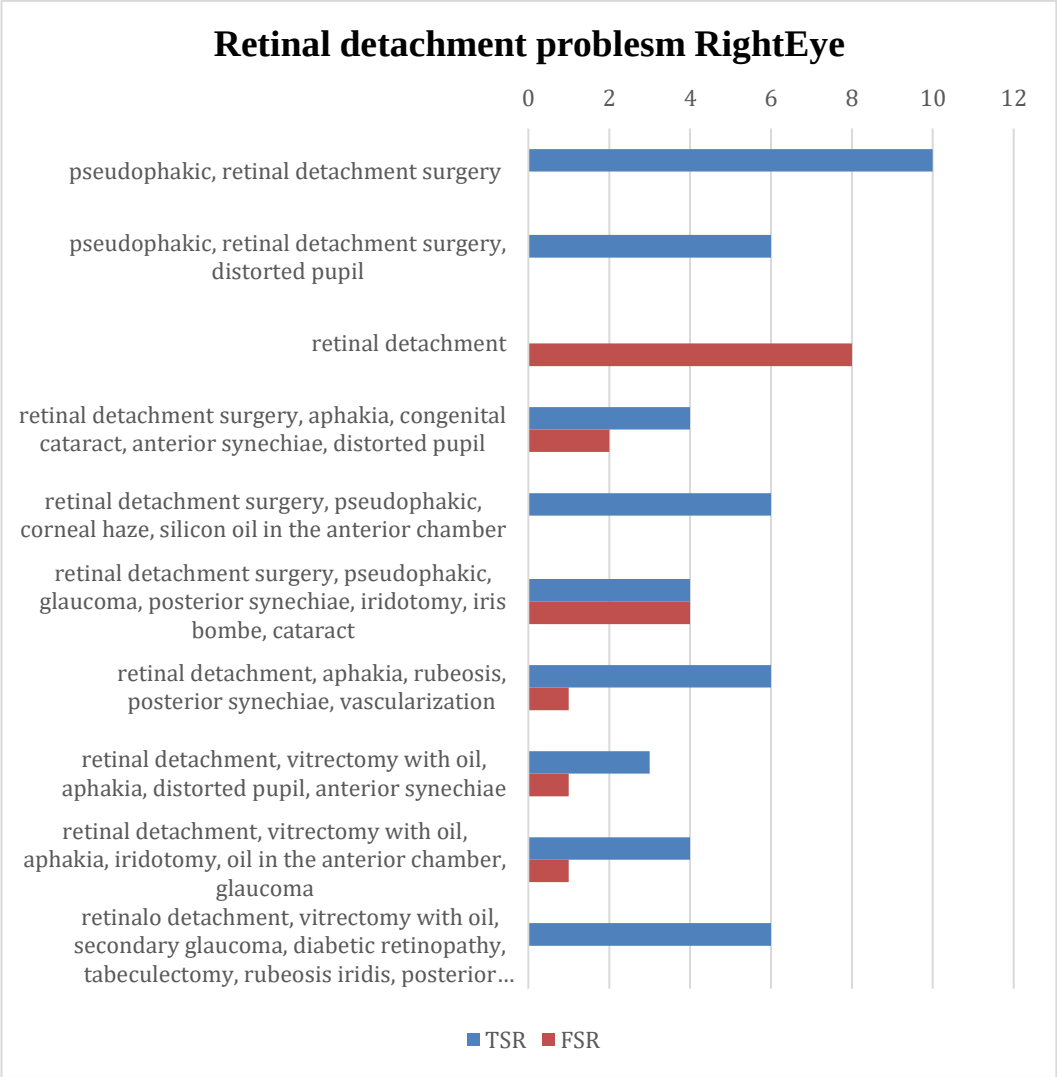

Figure 4.13. (B) The segmentation results of Retinal Detachment Right Eye.

The iridectomy cases appears mixed where other accompanying diseases also exist. Figure (4.14) shows situations of iridectomy in which many other diseases are there. The segmentation errors occur in case of pupil problems and some other complex situations of multiple eye disease.

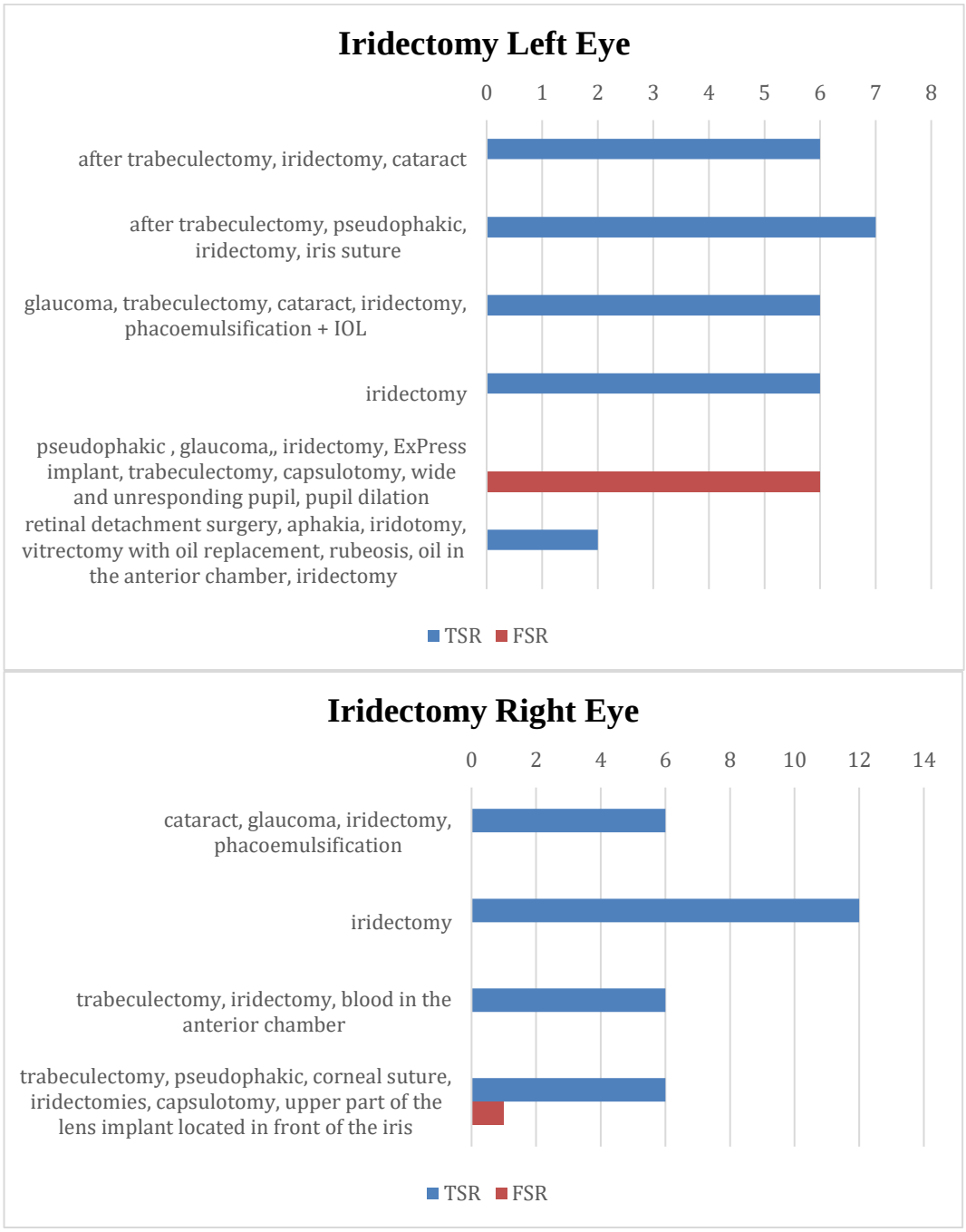

Figure 4.14. The segmentation results in case of Iridectomy cases.

Blindness is one of the worst eye diseases in which the iris is almost invisible. Figure (4.15) shows the left and right eye segmentation processes where eyes have blindness issues, and the segmentation is almost incorrect.

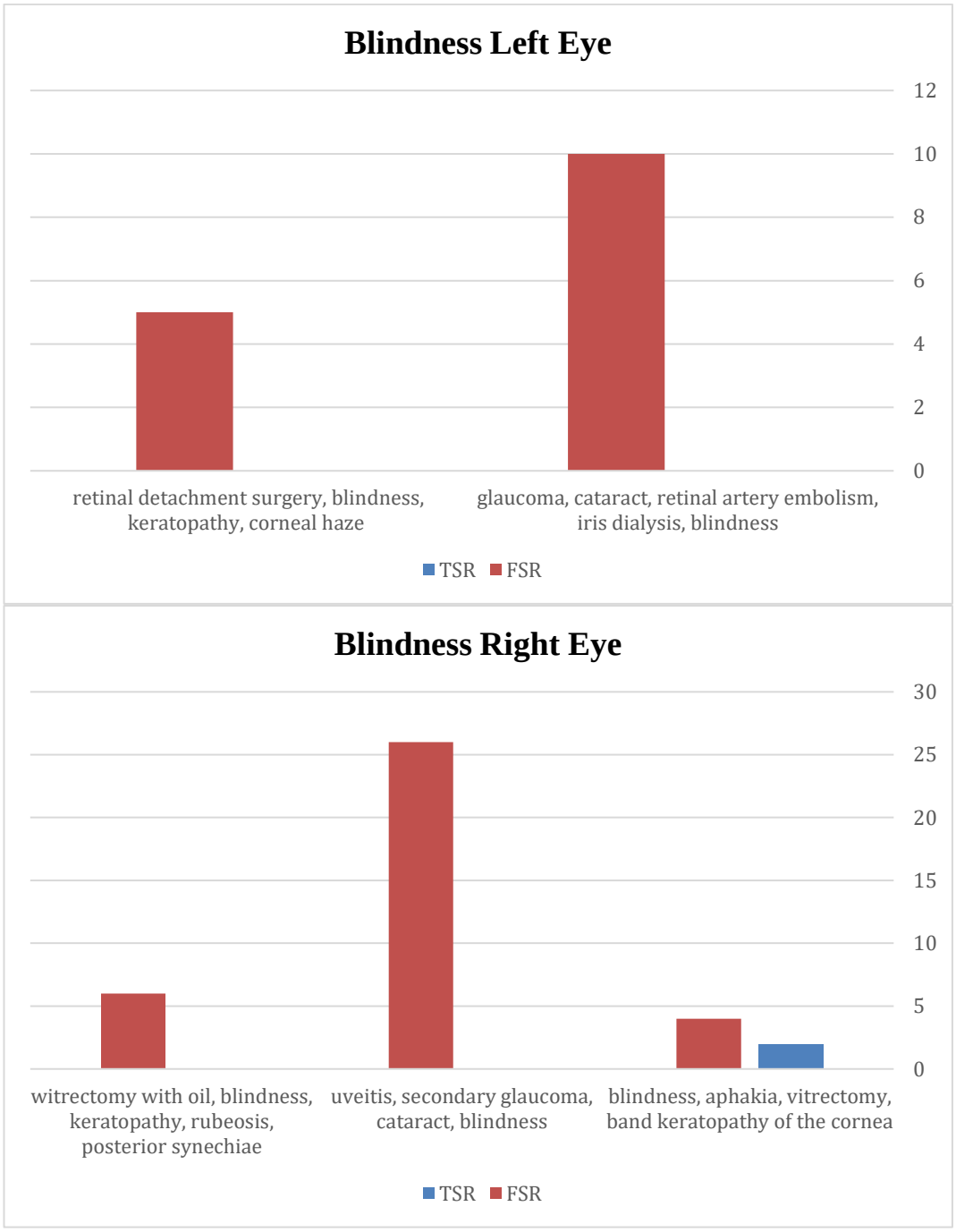

Figure 4.15. The segmentation results of Blindness.

In some eye trauma cases, the iris becomes unclear, so the segmentation process affects accordingly. Figure (4.16) lists the situation of eye diseases in which the eye trauma exists individually or with other diseases. The main reasons for segmentation errors in the case of Trauma are the blood in the eyes, the corneal haze, or other problems like retinal detachment and synechiae.

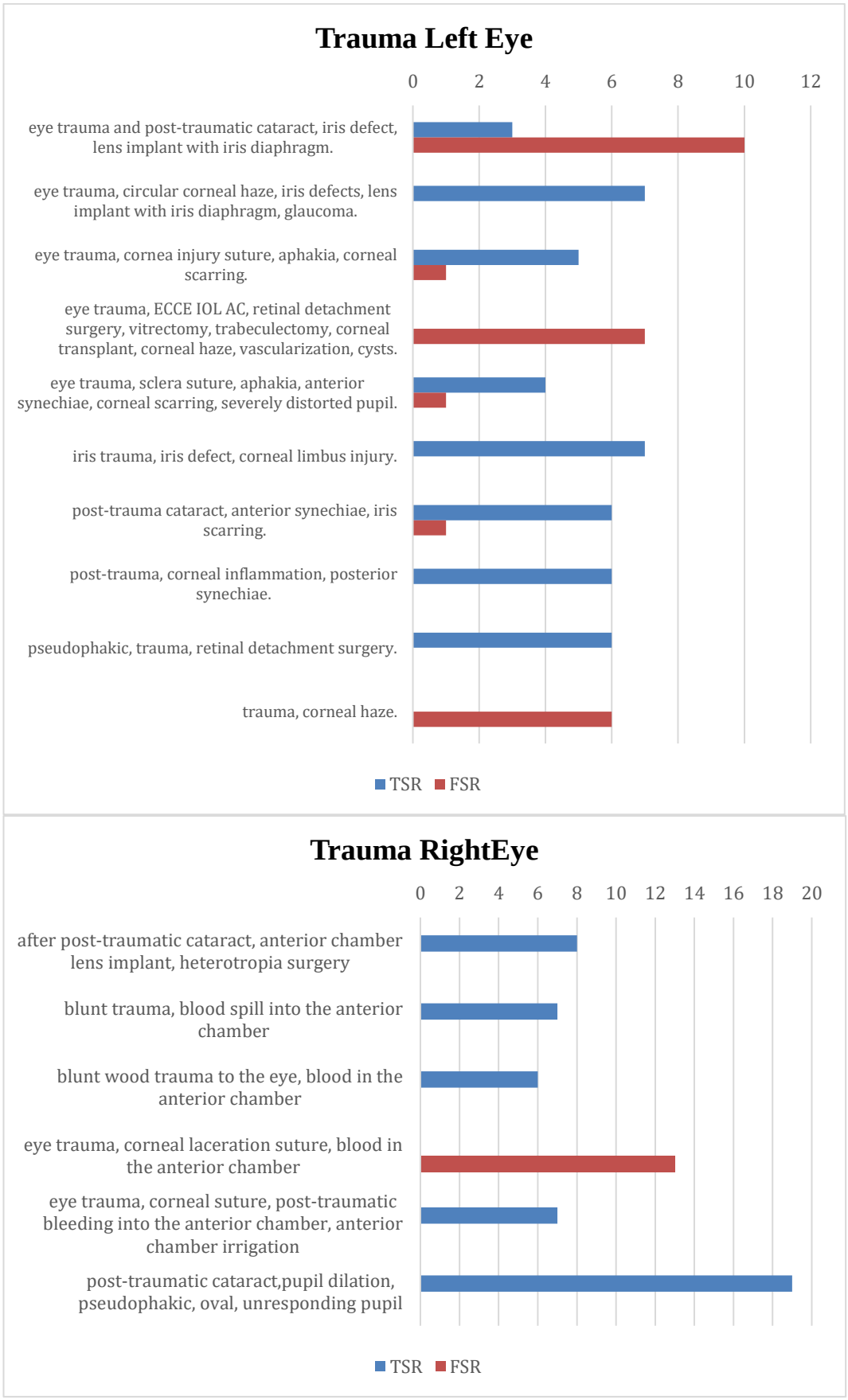

Figure 4.16. The segmentation results of Trauma cases.

The same conclusion of Cataract and Glaucoma in Warsaw V1 is also applied to the Warsaw V2. Figures (4.17) and (4.18) include the right and left eye's Cataract and Glaucoma disease statistics.

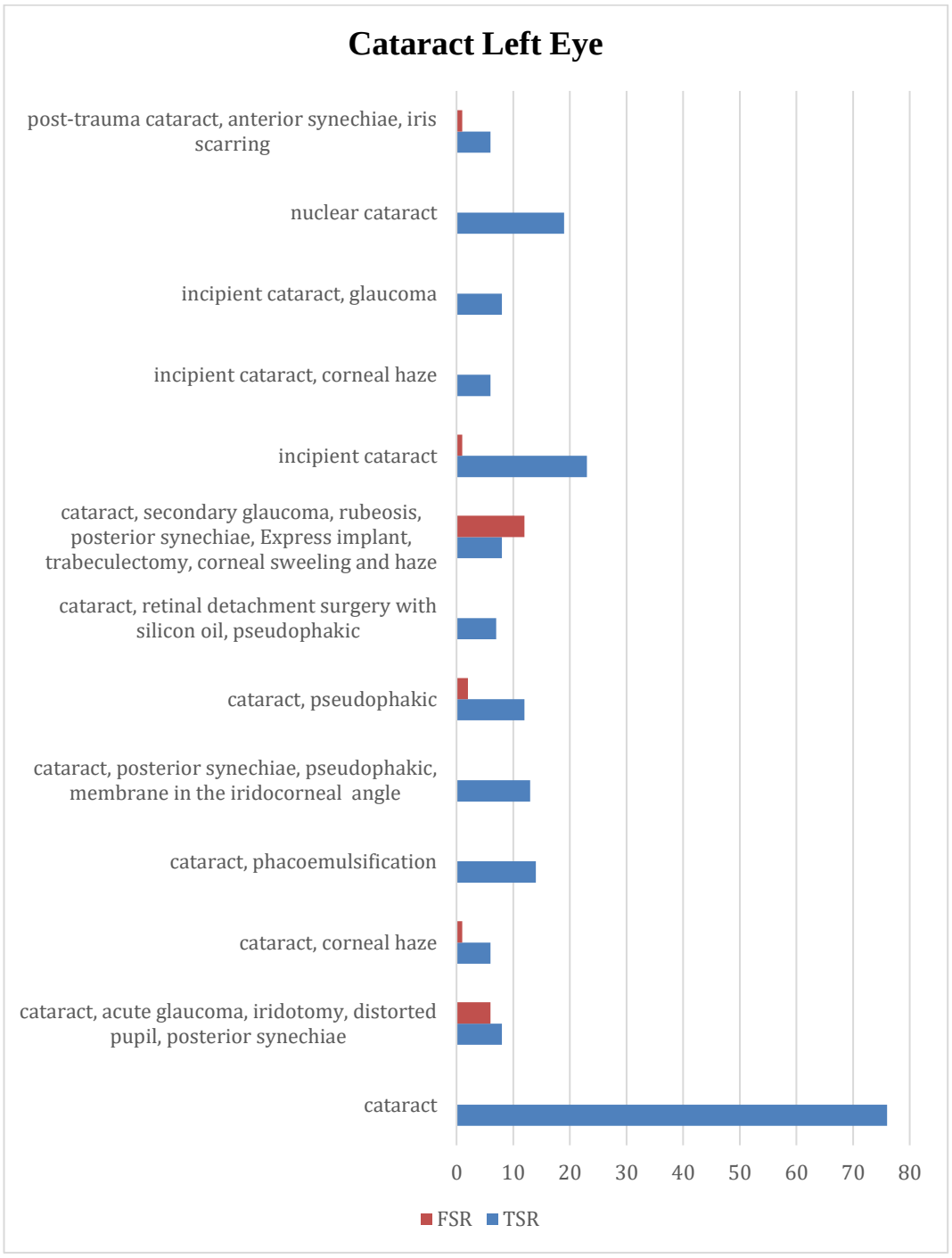

Figure 4.17. (A) The segmentation results of Cataract cases Left Eye.

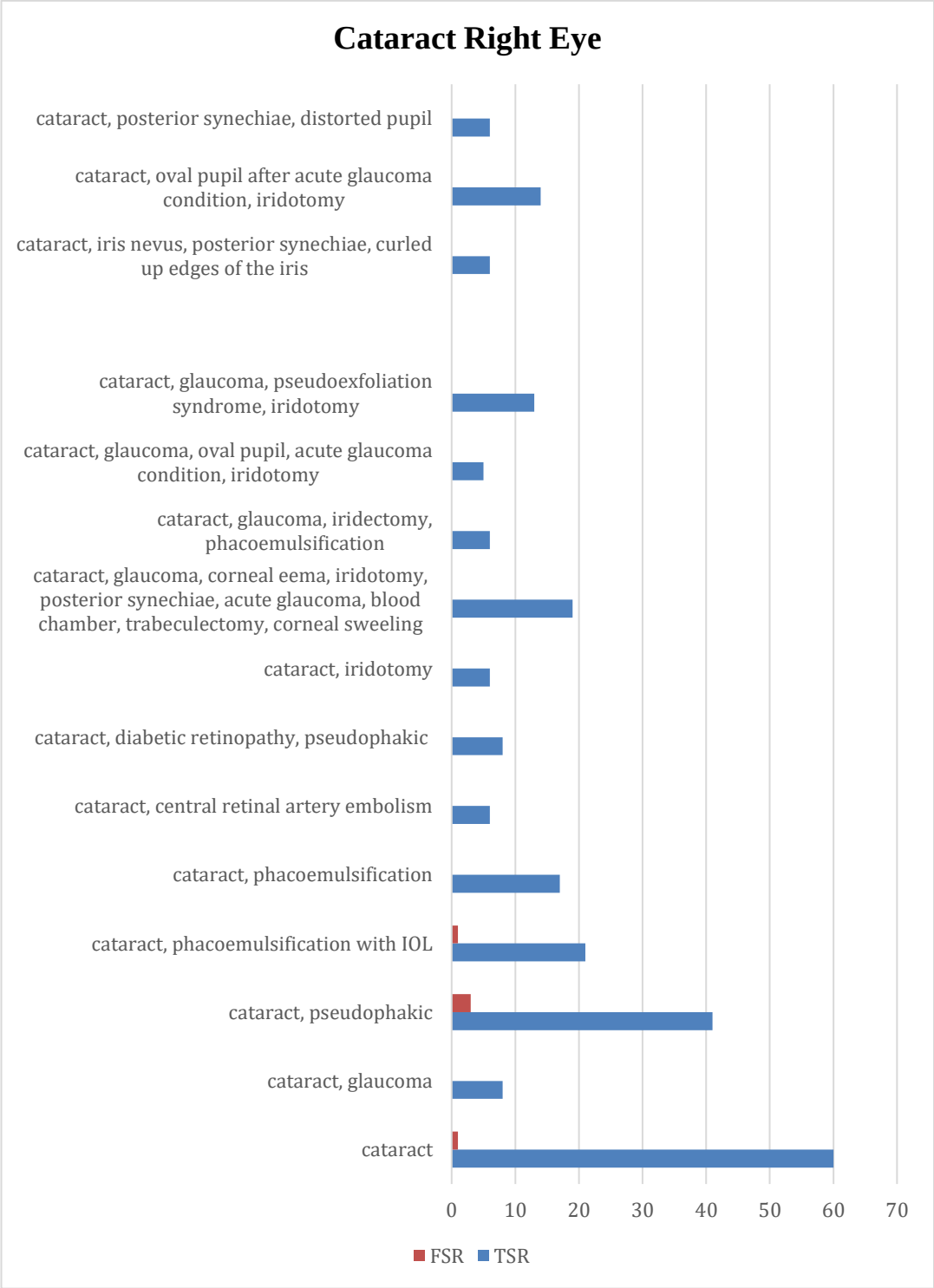

Figure 4.17. (B) The segmentation results of Cataract cases Right Eye.

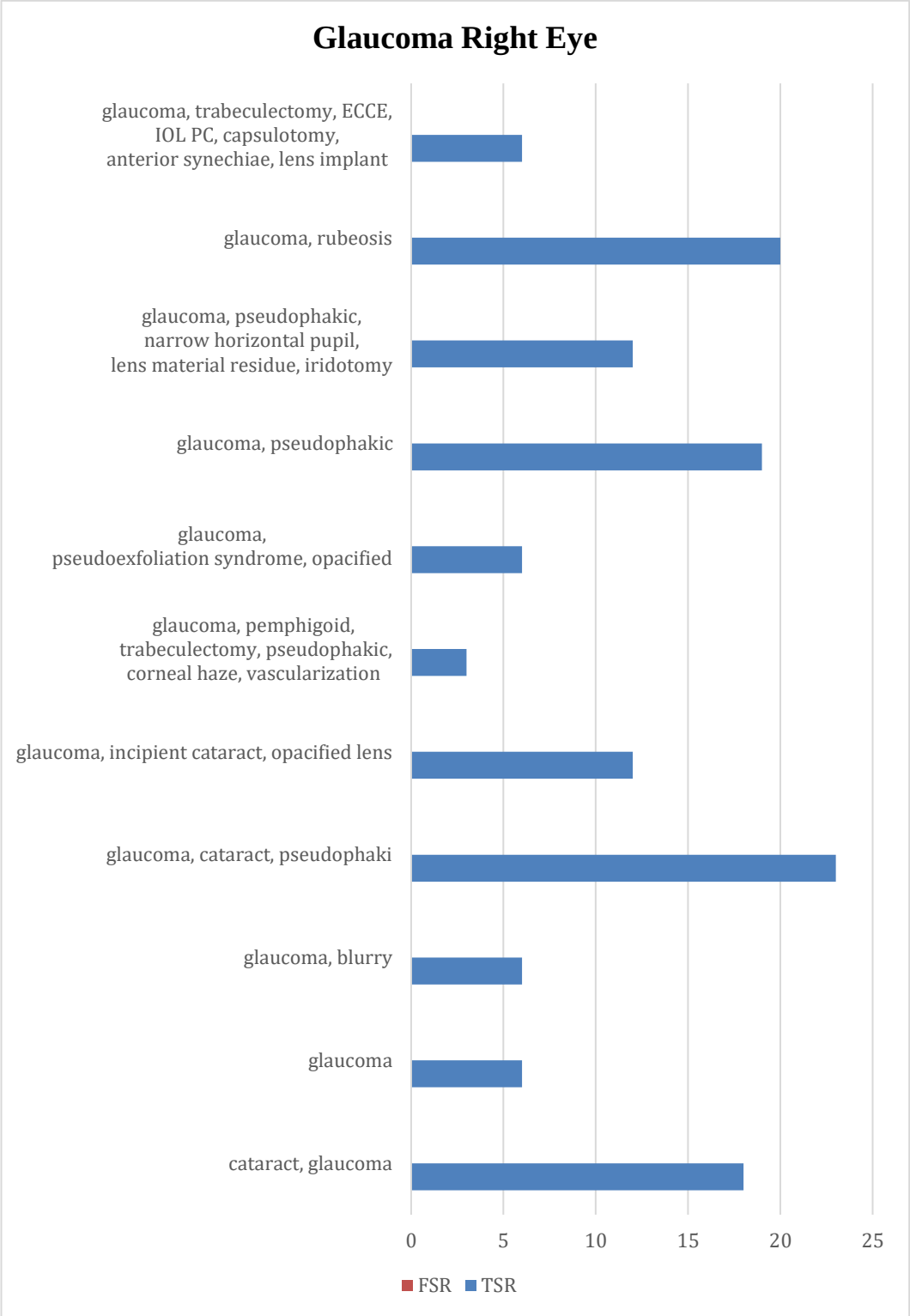

Figure 4.18. (A) The segmentation results of Glaucoma cases Right Eye.

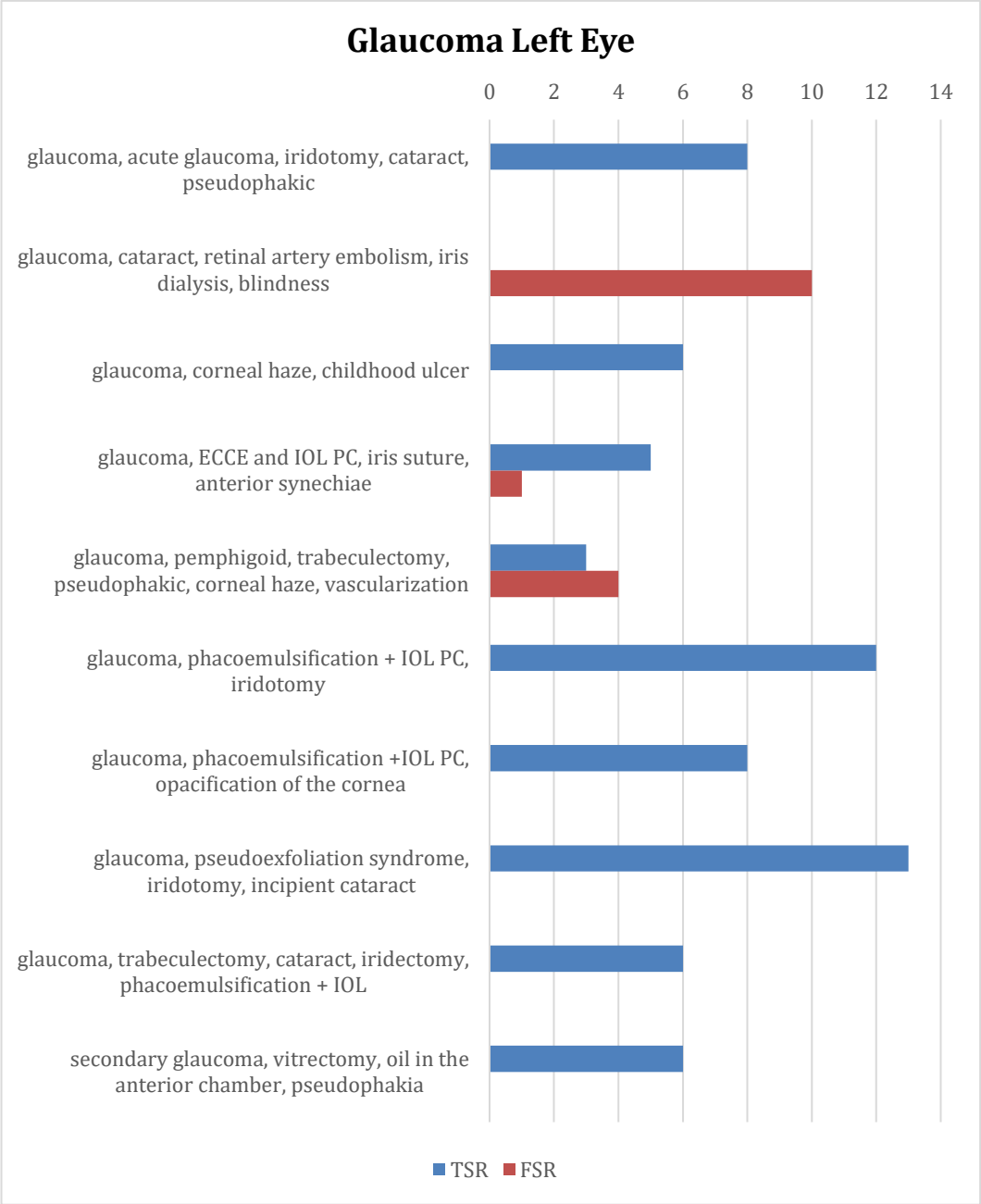

Figure 4.18. (B) The segmentation results of Glaucoma cases Left Eye.

Synechiae disease affects the segmentation results in case of mixed diseases (posterior synechiae, distorted pupil, corneal swelling and haze, retinal detachment, iridotomy, glaucoma, blindness, etc.), as figure (4.19) illustrates.

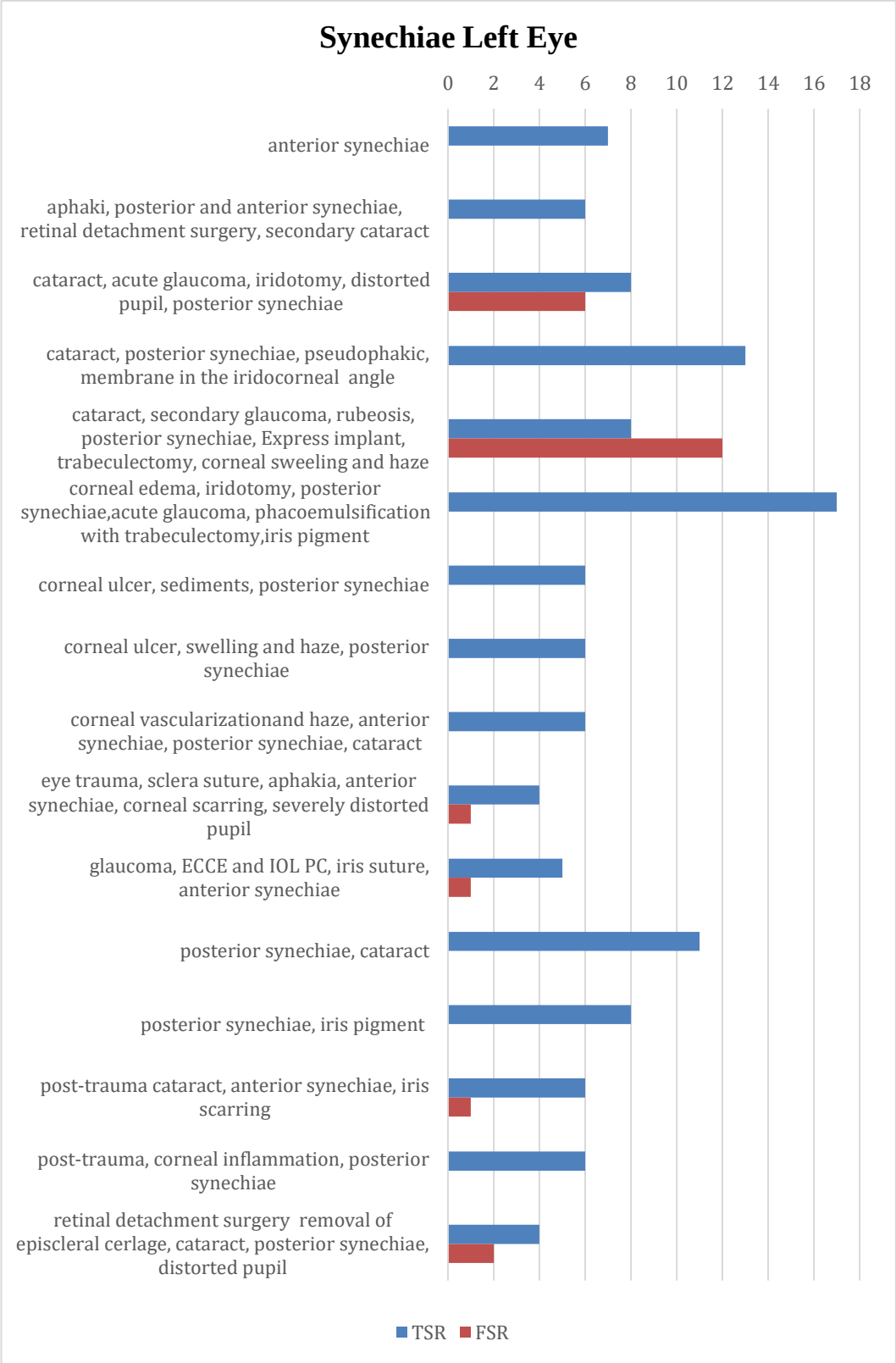

Figure 4.19. (A) The segmentation results of Synechiae cases Left Eye.

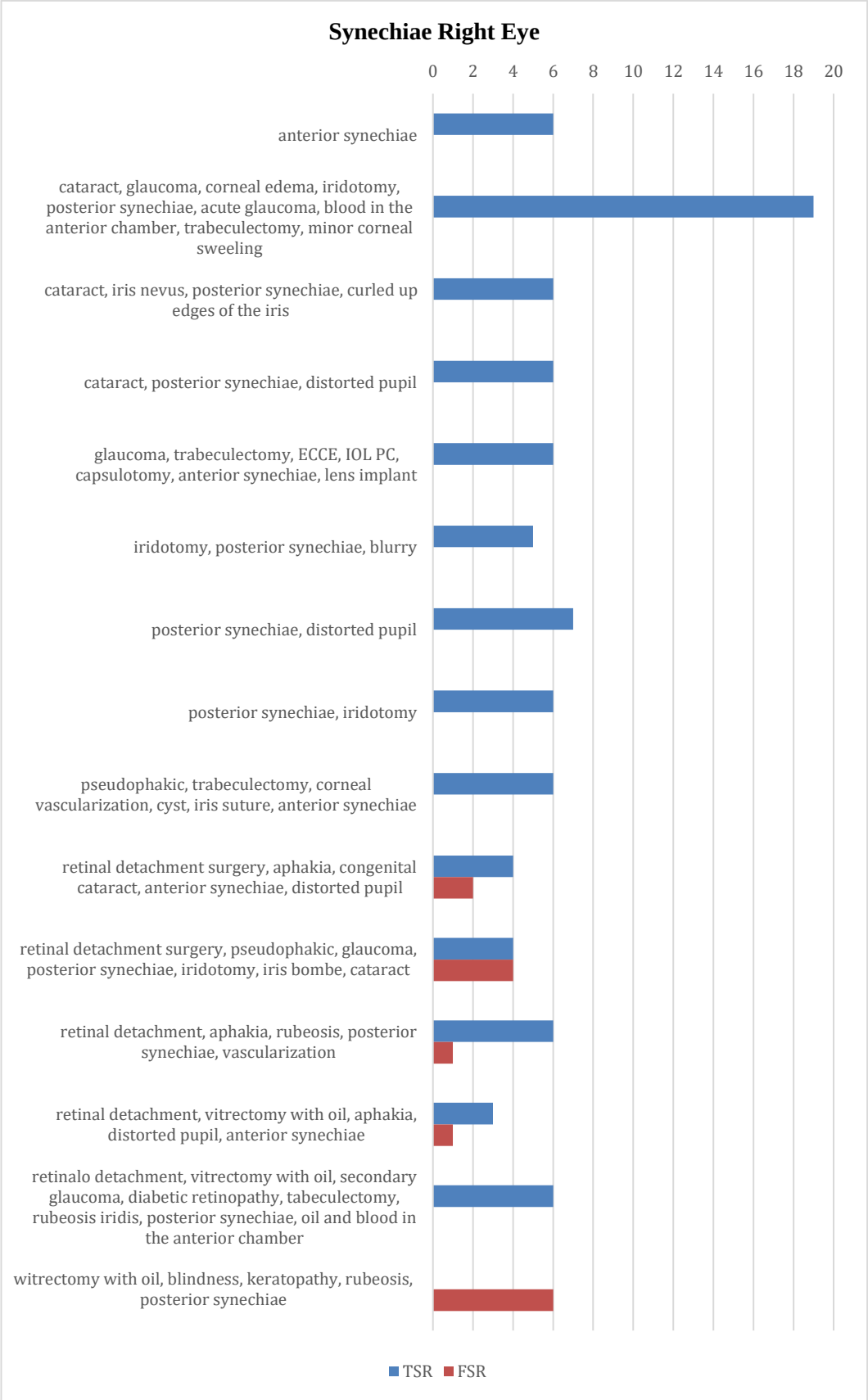

Figure 4.19. (B) The segmentation results of Synechiae cases Right Eye.

4.2.5. New Entry Diseases of Warsaw V2

1. **Lens Problems:**

The lens problem itself has no remarkable effect on the iris segmentation process. The segmentation errors in case of lens problems exist only because of other diseases (eye trauma, iris diaphragm, iris defect). Figure (4.20) confirms this conclusion.

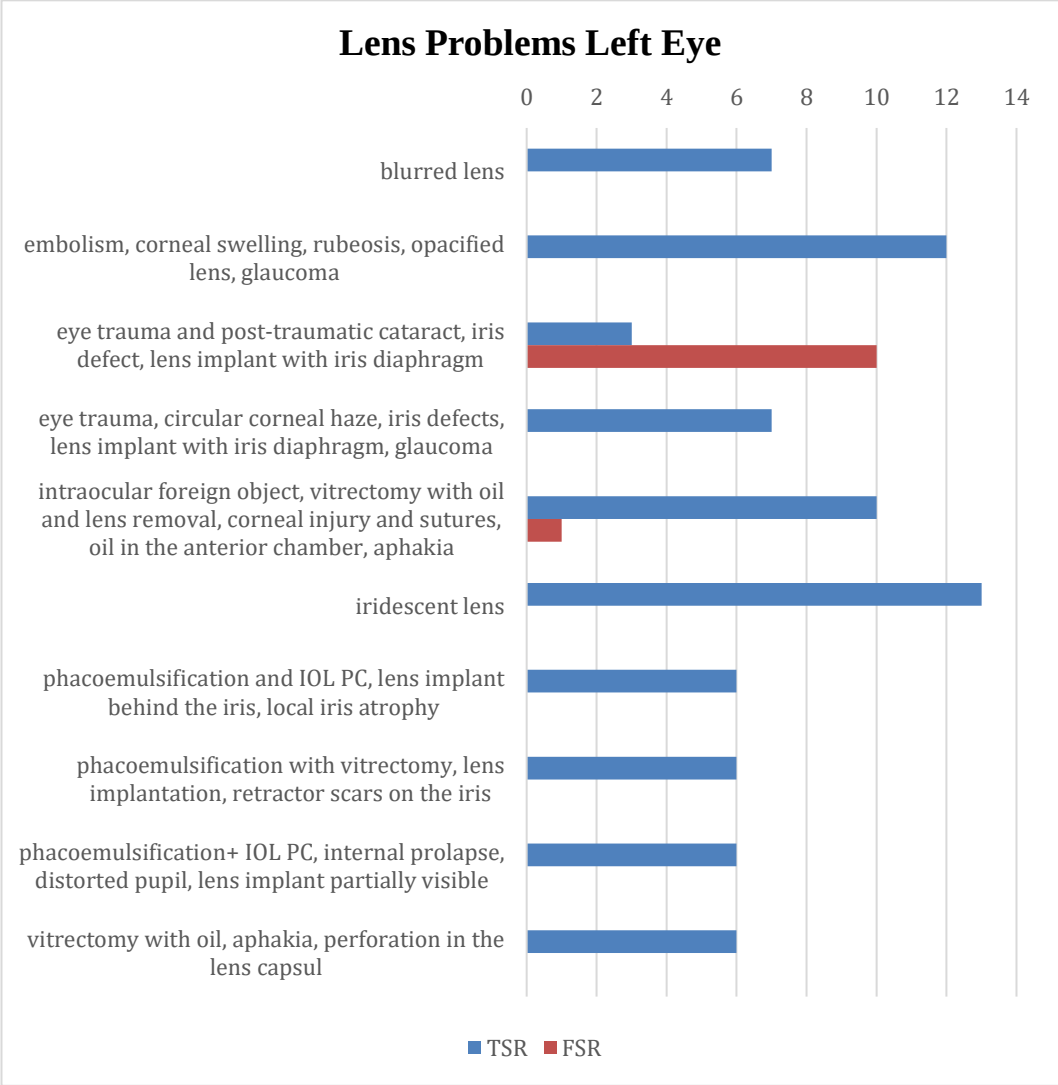

Figure 4.20. (A) The segmentation results of lens problems Left Eye.

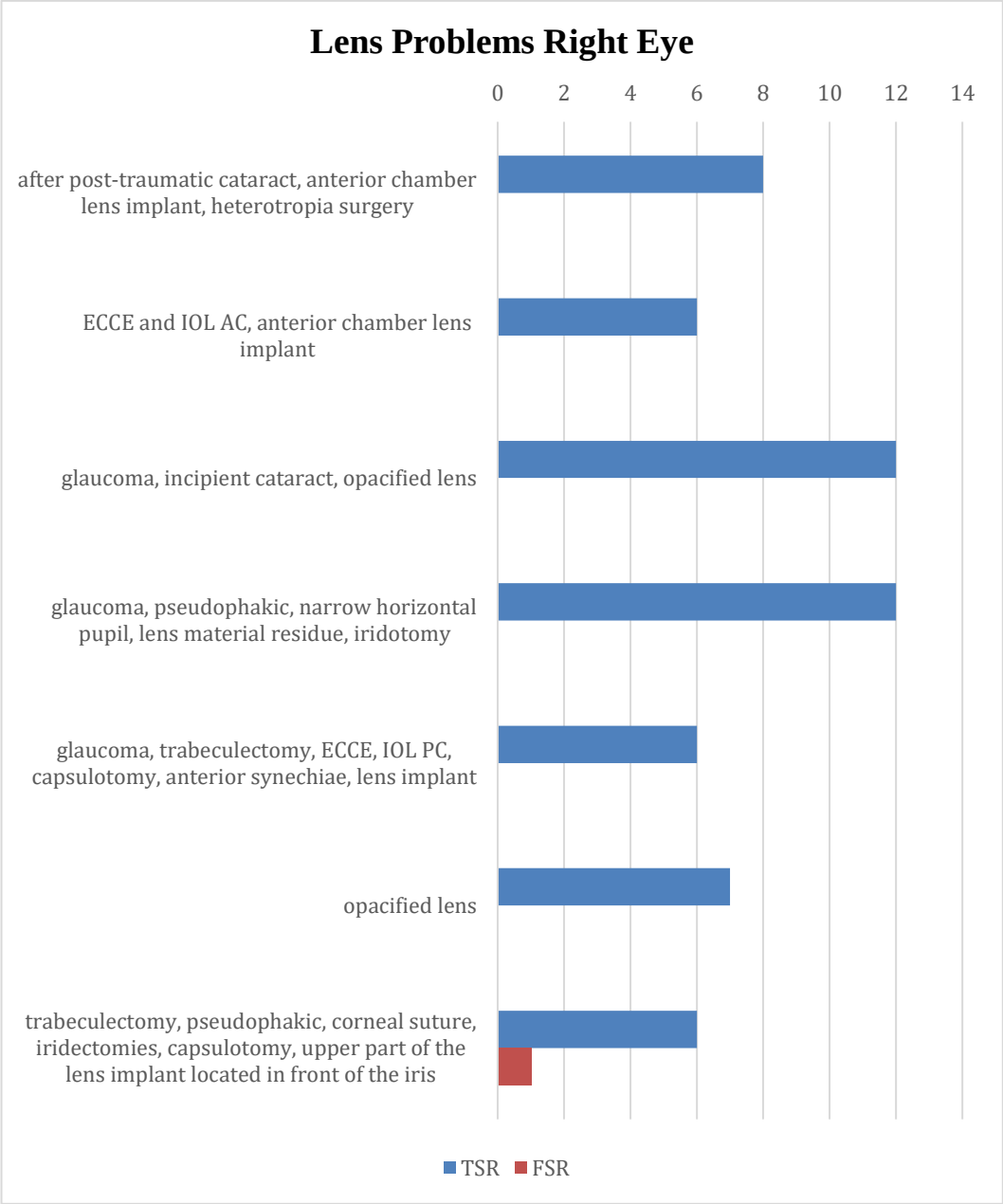

Figure 4.20. (B) The segmentation results of lens problems Right Eye.

2. Blurry Eyes:

The blurry problems have no effects on the segmentation process, as figure (4.21) shows.

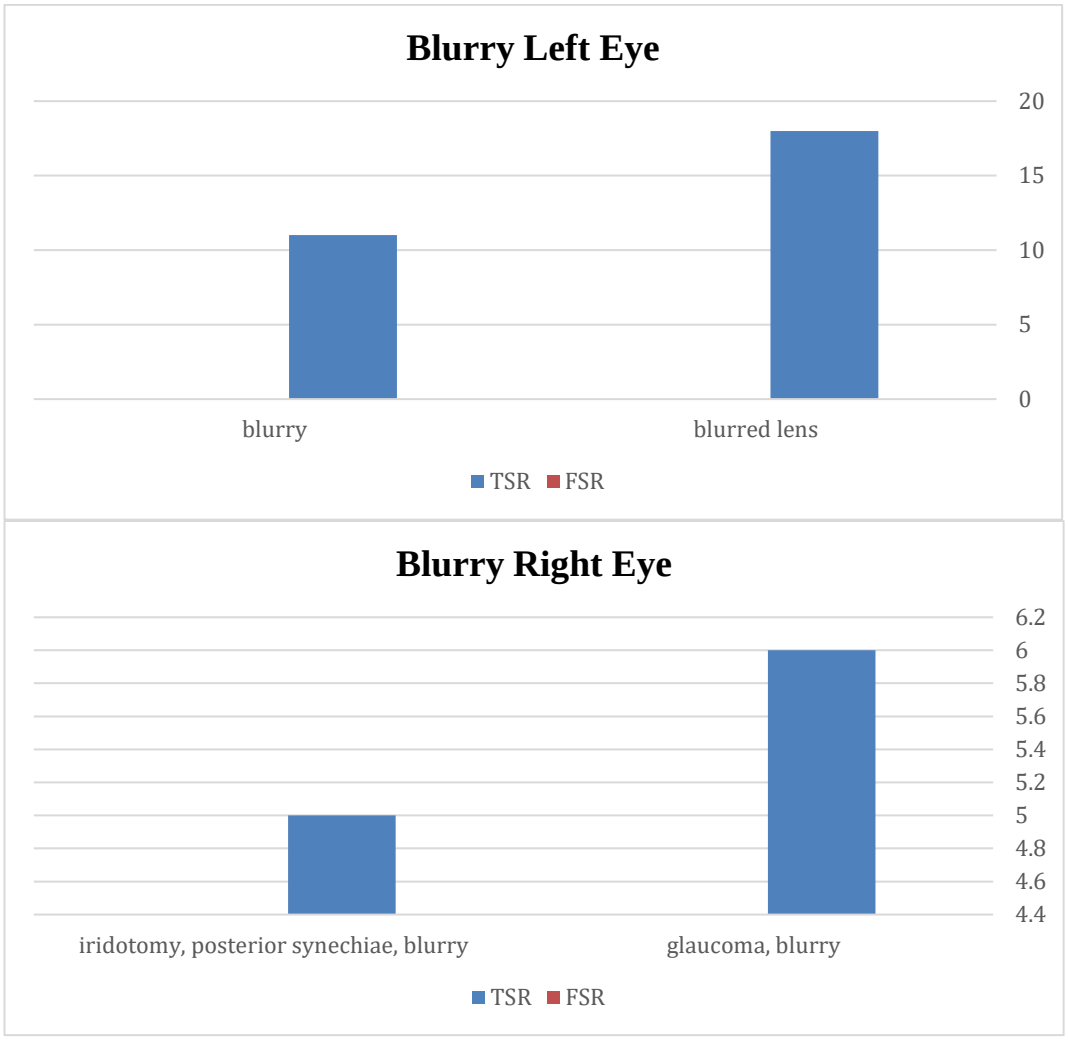

Figure 4.21. The segmentation results of blurry problems.

3. Aphakia:

Aphakia has some effects on the segmentation process but only in the presence of some other diseases, as figure (4.22) illustrates.

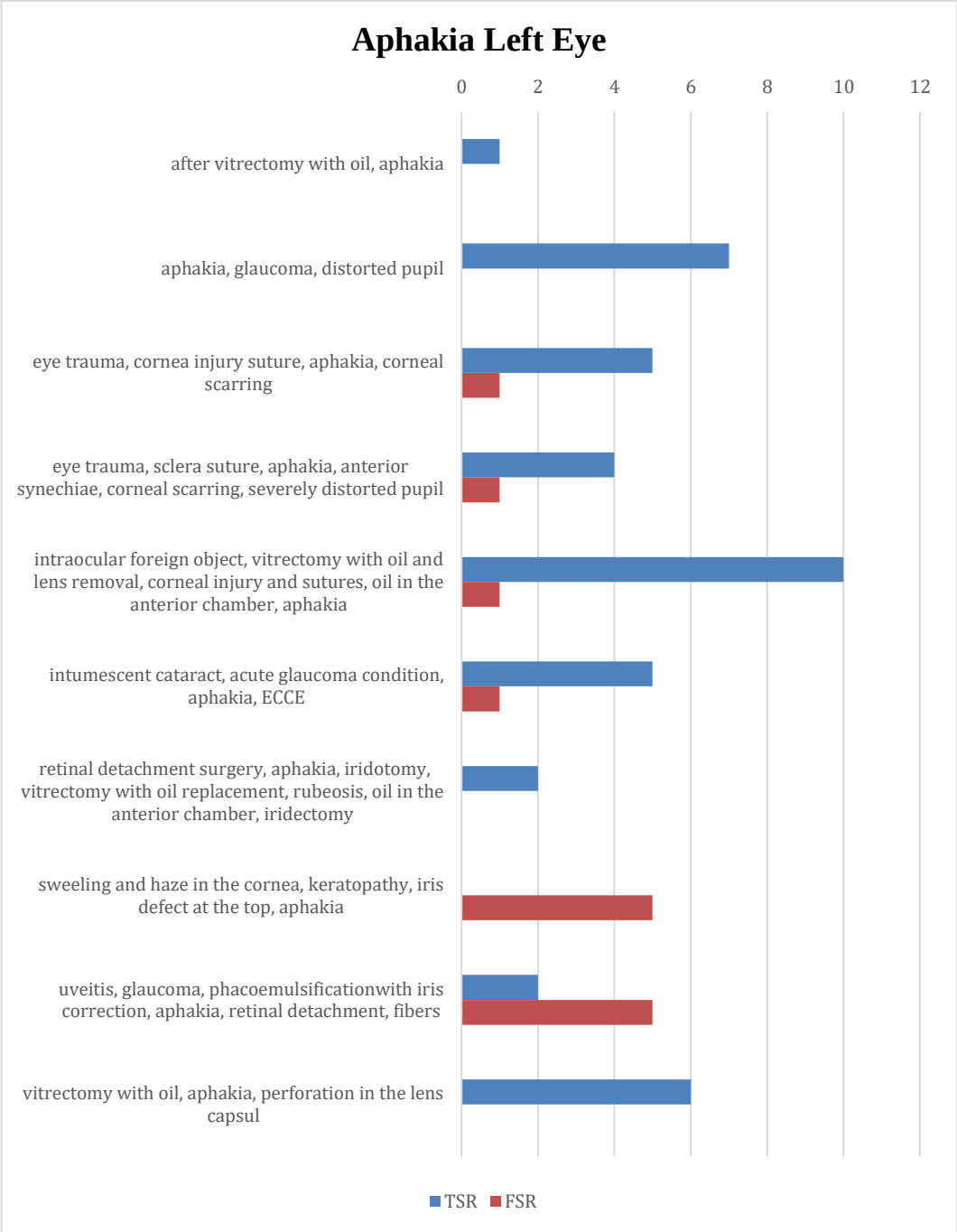

Figure 4.22. (A) The segmentation results of Aphakia problems Left Eye.

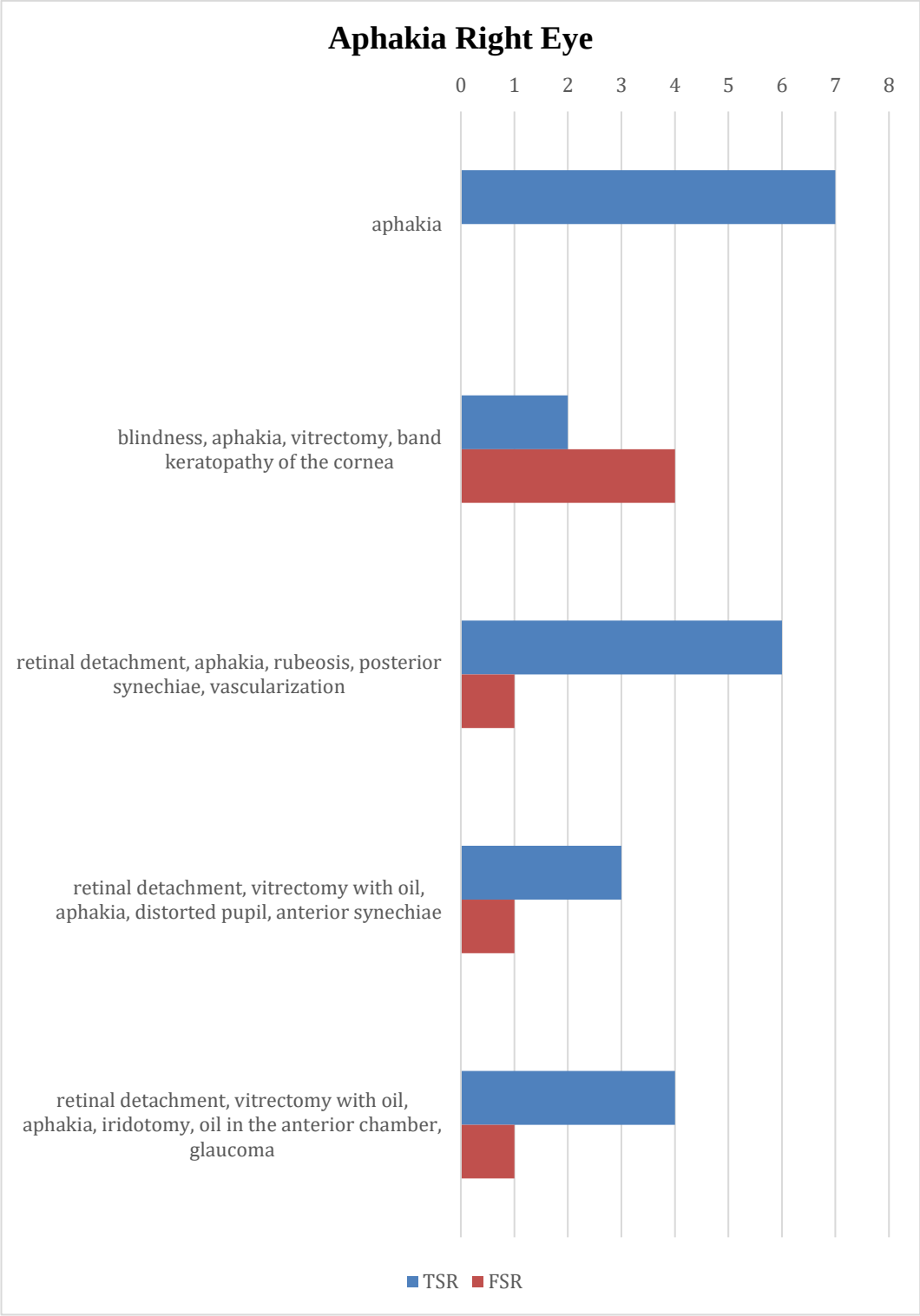

Figure 4.22. (B) The segmentation results of Aphakia problems Right Eye.

4.2.6 Ground Truth of The Iris Segmentation Results

Regarding the Warsaw Bio-Base V1 dataset, we segment 20 iris samples using the "Image Segmenter" of the MATLAB 2020 application designer. Figure (4.23) shows an example of image segmentation using this MATLAB app.

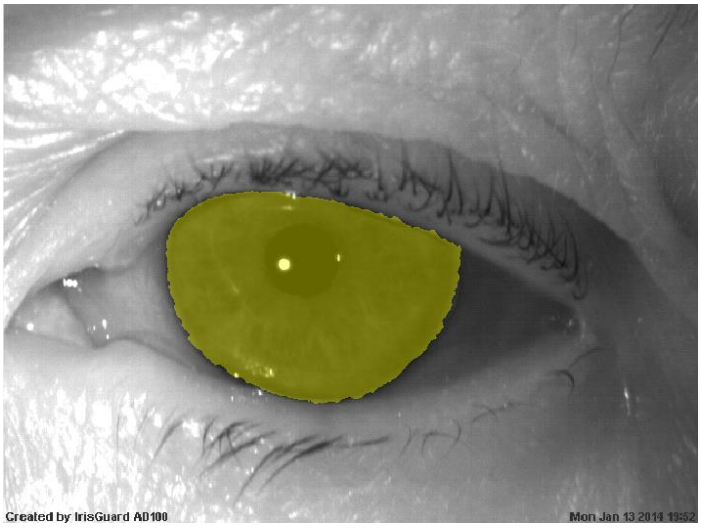

Figure 4.23. Manual segmentation Example of Warsaw V1.

The binary mask (ROI) is saved and used as the ground truth of this sample for each segmented image. For the next steps, the computed ground truth is compared to the actual segmentation results of the proposed iris segmentation methodology. To evaluate the segmentation results, the True Positives (TP), False Negatives (FN), True Negatives (TN), and False Positives (FP) of each iris test sample are computed. TP is the number of pixels that are correctly classified as iris pixels. FN is the number of incorrectly rejected pixels and considered non-iris pixels. On the other hand, TN is the number of pixels correctly classified as non-iris pixels, while FP is the number of pixels incorrectly classified as iris pixels. Figure (4.24) includes an example of an iris sample's TP, TN, FP, and FN after comparing the segmented iris ROI to its ground truth. Figure (4.25) shows the results of 20 randomly chosen samples of Warsaw Bio-Base V1 and their corresponding FN and FP.

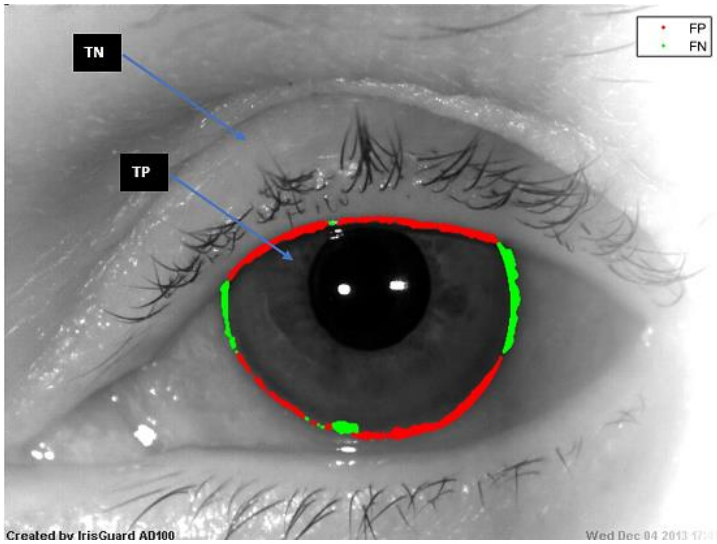

Figure 4.24. TP, TN, FP, and FN of an iris sample according to the ground truth.

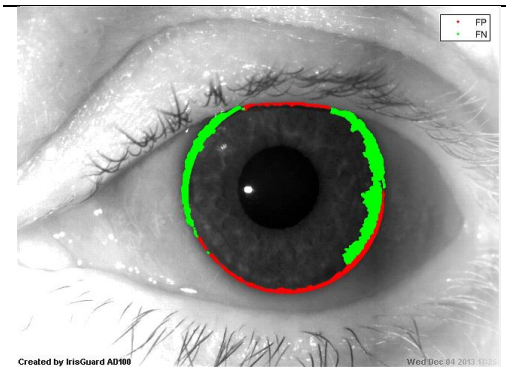

Img001L2

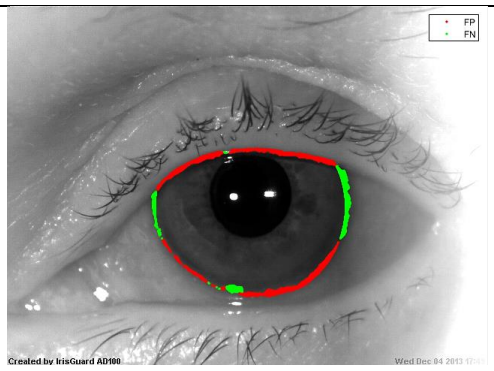

Img002L3

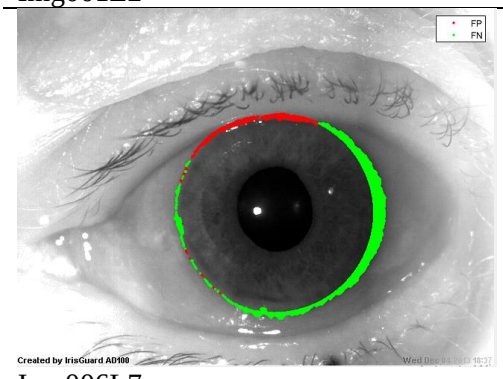

Img006L7

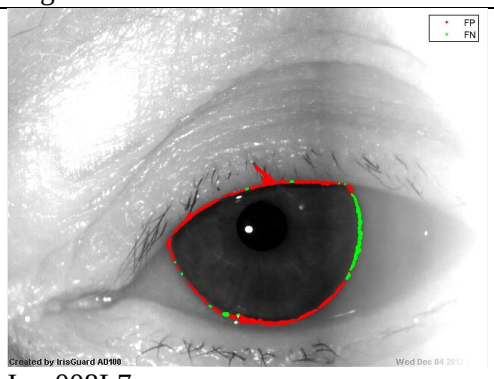

Img008L7

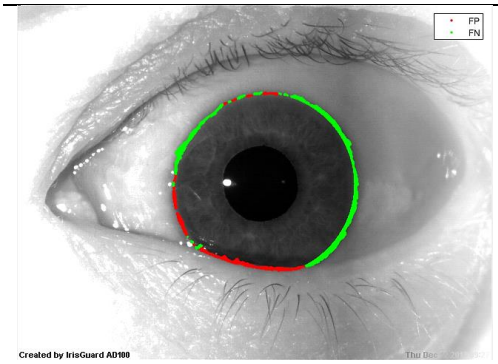

Img018L7

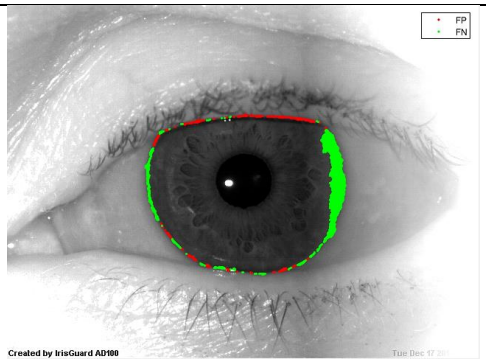

Img019L9

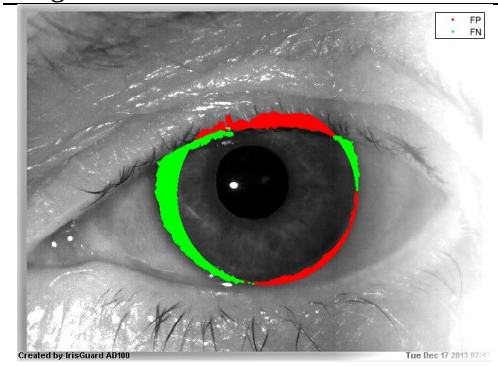

Img020L2

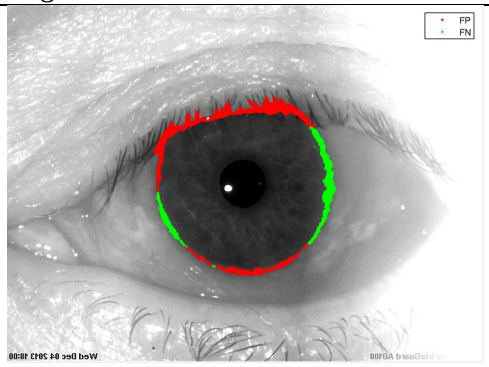

Img003R2

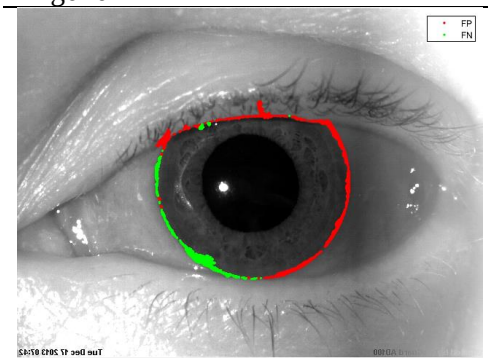

Img019R1

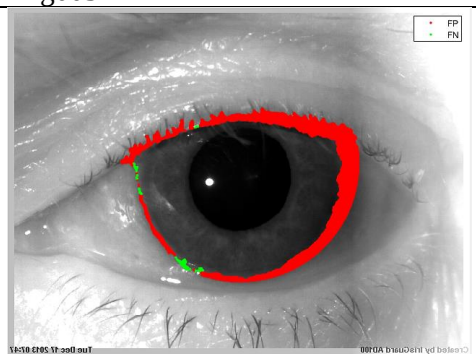

Img020R1

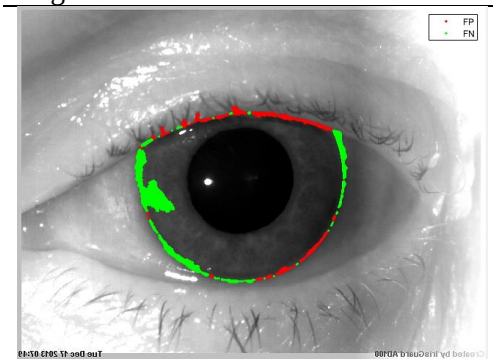

Img020R5

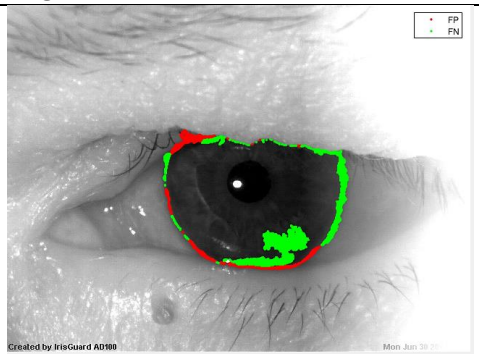

Img021L1

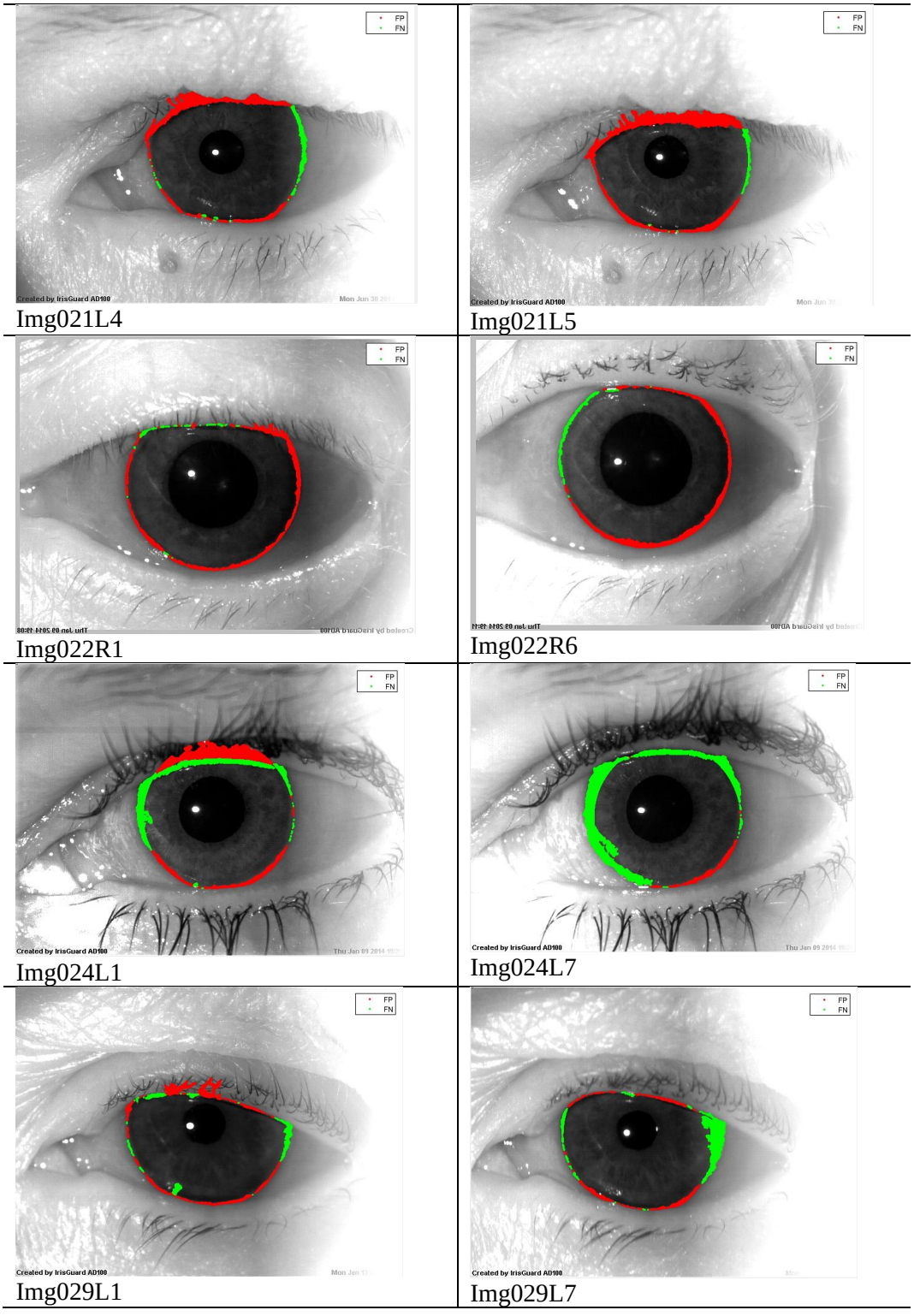

Figure 4.25. TP, TN, FP, and FN of a test sample of the iris dataset.

Table (4.1) includes the evaluation results of the 20 test samples of the Warsaw Bio-Base V1 dataset.

Table 4.1. TPR, FNR, TNR, FPR, and accuracy of some iris dataset samples.

File ID	TPR%	FNR%	TNR%	FPR%	ACC%
001L_2	88.775	11.225	99.492	0.50788	98.103
002L_3	97.283	2.7174	99.35	0.6495	99.148
003R_2	96.663	3.337	99.03	0.96967	98.734
006L_7	91.452	8.5484	99.707	0.29262	98.505
008L_7	99.107	0.89288	99.585	0.4154	99.533
018L_7	95.874	4.1257	99.776	0.22442	99.298
019L_9	94.37	5.6297	99.885	0.11481	99.155
019R_1	97.534	2.4662	99.452	0.54763	99.244
020L_2	86.554	13.446	98.829	1.1707	97.387
020R_1	99.629	0.37074	96.639	3.3606	97.036
020R_5	92.547	7.4533	99.689	0.31144	98.929
021L_1	88.801	11.199	99.627	0.37342	98.531
021L_4	98.241	1.7585	98.981	1.0193	98.89
021L_5	99.068	0.93231	98.287	1.7127	98.375
022R_1	99.601	0.3993	99.206	0.79367	99.254
022R_6	98.788	1.212	99.036	0.96361	99.004
024L_1	91.984	8.0156	98.522	1.4776	97.764
024L_7	82.03	17.97	99.792	0.20807	97.897
029L_1	97.662	2.3385	99.409	0.59133	99.212
029L_7	94.157	5.8428	99.71	0.28956	99.07
Average Values	94.506	5.494	99.2002	0.7997	98.6534

Table (4.1) proves that the segmentation accuracy of the proposed segmentation methodology is high, where the average segmentation accuracy is 98.6534% under a very low FPR of 0.799% and low FNR of 5.494%.

4.3. RECOGNITION RESULTS

To evaluate the effect of diseases on the performance of iris recognition systems, Warsaw Bio-Base Versions (V1 and V2) includes the most problematic and complex eye diseases image that affect both right and left eyes, utilized in the following scenarios. Additionally, the CASIA-IrisV3- Interval; Chinese Academy of Sciences holds healthy samples that also involve some scenarios. Classification to test the system's recognition accuracy based on the three types of pre-trained CNN models of transfer learning; GoogleNet, ResNet50, and ResNet101, are presented in all scenarios, the calculations of the confusion matrix, training, and validation of the models be used to evaluate the results. The augmentation option

has been configured in each scenario to augment training data. The implementation in this research is based on MATLAB R2020a.

It is essential to highlight that three splitting techniques have been utilized. For the first three scenarios sequentially, the splitting is 70 percent for training, 20 percent for validation, and 10 percent for testing. In scenario number 4, two other splitting techniques have been used to compare the most proper splitting method for the following scenarios.

4.3.1. Scenario No. (1) Utilizing Warsaw Bio-Base V1

Starting with Warsaw Bio-Base V1 as an input dataset for the first scenario. The entered data holds fifty-three classes; each includes segmented and original eye images of both left and right sides. The total numbers of samples are 1238 Grayscale images.

The results from Figures (4.26), (4.27), and (4.28) show the training and validation accuracy and loss for different models over a twenty-epoch period; The blue line stands for training accuracy. The red line illustrates the training loss, while the discrete black line represents validation in both cases of loss and accuracy. The accuracy in training or validation is measured by dividing the number of accurate predictions by the whole number of images.

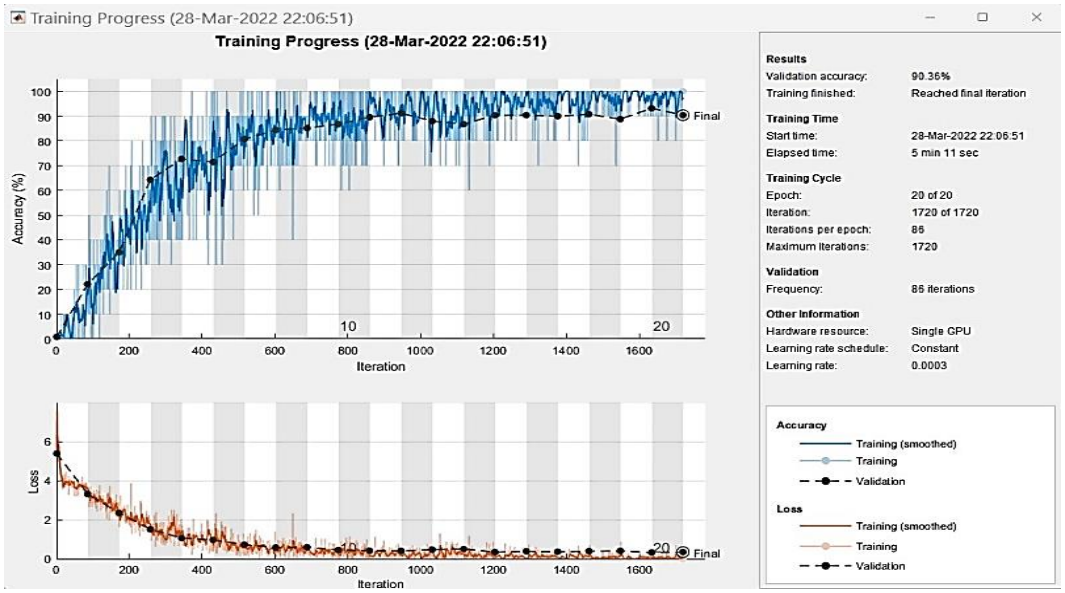

Figure 4.26. Warsaw Bio-Base training with GoogleNet model.

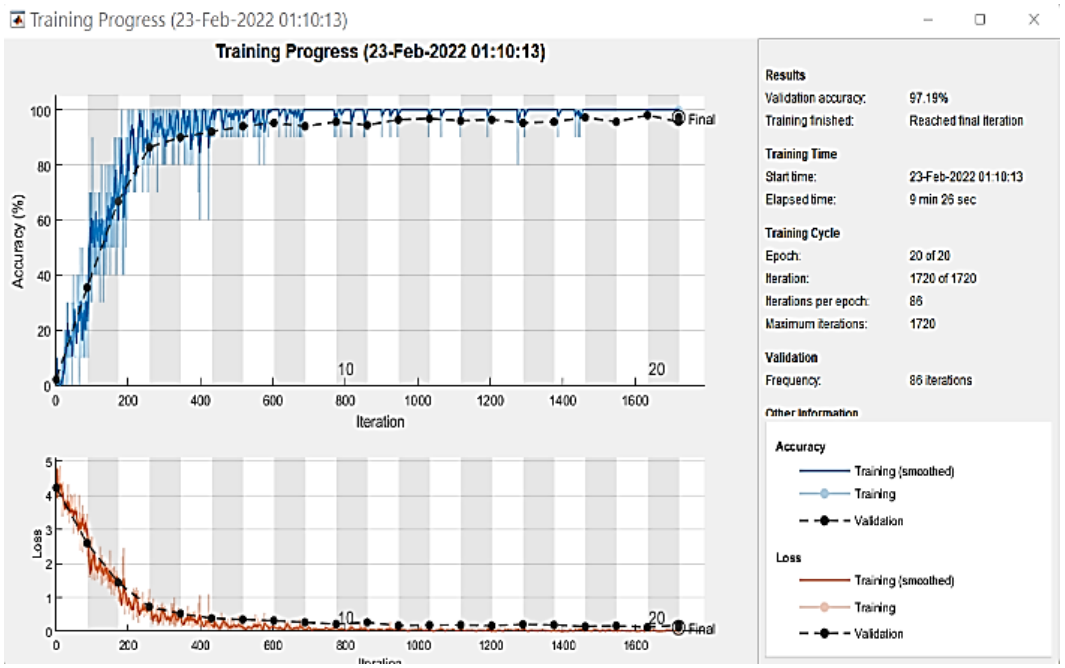

Figure 4.27. Warsaw Bio-Base training with ResNet50 model.

Overall, what stands out from the graphs, is that there were considerable upward trends for the training accuracy while the training loss saw a substantial fall over the period of training, which refers to a superior quality of training. However, the validation accuracy achieved 90.36% for GoogleNet compared with ResNet50,

97.19%, while ResNet101 closed with 96.38%. The validation prevents the models from overfitting and observes proper convergence; in Table (4.2), a comparison of the error rates according to the validation results for the given three models, the ResNet50 records the lowest error rate, for example, the false discovery rate (FDR) was 1.98% comparing with GoogleNet and ResNet101 which attained 7.46% and 2.46% respectively.

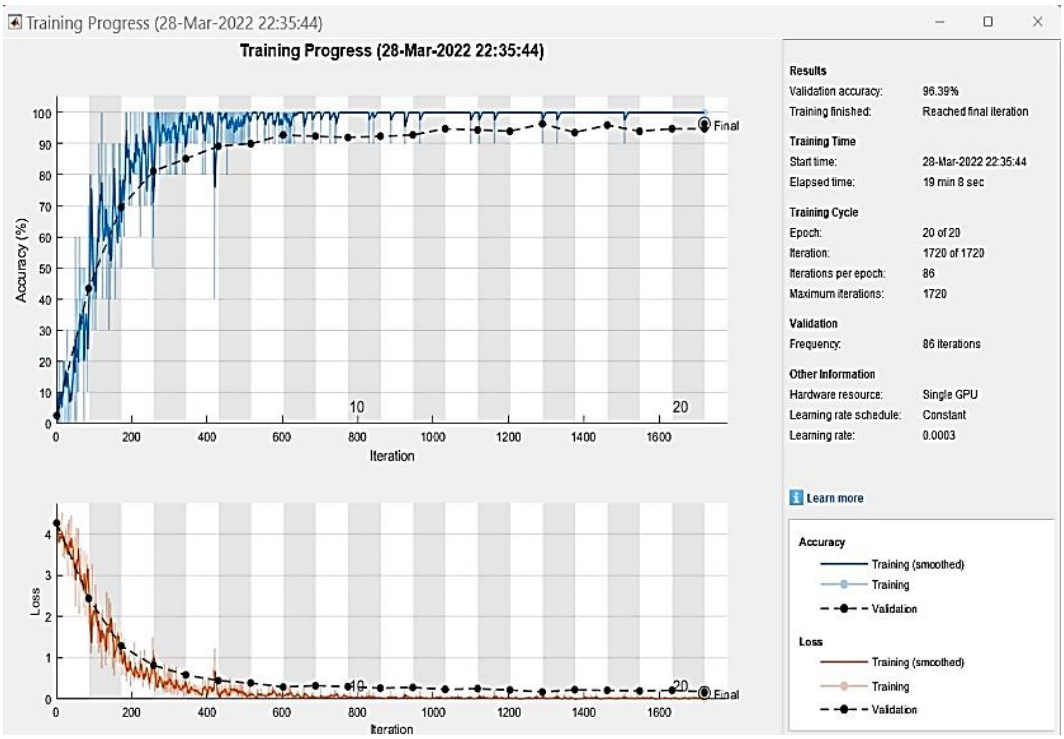

Figure 4.28. Warsaw Bio-Base training with ResNet101 model.

The GoogleNet network spent a reduced computational time, only 5 minutes 11 seconds. While the ResNet50 was 9.26 and the ResNet101 took the longest time, 19.8 compared with previous models.

The tests were 90.98, 94.26, and 95 percent for the recognition accuracy of GoogleNet, ResNet50, and ResNet101, respectively. Table (4.2) illustrates the model's test accuracys according to the calculations of the confusion matrix-based test sets. Including the true positive rate, positive predictive rate, false-negative rate, and false discovery rate, with each model's training computational time elapsed.

Table 4.2. Three models result for Warsaw Bio-Base V1.

Models	GoogleNet	Resnt-50	ResNet101
Test accuracy (%)	90.9836	94.2623	95.0820
Computational Time	5 min 11 sec.	9 min 26 sec	19 min. 8 sec.
Test TPR (%)	88.9937	93.0818	94.9686
Test PPR (%)	91.6026	95.9333	97.4679
Test FNR (%)	11.0063	6.9182	5.0314
Test FDR (%)	8.3974	4.0667	2.5321
Validation Accuracy (%)	90.3614	97.1888	96.3855
Validation TPR (%)	88.8604	96.6667	94.9161
Validation PPR (%)	92.5385	98.0121	97.5008
Validation FNR (%)	11.1396	3.3333	5.0839
Validation FDR (%)	7.4615	1.9879	2.4992
Training Accuracy (%)	100.00	100.00	100.00

To conclude the scenario, the model's recognition performance increased and achieved a test result of 95.36% for ResNet101, while the amount of computational time increased approximately double compared with the previous models (ResNet50 and GoogleNet). The GoogleNet spent the lower computational time but the highest error rates. The ResNet50 achieved the highest validation accuracy and balance-off computational time with high test accuracy.

4.3.2. Scenario No. (2) Warsaw Bio-Base V2 Results

Warsaw V2 dataset is an extension of V1, including more eye diseases. The same scenario (Scenario No.1) applied for the Warsaw dataset version two, the scenario holding 3128 grayscale samples. As shown in the comparison Table (4.3), the GoogleNet achieved only 88.78% of test accuracy with a computational time of 13 minutes and 3 seconds, while ResNet50 provided 94.39% with 25 minutes and 40 seconds compared with the ResNet101 peaks 96.37% with 51 minutes and 58 seconds, as well as the FDR and FNR, was the lowest in ResNet101 comparing with other models.

Table 4.3. Three models result for Warsaw Bio-Base V2.

Models	GoogleNet	Resnt-50	ResNet101
Test accuracy (%)	88.7789	94.3894	96.3696
Computational Time	13 min. 3 sec.	25 min. 40 sec.	51 min. 58 sec.
Test TPR (%)	86.0767	92.5411	93.9528
Test PPR (%)	89.9913	96.2095	96.8654
Test FNR (%)	13.9233	7.4589	6.0472
Test FDR (%)	10.0087	3.7905	3.1346
Validation Accuracy (%)	90.5213	96.3665	96.5245
Validation TPR (%)	89.7515	96.1894	94.8230
Validation PPR (%)	92.3009	97.1506	96.7920
Validation FNR (%)	10.2485	3.8106	5.1770
Validation FDR (%)	7.6991	2.8494	3.2080
Training Accuracy (%)	100.00	100.00	100.00

The scenario proves that the ResNet models achieved a higher test accuracy than the GoogleNet, while computational time increased approximately double in each other models.

4.3.3. Scenario No. (3) Warsaw plus CASIA Results

To evaluate the model's ability in the case of fusion diseases and healthy datasets, the Warsaw Version 2 and CASIA datasets of grayscale images contain the original eye samples with the segmented iris images comprising 10889 total samples inside 360 distributed unequally as the original datasets' classes have been used. The experiment was repeated with the same scenario after separating the number of classes equally between Warsaw and CASIA, where the total number of samples was 6935 in 228 classes (table (4.4)).

Table 4.4. Fusion Scenario Warsaw Plus CASIA grayscale images.

Models	GoogleNet	Resnt-50	ResNet101
Test accuracy (%)	95.6190	98.3810	98.6667
Computational Time	42 min. 20 sec.	81 min. 22 sec.	177 min. 5 sec.
Test TPR (%)	93.9551	98.0349	98.5560
Test PPR (%)	96.7498	98.3805	99.0628
Test FNR (%)	6.0449	1.9651	1.4440
Test FDR (%)	3.2502	1.6195	0.9372
Validation Accuracy (%)	96.0325	98.1966	98.1515

Models	GoogleNet	Resnt-50	ResNet101
Validation TPR (%)	94.3207	96.9264	97.8585
Validation PPR (%)	96.3665	98.3767	98.4948
Validation FNR (%)	5.6793	3.0736	2.1415
Validation FDR (%)	3.6335	1.6233	1.5052
Training Accuracy (%)	100.00	100.00	100.00

Many points have been concluded; fault samples for Warsaw and CASIA fused datasets result in only a few test errors, especially with the ResNet101 model, which hit the zero for the FDR and 1.44 for the FNR. The combination of healthy and disease sets increased the overall test accuracy for all three models. The number of samples increased; thus, the training process elapsed longer. In contrast, ResNet50 consumed the average computational time among the models and achieved a 98.38% recognition accuracy rate.

Reducing the number of healthy classes will increase the error rates of both FDR and FNR; however, the test accuracy decreased by only one percent for ResNet models. Table (4.5).

Table 4.5. Warsaw – CASIA datasets equally distributed classes.

Models	GoogleNet	Resnt-50	ResNet101
Test accuracy (%)	92.3653	97	97.4551
Computational Time	27 min. 10 sec.	52 min. 41 sec.	114 min. 41 sec.
Test TPR (%)	90.8402	95.2063	96.9439
Test PPR (%)	92.9265	97.3853	98.3859
Test FNR (%)	9.1598	4.7937	3.0561
Test FDR (%)	7.0735	2.6147	1.6141
Validation Accuracy (%)	94.4091	98.4430	98.0184
Validation TPR (%)	92.3420	98.2511	97.0832
Validation PPR (%)	94.9245	98.5834	97.7044
Validation FNR (%)	7.6580	1.7489	2.9168
Validation FDR (%)	5.0755	1.4166	2.2956
Validation Models	GoogleNet	Resnt-50	ResNet101
Training Accuracy (%)	100.00%	100.00%	100.00%

4.3.4. Scenario No. (4) Splitting Scenario

Three different splitting scenarios are used; the first uses 70% of data for training, 20% for validation, and 10% for test sets, while the second splitting utilizes the same training split but with 15% for validation and the same for test sets. The last splitting method is making the training set 60% of the data, while the validation takes 20%, and the rest will remain for test sets. Tables (4.6), (4.7), and (4.8) compare these scenarios using the GoogleNet, ResNet50, and ResNet101 deep learning networks.

To study the response of each model with different splitting techniques and evaluate how far the model accuracy changes in different splitting scenarios to distinguish the most proper splitting set. The tables below show the comparison results for each model in different splitting cases, utilizing both Warsaw V2 and CASIA datasets.

The GoogleNet accuracy responds differently based on splitting techniques. Still, deep learning networks perform well in many cases of eye diseases. However, splitting 70%, 20%, and 10% of data was the best choice compared to the testing accuracy and the calculation percentage of the error rates for each model scenario.

Table 4.6. Three GoogleNet different splitting scenarios results.

Splitting Rates	**70% 15% 15%**	**60% 20% 20%**	**70% 20% 10%**
Test accuracy (%)	92.3410	93.2439	95.6190
Computational Time	44 min. 47 sec.	36.min. 22 sec.	42 min. 20 sec.
TPR (%)	91.2676	91.3165	93.9551
PPR (%)	93.5633	94.2472	96.7498
FNR (%)	8.7324	8.6835	6.0449
FDR (%)	6.4367	5.7528	3.2502

Table 4.7. Three ResNet50 different splitting scenarios results.

Splitting Rates	70% 15% 15%	60% 20% 20%	70% 20% 10%
Test accuracy (%)	98.8264	97.5474	98.3810
Computational Time	85 min. 29 sec.	70 min. 34 sec.	81 min. 22 sec.
TPR (%)	98.5010	96.3948	98.0349
PPR (%)	99.0732	97.8962	98.3805
FNR (%)	1.4990	3.6052	1.9651
FDR (%)	0.9268	2.1038	1.6195

Table 4.8. Three ResNet101 different splitting scenarios results.

Splitting Rates	70% 15% 15%	60% 20% 20%	70% 20% 10%
Test accuracy (%)	98.4558	97.5012	98.6667
Computational Time	175 min. 40 sec.	157 min. 3 sec.	177 min. 5 sec.
TPR (%)	97.8282	96.4872	98.5560
PPR (%)	98.5171	97.8480	99.0628
FNR (%)	2.1718	3.5128	1.4440
FDR (%)	1.4829	2.1520	0.9372

For the following scenario, we will study the effect of the colored images of the diseases Warsaw datasets and how far they will change the results.

4.3.5. Scenario No. (5) The Colored Samples Scenario

Further specific criteria have been used in this scenario to compare the model's performance under colored (RBG) and non-colored photos (Grayscale Images); thus, Warsaw V1 was applied first, followed by Warsaw V2, and then the combined datasets (CASIA and Warsaw) utilized.

4.3.5.1. Warsaw Bio-Base V1 with Colored Samples

In this scenario, the Warsaw V1 Grayscale samples were utilized plus 112 colored images, while the total number of samples was 1350.

The calculations in Table (4.9) prove that the GoogleNet model slightly decreased the False Discovery Rate (FDR) and False Negative Rate (FNR) compared with the non-colored scenario. In contrast, small increases in the error rate with the model ResNet101, where the ResNet50 showed robustness against the changes, decreased

the FNR, and achieved approximately the same test accuracy in both scenarios. The colored scenario increased the training time in all models.

Table 4.9. Warsaw Bio-Base "With Colored Samples" V1 Scenario Results.

Models	GoogleNet	ResNet50	ResNet101
Test accuracy (%)	91.0448	94.7761	93.2836
Computational Time	7 min. 44 sec.	12 min. 31 sec.	22 min. 27 sec.
TPR (%)	90.0943	94.3396	93.2390
PPR (%)	93.2353	95.8940	96.0256
FNR (%)	9.9057	5.6604	6.7610
FDR (%)	6.7647	4.1060	3.9744

4.3.5.2. Warsaw Bio-Base V2 with colored samples

In this scenario, the dataset of Warsaw V2 Grayscale contains 616 additional colored images, while the total number of samples was 3744 images.

The FNR and FDR slightly increased with ResNet101 compared with the ResNet50, which again showed decreasing false-negative rate and a slight increase in test accuracy compared with the non-colored samples scenario. The ResNet50 shows a better performance than both GoogleNet and ResNet101. as Table (4.10) illustrates.

Table 4.10. Warsaw Bio-Base "With Colored Samples" V2 Scenario Results.

Models	GoogleNet	Resnt-50	ResNet101
Test accuracy (%)	87.4659	95.3678	95.6403
Computational Time	32 min. 23 sec.	41 min. 52 sec.	71 min. 41 sec.
TPR (%)	86.1020	94.4374	92.8677
PPR (%)	89.3754	96.9335	96.1835
FNR (%)	13.8980	5.5626	7.1323
FDR (%)	10.6246	3.0665	3.8165

4.3.5.3. Warsaw plus CASIA with colored samples

In this case, we trained the models with colored samples. Applied the datasets, Warsaw Bio-Base Version-2 holds 616 colored iris images with CASIA-Interval; the total number of images used is 11,505, containing original and segmented samples.

The comparison between models according to the calculation of each model's recognition accuracy and confusion matrix results in Table (4.11).

Table 4.11. Warsaw – CASIA "With Colored Samples" Scenario Results.

Models	**GoogleNet**	**Resnt-50**	**ResNet101**
Test accuracy (%)	91.8379	98.2384	98.1210
Computational Time	56 min 36 sec	98 min 45 sec	195 min 52 sec
TPR (%)	89.7754	97.7998	97.4315
PPR (%)	93.2454	98.1551	98.4690
FNR (%)	10.2246	2.2002	2.5685
FDR (%)	6.7546	1.8449	1.5310

The mixed Warsaw-CAISA dataset scenario has the same conclusion as the previous colored cases, proving that the ResNet50 has a low error rate and better accuracy than other models.

However, table (4.12) compared validation and testing accuracy for colored and noncolored scenarios.

Table 4.12. Comparison between Colored and Non-Colored Scenarios.

Validation Accuracy (%)			
Models	**Warsaw V1**	**Warsaw V2**	**Warsaw Plus CASIA**
GoogleNet Colored	92.61	88.50	94
GoogleNet Non-Colored	90.36	90.52	96
ResNet50 Colored	96.31	96.79	98.2
ResNet50 Non-Colored	97.18	96.36	98.2
ResNet101 Colored	96.31	93.98	98.45
ResNet101 Non-Colored	96.38	96.52	98.15
Testing Accuracy (%)			
Models	**Warsaw V1**	**Warsaw V2**	**Warsaw Plus CASIA**
GoogleNet Colored	91	86.10	91.83
GoogleNet Non-Colored	90	86.07	93.8
Resnet50 Colored	94.77	95.36	98.23
Resnet50 Non-Colored	94.26	94.38	97.80
Resnet101 Colored	93.28	95.64	98.12
Resnet101 Non-Colored	95	96.36	98

The comparison results show no significant change in the validation and testing accuracy between colored and non-colored scenarios. Nevertheless, there is no doubt that the elapsed time increased when utilizing the colored images.

In the latter scenarios, we will independently study the segmented iris images and compare them with non-segmented (original image results), using transfer learning of pre-trained networks (focusing on only diseases datasets, Warsaw V1, and Warsaw V2.

4.3.6. Scenario No. (6) Two Layers of Transfer Learning

For Warsaw Bio-Base versions 1 and 2, in the segmentation part, 619 images of V1 and 1571 images of V2 have been segmented successfully; both versions contain one or multiple diseases of the left and right eyes. where CASIA contains 5174 segmented iris images. In this scenario, the models will examine only segmented irises.

As is well known that GoogleNet, ResNet50, and ResNet101 trained on large size of images like animals, plants, etc., so somehow, these types of images are unrelated to our datasets; thus, the scenario aims to transfer learned models after training them on the CASIA images and reuse them on the Warsaw versions (two-layers training scenario) to boost the models' performance for better recognition accuracy in the case of segmented eye diseases.

Tables (4.13) and (4.15) are the results of the origin pre-trained models, where Tables (4.14) and (4.16) are the results of the transferred learning models (two-layers training scenario) implemented on Warsaw V1 then Warsaw V2 and Table (4.17) shows the results of the only CASIA samples of the original pre-trained models.

Table 4.13. Warsaw V1 experiment result of the original pre-trained models.

Models	**GoogleNet**	**Resnt50**	**ResNet101**
Test accuracy (%)	91.2281	96.4912	98.2456
Computational Time	2 min. 22 sec.	4 min. 30 sec.	9 min. 23 sec.
Test TPR (%)	90.1961	96.0784	98.0392
Test PPR (%)	95.2899	97.9592	99
Test FNR (%)	9.8039	3.9216	1.9608
Test FDR (%)	4.7101	2.0408	1
Validation Accuracy (%)	78.2946	91.4729	93.0233
Validation TPR (%)	78.4906	91.6981	92.4528
Validation PPR (%)	80.4808	94.0064	94.2308
Validation FNR (%)	21.5094	8.3019	7.5472
Validation FDR (%)	19.5192	5.9936	5.7692
Training Accuracy (%)	100.00	100.00	100.00

Table 4.14. Warsaw V1 experiment result of the CASIA transferred learning.

Models	GoogleNet	Resnt50	ResNet101
Test accuracy (%)	94.2623	98.5	99.1803
Computational Time	5 min	12 min 29 sec	18 min 56 sec
Test TPR (%)	94.0252	98.7421	99.0566
Test PPR (%)	96.2579	98.4277	99.3711
Test FNR (%)	5.9748	1.2579	0.9434
Test FDR (%)	3.7421	1.5723	0.6289
Validation Accuracy	92.7711	97.4170	98.3936
Validation TPR (%)	90.5481	97.5157	98.2390
Validation PPR (%)	93.9377	98.3349	98.8320
Validation FNR (%)	9.4519	2.9635	1.7610
Validation FDR (%)	6.0623	1.6651	1.1680
Training Accuracy (%)	100.00	100.00	100.00

Table 4.15. Warsaw V2 experiment result of the original pre-trained models.

Models	GoogleNet	Resnt50	ResNet101
Test accuracy (%)	79.4521	90.4110	94.5205
Computational Time	7 min 5 sec.	12 min 57 sec.	28 min 11 sec.
Test TPR (%)	77.2377	89.5833	93.5185
Test PPR (%)	84.7849	94.7691	96.4052
Test FNR (%)	22.7623	10.4167	6.4815
Test FDR (%)	15.2151	5.2309	3.5948
Validation Accuracy	80.1205	91.2651	90.3614
Validation TPR (%)	77.0164	90.0358	87.4673
Validation PPR (%)	86.4777	92.6780	91.3259
Validation FNR (%)	22.9836	9.9642	12.5327
Validation FDR (%)	13.5223	7.3220	8.6741
Training Accuracy (%)	90.00%	100.00%	100.00%

Table 4.16. Warsaw V2 experiment result of the CASIA transferred learning.

Models	GoogleNet	Resnt50	ResNet101
Test accuracy (%)	83.5616	93.1507	92.4658
Computational Time	5 min. 56 sec.	11 min 28 sec	23 min 49 sec
Test TPR (%)	83.2562	91.2037	91.5895
Test PPR (%)	90.4035	95.6106	94.0850
Test FNR (%)	16.7438	8.7963	8.4105
Test FDR (%)	9.5965	4.3894	5.9150
Validation Accuracy	83.4337	93.6747	94.2771
Validation TPR (%)	81.2790	91.2389	91.8584
Validation PPR (%)	89.6738	95.7862	94.9465
Validation FNR (%)	18.7210	8.7611	8.1416
Validation FDR (%)	10.3262	4.2138	5.0535
Training Accuracy (%)	100%	100%	100%

Table 4.17. CASIA in case of only segmented iris images.

Models	GoogleNet	Resnt50	ResNet101
Test accuracy (%)	93.2331	98.4962	99.0602
Computational Time	19 min. 52 sec.	39 min. 30 sec.	81 min. 59 sec.
Test TPR (%)	93.1268	98.2906	99.3590
Test PPR (%)	96.2485	99.0374	99.3803
Test FNR (%)	6.8732	1.7094	0.6410
Test FDR (%)	3.7515	0.9626	0.6197
Validation Accuracy	93.0070	98.8012	99.2008
Validation TPR (%)	92.6433	98.0499	98.8445
Validation PPR (%)	95.5189	98.7477	99.3123
Validation FNR (%)	7.3567	1.9501	1.1555
Validation FDR (%)	4.4811	1.2523	0.6877
Training Accuracy (%)	100%	100%	100%

Although ResNet models obtained 98% accuracy with Warsaw V1, Warsaw V2 achieved only 93% and 92% test accuracy with the ResNet50 and ResNet101 models; hence, this study advises modifying the model's hyperparameters by increasing the number of epochs from 20 to 500. This procedure enabled the ResNet50 to attain 97% test accuracy, enhancing the training and validation accuracy and decreasing error rates. Table 4.18 shows the results of the different number of epochs.

Table 4.18. Warsaw V2 result of the CASIA transferred learning.

Models With 500 Epochs	GoogleNet	Resnt-50	ResNet101
Test accuracy (%)	90.4110	97.2603	96.575
Computational Time	147 min. 58 sec.	318 min. 12 sec.	642 min. 35 sec.
Test TPR (%)	89.1975	96.2963	95.8333
Test PPR (%)	94.3603	98.3654	98.2051
Test FNR (%)	10.8025	3.7037	4.1667
Test FDR (%)	5.6397	1.6346	1.7949
Validation Accuracy	89.7590	95.7831	94.5783
Validation TPR (%)	88.3298	93.7512	91.2453
Validation PPR (%)	90.9127	97.0420	95.9535
Validation FNR (%)	11.6702	6.2488	8.7547
Validation FDR (%)	9.0873	2.9580	4.0465
Training Accuracy (%)	100%	100%	100%

Scenario No. 6 has delivered the following bases:

1. Transfer learning of the model's used related species of samples decreased the model's error rates and improved the training, validation, and testing accuracy for all three models GoogleNet, ResNet101, and ResNet50.
2. ResNet50 balanced time consumption and test accuracy; compared with GoogleNet and ResNet101; thus, ResNet50 is the preferred model.
3. The test accuracy in the case of diseases for only segmented images achieved excellent accuracy of 99% for Warsaw V1 and 97.26% for Warsaw V2.
4. Increasing the number of training epochs for Warsaw V2 improved the model's accuracy by 4%, reducing error rates and increasing computational time. Furthermore, there is no error record for most individuals whose images were acquired in two sessions.
5. The test accuracy of CASIA (healthy eyes) for only segmented images achieved excellent validation and test accuracy of 99%, while the false discovery rate hits the zeros.

PART 5

DISCUSSION & CONCLUSION

5.1. DISCUSSION OF THE IRIS SEGMENTATION RESULTS

This section contains two parts; the first demonstrates the general discussion of iris segmentation experiment results, while the second discusses iris segmentation evaluation results of the ground truth.

5.1.1. Iris Segmentation General Discussion

The previous analysis of the effects of eye diseases on the iris segmentation process confirms many conclusions:

1. Some eye diseases affect the iris segmentation significantly, like blindness, some pupil distortion issues, some bloody eye issues, and most retinal detachment situations (with silicon oils only). Figure (5.1) confirms this point.

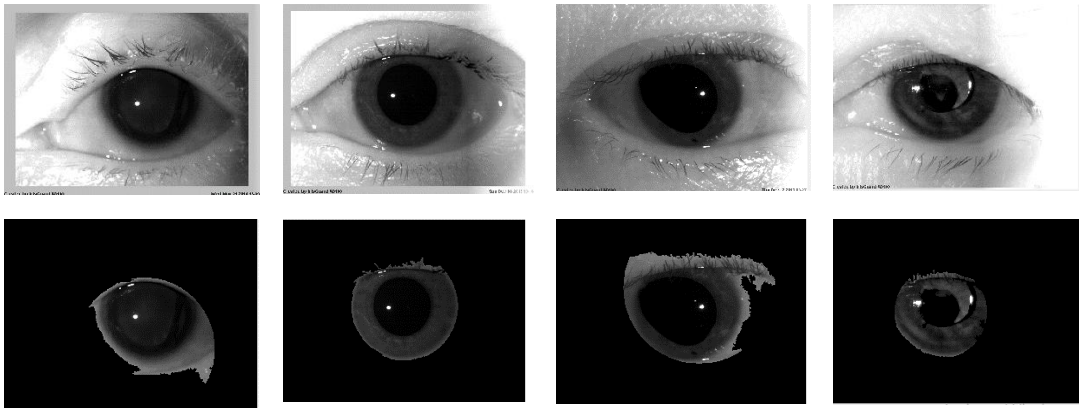

Blindness | retinal detachment | retinal detachment with silicon oil | Distorted Pupil

Figure 5.1. Examples of iris segmentation in case of partially-effect eye diseases.

2. Some diseases do not affect the iris segmentation, like blurry, some lens problems, and some corneal problems, as shown in Figure (5.2).

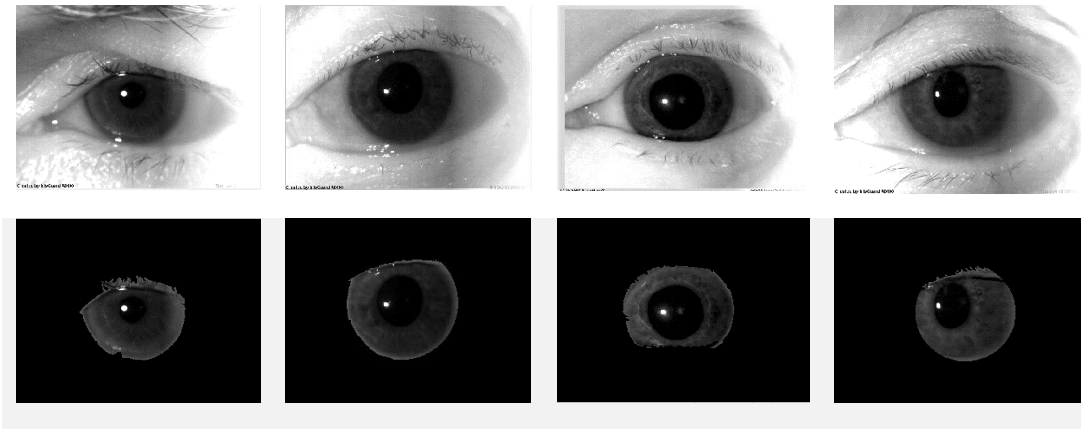

Blurry Lens | Blurry Eyes | corneal haze, corneal ulcer, corneal vascularization | corneal swelling, opacified lens

Figure 5.2. Examples of iris segmentation cases of mild or no-effect eye diseases.

3. Some eye diseases affect iris segmentation, especially when other diseases accompany them. Many examples of this case include cataract, glaucoma, iridectomy, synechiae, eye trauma, pupil dilation, narrow iris, Aphakia, and Pseudophakic. Figure (5.3) illustrates some of these cases.

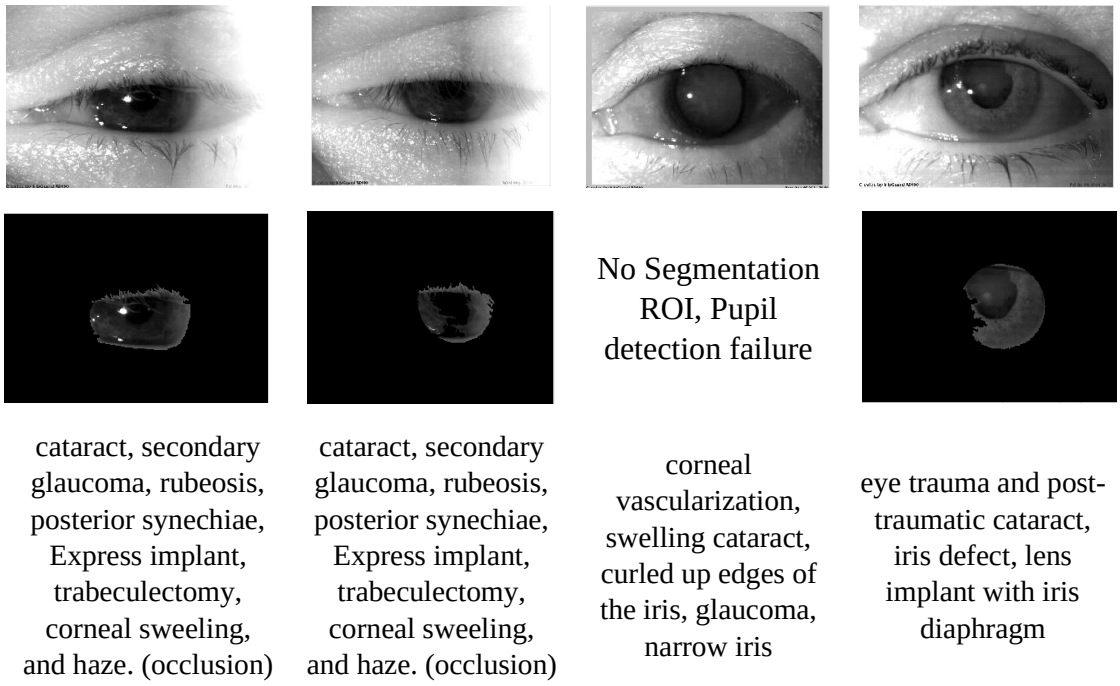

Figure 5.3. Examples of iris segmentation in the case of mixed eye diseases.

Although multiple diseases in some cases can cause problems, they do not have those bad effects on iris segmentation when they exist individually. For example, there are no segmentation errors caused by samples, including only cataract disease. The same conclusion is true for other diseases like Glaucoma, iridectomy, anterior synechiae, pseudophakic, blurred lens, iridescent lens, corneal ulcer, and aphakia. Figure (5.4) includes some examples of iris segmentation in the case of individual non-effective eye diseases.

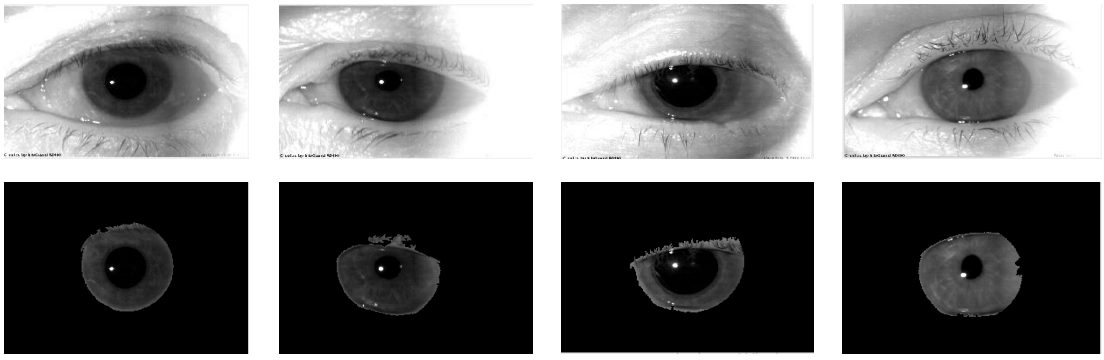

Cataract Pseudophakic iridectomy Aphakia

Figure 5.4. Some examples of iris segmentation in the case of single eye diseases.

Although healthy cases have no medical problems, the segmentation fails due to some other factors like the huge occlusion of eyelids. In case 83 (left eye) specifically, the samples are listed as healthy ones, but they contain wide pupils, affecting the iris segmentation, as shown in figure (5.5).

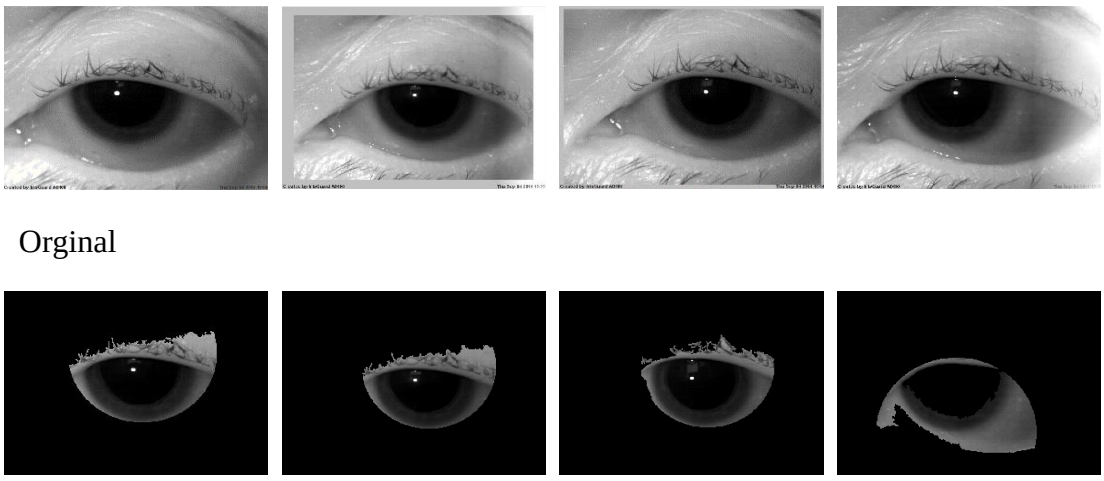

Orginal

Segmented

Figure 5.5. Bad segmentation results of Healthy case 83-Left eye.

5.1.2. Discussion of Ground Truth Evaluation Results

The ground truth iris segmentation results prove the fact that the segmentation approach is robust against false positives (non-iris regions), and its sensitivity against false negatives (rejected true iris regions) is good enough since the proposed methodology achieved a very low FPR of 0.799% and low FNR of 5.494% of Warsaw Bio-Base V1 dataset.

5.2. DISCUSSION OF IRIS RECOGNITION RESULTS

The scenarios experiment presents the following observations:

1. For Warsaw V1, the transfer-related learning experiment of the two layers training scenarios, show an excellent accuracy of 93%, 98.5%, and 99% for the three pre-trained models, GoogleNet, ResNet50, and ResNet101. Compared with the first scenario, where the models trained originally on the large unrelated datasets. Scenario No.6 also proves that the segmented samples improved the network's performance and decreased the False Negative Rates and False Discovery Rates compared with the results of mixed samples (original and segmented) of Warsaw V1.
2. The fusion of raw and segmented eye images achieved 96 % accuracy.
3. The ResNet model achieved 99% accuracy when combining healthy and diseased datasets in most scenarios.
4. The experiment results of the splitting scenario No.4 prove that the splitting data as 70% training, 20% validation, and 10% test is the best division method for the proposed models.

5. The ResNet50 achieved the highest validation accuracy and balance-of computational time with high test accuracy. Besides that, ResNet50 showed a good convergence, as figure (5.6), (5.7), and (5.8) shows (For example, in scenario No.1, ResNet50 reached 80% accuracy between epochs 2 and 3, while GoogleNet got the same accuracy between epochs 5 and 6, for Warsaw Bio-Base V1. Similarly, for the Warsaw Bio-Base V2 dataset, ResNet50 reached 80% accuracy between epochs 2 and 3, while GoogleNet needed eight training epochs to reach the same accuracy.

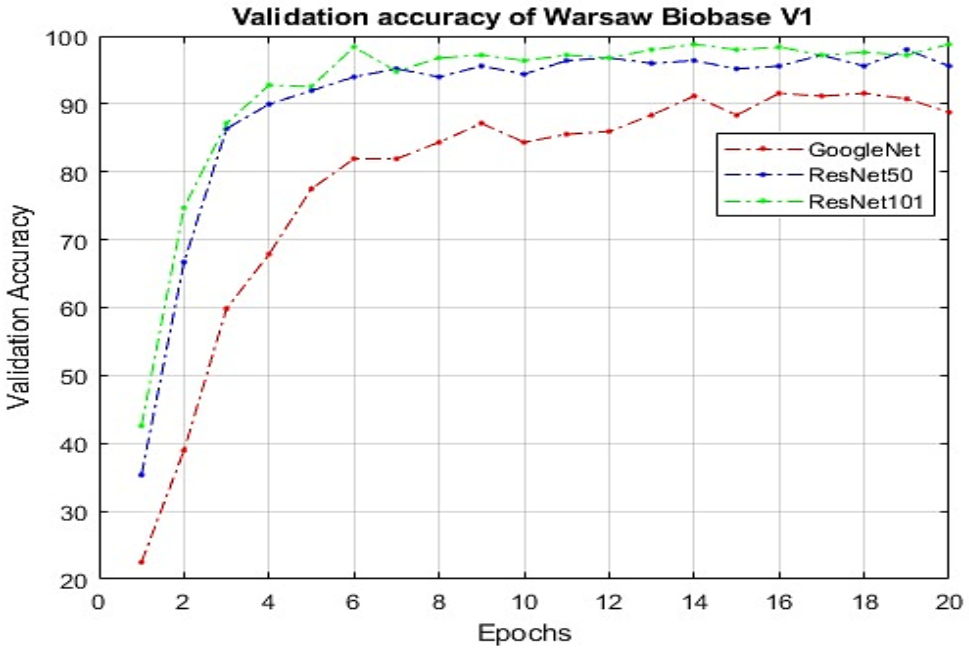

Figure 5.6. Validation accuracy of the Warsaw V1 dataset (Scenario No.1).

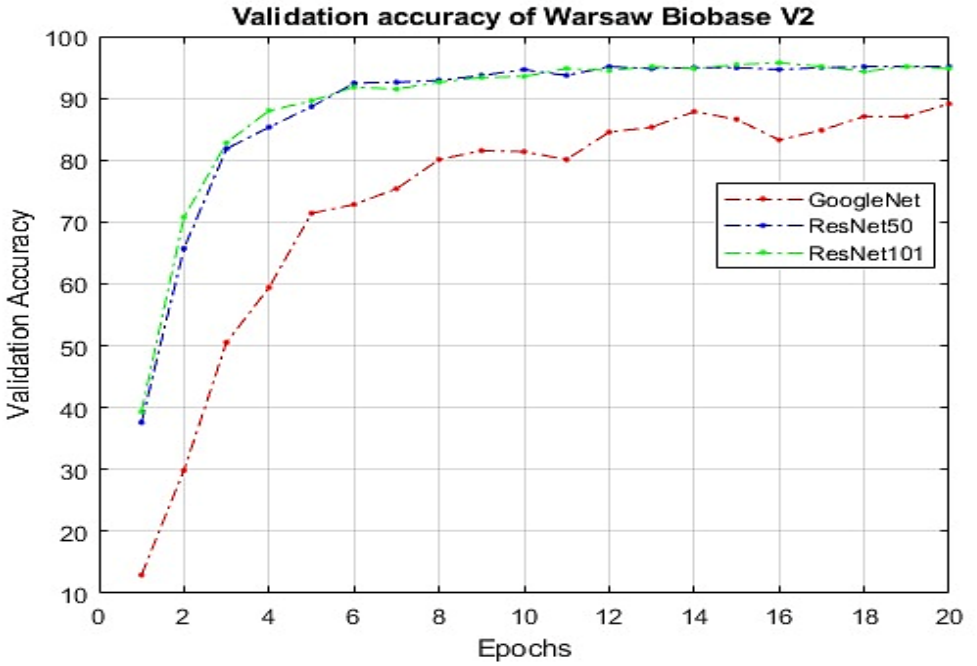

Figure 5.7. Validation accuracy of the Warsaw V2 dataset (Scenario No.1).

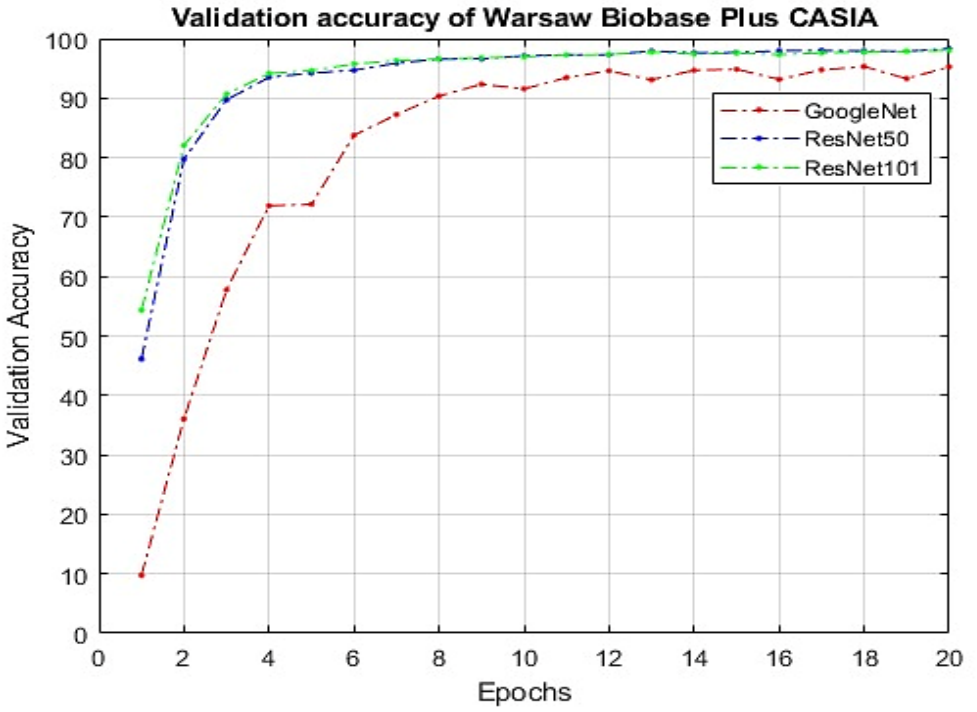

Figure 5.8. Validation accuracy of the CASIA dataset (Scenario No.1).

6. Scenario No. 5 demonstrated no significant change in validation and testing accuracy when colored images were involved. However, the computational time increased in all models.
7. The suggested models successfully recognized the segmented irises of CASIA datasets. The accuracy reached 99%.
8. Despite that CASIA is mentioned as a total healthy case, it is noted that some abnormal eye images are suffering from iris dilations. Despite that, the suggested models overcome these problems and successfully recognize them.
9. Combining healthy and diseased datasets improved the network's validation and testing, which achieved 98.66% test accuracy.
10. Although, Warsaw V2, multiple diseases seriously affecting most of the iris geometry, like the samples of 1090, leads to frequent error in most scenarios. The individual 0090 left eyes are suffering from multiple diseases like; vitrectomy with oil and lens removal, corneal injury and sutures, oil in the anterior chamber, and aphakia; these eye samples contain images acquired by two sessions, session 1: 2014-10-09 (before surgery), session 2: 2014-10-13 (after surgery) with high occlusion, leads to a frequent fault in most scenarios. However, according to table 4.20, after increasing the number of epochs to 500, the resnet model overcome such problems and successfully recognize these individuals and no error records.

5.2.1. Discussion of The Original First Three Scenarios

In the following discussion, a detailed disease-related study is introduced to identify the effect of eye diseases on the performance of iris recognition. Three different scenarios are used, Warsaw-Bio-Base-V1, Warsaw-Bio-Base-V2, and fused Warsaw-CASIA datasets training scenarios (with original split 70% training, 20% validation, and 10% test). For the three scenarios, samples with more than 50% FNR or more than 50% FDR are collected and listed in tables (5.1, 5.2, and 5.3).

Experiments on the Warsaw V1 dataset (Table 5.1) show that the suggested deep networks differ in performance with a transcendence of the ResNet50 among the three used networks.

There is only no frequent wrong case among networks; furthermore, results also indicate that there are only two samples (0030 and 0038) with two false discoveries/errors (of GoogleNet results). All other samples have only one fault. These results prove that eye diseases have no big effect on iris recognition since the faulty samples differ among models.

Sum$_r$: the sum of all true and wrong samples horizontally, **Sum$_c$**: the sum of all true and wrong samples vertically, **TP**: true positives (The frequent false-detected samples are highlighted).

Warsaw V2 dataset is an extension of V1, including more eye diseases. Results in Table (5.2) illustrate that classes 0004, 0076, 0082, 0086, 0103, and 1090 have frequent faults. Sample 0004 has cataract and phacoemulsification eye diseases and includes only one false result. On the other hand, sample 0086 has many eye diseases (corneal ulcer, sediments, and posterior synechiae) and includes two faults. Similarly, sample 0022 has cataract corneal haze and pseudophakic eye diseases, causing one false negative and three false discoveries.

Table 5.1. Warsaw Bio-Base V1 Scenario Analysis Results.

GoogleNet				ResNet50				ResNet101			
Class	**Sum_r**	**Sum_c**	**TP**	**Class**	**Sum_r**	**Sum_c**	**TP**	**Class**	**Sum_r**	**Sum_c**	**TP**
0000	1	1	0	**0041**	1	2	1	**0039**	2	1	1
0012	2	1	1					**0053**	2	1	1
0022	2	1	1								
0030	1	3	1								
0036	2	2	1								
0037	2	1	1								
0038	1	3	1								
0057	2	1	1								

Table 5.2. Warsaw Bio-Base V2 Scenario Analysis Results.

GoogleNet				ResNet50				ResNet101			
Class	**Sum_r**	**Sum_c**	**TP**	**Class**	**Sum_r**	**Sum_c**	**TP**	**Class**	**Sum_r**	**Sum_c**	**TP**
0011L	4	2	2	**0004L**	2	2	1	**0004L**	2	2	1
0020L	3	1	1	**0076L**	2	1	1	**0082L**	1	2	1
0022L	3	5	2	**0082L**	1	2	1	**0086L**	2	4	2
0025L	2	1	1	**0086L**	2	4	2				
0031L	2	1	1	**0103L**	2	1	1				
0037L	2	4	2	**0108L**	2	1	1				
0047L	2	4	2	**1090L**	2	1	1				
0048L	3	1	1								
0052L	2	1	1								
0053L	2	1	1								
0068L	2	1	1								
0076L	2	1	1								
0082L	1	2	1								
0094L	2	1	1								
0095L	1	2	1								
0096L	1	1	0								
0100L	1	2	1								
0103L	2	1	1								
0104L	2	1	1								
0110L	2	2	1								
0111L	2	2	1								
0113L	2	1	1								
0114L	2	1	1								
0116L	1	3	1								
1090L	2	1	1								

Two fault samples for Warsaw and CASIA fused datasets result in only one error (0110 and 1090). For individual 0110, there are multiple diseases like (secondary glaucoma, vitrectomy, oil in the anterior chamber, pseudophakia, aphakia, vitrectomy, and blindness). On the other hand, the eye diseases of sample 1090 are opacified lens, uveitis, glaucoma, phacoemulsification with iris correction, aphakia, retinal detachment, and fibers, as shown in Table (5.3).

Table 5.3. Warsaw-CASIA Scenario Analysis Results.

GoogleNet				**ResNet50**				**ResNet101**			
Class	**Sum_r**	**Sum_c**	**TP**	**Class**	**Sum_r**	**Sum_c**	**TP**	**Class**	**Sum_r**	**Sum_c**	**TP**
0025C	1	2	1	**0012C**	2	1	1	**0004L**	2	1	1
0046C	1	2	1	**0013C**	2	1	1	**0018L**	1	2	1
0088L	2	1	1	**0021L**	2	1	1	**0027L**	3	1	1
0110L	2	1	1	**0082L**	1	2	1	**0038L**	2	1	1
0113L	2	1	1	**0090L**	4	1	1	**0073L**	2	4	2
0183C	2	1	1	**0107L**	2	1	1	**0090L**	4	2	2
0184C	1	2	1	**0247C**	2	1	1	**0109L**	2	1	1
0202C	2	1	1	**1090L**	2	1	1	**0110L**	2	2	1
0204C	1	2	1					**0111L**	2	4	2
0226C	2	1	1					**0112L**	1	2	1
1090L	2	1	1					**0114L**	2	1	1

Table (5.4) includes the samples with many errors and related eye diseases (Warsaw V1, Warsaw V2, fused Warsaw, and CASIA datasets). However, the 0090 sample has many errors because of multiple eye diseases like an intraocular foreign object, vitrectomy with oil and lens removal, corneal injury and sutures, oil in the anterior chamber, and aphakia.

Table 5.4. Most frequent fault samples with their corresponding eye diseases.

Sample	**Eye Diseases**	**Number of scenarios/models in which fault is detected**	**Number of false negatives**	**Number of false discoveries**
0022	cataract, pseudophakic	2 scenario/ 1 model	3/5	3/5
0086	corneal ulcer, sediments, posterior synechiae	1 scenario/ 2 models	0/2	2/4

Sample	Eye Diseases	Number of scenarios/models in which fault is detected	Number of false negatives	Number of false discoveries
0090	intraocular foreign object, vitrectomy with oil and lens removal, corneal injury and sutures, oil in the anterior chamber, aphakia	1 scenario/ 2 models	ResNet50: 3/4 ResNet101: 2/4	ResNet50: 0/1 ResNet101: 0/2

Posterior synechiae and other eye conditions that change or cover the iris tissue have influences on iris recognition, as shown in Table (5.4). These conditions include lens problems, corneal injury or sutures, oily eyes, and foreign objects that occlude the iris tissues. The effect of such diseases is partial. According to the CASIA dataset, we find no frequent error prototype. The faults happen due to some imaging conditions like the high occlusion.

5.2.2. Discussion of The Splitting Scenarios

Three different splitting scenarios are used; the first uses 70% of data for training, 20% for validation, and 10% for test sets, while the second uses the same training split but with 15% for validation and the same for test sets. The last splitting is to make the training set as 60% of the data, while the validation takes 20%, and the rest will remain for test sets. Tables (5.5, 5.6, and 5.7) compare these scenarios using the GoogleNet, ResNet50, and ResNet101 deep learning networks.

Table 5.5. Three GoogleNet different splitting scenarios analysis results.

70% 15% 15%				**60% 20% 20%**				**70% 20% 10%**			
Class	**Sum_r**	**Sum_c**	**TP**	**Class**	**Sum_r**	**Sum_c**	**TP**	**Class**	**Sum_r**	**Sum_c**	**TP**
0001L	4	2	2	**0026L**	2	1	0	**0025C**	1	2	1
0015L	4	2	2	**0028L**	3	2	1	**0046C**	1	2	1
0022C	2	1	1	**0046C**	2	1	1	**0088L**	2	1	1
0022L	4	7	3	**0048L**	5	6	3	**0110L**	2	1	1
0026L	2	1	1	**0070L**	2	1	1	**0113L**	2	1	1
0028L	2	2	1	**0073L**	5	2	2	**0183C**	2	1	1
0031L	4	2	2	**0076C**	8	17	8	**0184C**	1	2	1

70% 15% 15%				60% 20% 20%				70% 20% 10%			
Class	**Sum_r**	**Sum_c**	**TP**	**Class**	**Sum_r**	**Sum_c**	**TP**	**Class**	**Sum_r**	**Sum_c**	**TP**
0032C	1	2	1	**0082L**	2	1	1	**0202C**	2	1	1
0036L	4	2	2	**0089L**	2	1	1	**0204C**	1	2	1
0037L	4	8	4	**0090L**	8	4	4	**0226C**	2	1	1
0041L	4	2	2	**0094L**	5	11	5	**1090L**	2	1	1
0042L	4	3	2	**0095L**	2	1	1				
0051L	4	3	2	**0096L**	2	1	0				
0053L	4	1	1	**0107L**	3	2	1				
0069C	6	2	2	**0109L**	4	3	2				
0070L	1	2	1	**0110L**	3	1	1				
0089L	2	1	1	**0111L**	4	5	2				
0090L	6	4	2	**0116L**	2	2	1				
0094L	4	2	2	**0158C**	3	1	1				
0096L	2	2	1	**0221C**	4	2	2				
0104L	3	1	1	**0234C**	4	1	1				
0111L	3	1	1	**0242C**	2	1	1				
0117L	4	3	2	**1090L**	4	6	2				
0131C	5	13	5								
0155C	1	1	0								
194C	2	1	1								
245C	2	1	1								
247C	4	2	2								

Table 5.6. Three ResNet50 different splitting scenarios analysis results.

70% 15% 15%				60% 20% 20%				70% 20% 10%			
Class	**Sum_r**	**Sum_c**	**TP**	**Class**	**Sum_r**	**Sum_c**	**TP**	**Class**	**Sum_r**	**Sum_c**	**TP**
0028L	2	1	1	**0028L**	**3**	**1**	**1**	**0012C**	2	1	1
0082L	2	4	2	**0046C**	**2**	**1**	**1**	**0013C**	2	1	1
0196C	2	1	1	**0110L**	**3**	**4**	**2**	**0021L**	2	1	1
				0116L	**2**	**1**	**1**	**0082L**	1	2	1
				0155C	**2**	**1**	**1**	**0090L**	4	1	1
								0107L	2	1	1
								0247C	2	1	1
								1090L	2	1	1

Table 5.7. Three ResNet101 different splitting scenarios analysis results.

70% 15% 15%				60% 20% 20%				70% 20% 10%			
Class	**Sum_r**	**Sum_c**	**TP**	**Class**	**Sum_r**	**Sum_c**	**TP**	**Class**	**Sum_r**	**Sum_c**	**TP**
0028L	2	1	1	**0016C**	2	1	1	**0004L**	2	1	1
0070L	1	1	0	**0022L**	5	8	4	**0018L**	1	2	1
0090L	6	4	3	**0028L**	3	1	1	**0027L**	3	1	1
0096L	2	1	1	**0046C**	2	1	1	**0038L**	2	1	1

70% 15% 15%				60% 20% 20%				70% 20% 10%			
Class	**Sum_r**	**Sum_c**	**TP**	**Class**	**Sum_r**	**Sum_c**	**TP**	**Class**	**Sum_r**	**Sum_c**	**TP**
0109L	3	2	1	**0110L**	3	6	3	**0073L**	2	4	2
0110L	2	1	1	**0236C**	2	1	1	**0090L**	4	2	2
								0109L	2	1	1
								0110L	2	2	1
								0111L	2	4	2
								0112L	1	2	1
								0114L	2	1	1

Many diseases affect the left eye, the right eye, or both. In many cases of eye diseases, the deep learning networks perform well. However, ResNet has better performance than GoogleNet in all scenarios. ResNet50 especially has the best iris recognition performance in the case of diseases. ResNet50 has only two low samples performance (28 and 82 individuals). In contrast, GoogleNet has six bad samples performance. However, ResNet101 includes four bad results.

Regarding eye disease, the iris recognition performance is less affected by eye diseases than the iris segmentation. No singular eye diseases affect iris recognition. While in contrast, we found some cases in which iris segmentation is affected even under singular eye diseases. For multiple eye diseases, iris recognition can be affected, but this depends on the diseases themselves. Table (5.8) includes the frequent fault samples across all splitting scenarios.

Table 5.8. Most frequent fault samples (Splitting Scenarios).

Sample	Eye Diseases	Number of scenarios/ models in which fault is detected	Number of faults (FNs) of all models/ number of samples	Number of faults (FDs) of all models/ number of samples
0026	aphakia, posterior and anterior synechiae, retinal detachment surgery, secondary cataract	2 scenarios/ 1 model	3/4	1/2
0028	post-trauma cataract, anterior synechiae, iris scarring	2 scenarios/ 3 models	3/5	2/4
0082	glaucoma, pemphigoid, trabeculectomy, pseudophakic, corneal haze, vascularization	2 scenarios/ 1 model	0/3	3/6

Sample	Eye Diseases	Number of scenarios/ models in which fault is detected	Number of faults (FNs) of all models/ number of samples	Number of faults (FDs) of all models/ number of samples
0090	intraocular foreign object, vitrectomy with oil and lens removal, corneal injury and sutures, oil in the anterior chamber, aphakia	3 scenarios/3 models	GoogleNet:8/14 ResNet:5/10	GoogleNet:2/8 ResNet:1/6
0094	intraocular foreign body in the cornea	2 scenarios/1 model	2/9	6/13
0109	blunt wood trauma to the eye, blood in the anterior chamber	2 scenarios/1 model	3/5	1/3
0110	secondary glaucoma, vitrectomy, oil in the anterior chamber, pseudophakia, blindness, aphakia, band keratopathy	Three scenarios/2 models	2/7	4/9
0111	retinal detachment and vitrectomy with oil, pseudophakic oil in the anterior chamber	2 scenarios/1 model	4/7	3/6
1090	uveitis, glaucoma, phacoemulsification with iris correction, aphakia, retinal detachment, fibers, opacified lens	2 scenarios/1 model	3/6	4/7

Results show that some mixed diseases (blindness, bloody eyes, eye trauma, oil in the eye, anterior synechiae, iris scarring, glaucoma, pemphigoid, trabeculectomy, pseudophakic, corneal haze, vascularization, intraocular foreign bodies in eye, retinal detachment, phacoemulsification, post-trauma cataract) can affect iris recognition partially.

Results also indicate no completely false recognition in the case of any singular or plural diseases (All recognition errors occurred to some test samples and not all samples of the same eye). This conclusion differs from iris segmentation results, where some eye diseases cause completely false segmentation results for some test samples.

5.2.3. Discussion of The Colored Samples Scenario

Three new scenarios are obtained after adding the colored samples to the original scenarios (gray-scale iris images). Tables (5.9, 5.10, and 5.11) include the results of the three scenarios after adding the colored iris samples.

Table 5.9. Warsaw “with colored samples” V1 Scenario analysis results.

GoogleNet				ResNet50				ResNet101			
Class	**Sum_r**	**Sum_c**	**TP**	**Class**	**Sum_r**	**Sum_c**	**TP**	**Class**	**Sum_r**	**Sum_c**	**TP**
0012	2	6	2	**0000**	1	2	1	**0004**	2	1	1
0014	2	1	1	**0004**	2	1	1	**0012**	2	4	2
0022	2	2	1	**0006**	2	1	1	**0057**	3	1	1
0025	2	2	1	**0028**	1	2	1				
0028	1	3	1	**0031**	2	1	1				
0054	4	2	2	**0058**	2	1	1				

Table (5.9) illustrates that there are three frequent fault samples which are "0004", "0012", and "0028". Both samples, "0004" and "0028", have a few false discoveries.

However, sample "0012" has too many false discoveries (4 for GoogleNet and 2 for ResNet101). Sample "0012" has a cataract and pseudophakic eye diseases.

Table 5.10. Warsaw “with colored samples” V2 scenario analysis results.

GoogleNet				ResNet50				ResNet101			
Class	**Sum_r**	**Sum_c**	**TP**	**Class**	**Sum_r**	**Sum_c**	**TP**	**Class**	**Sum_r**	**Sum_c**	**TP**
0012L	2	5	1	**0025L**	2	1	1	**0081L**	3	3	1
0017L	6	4	3	**0033L**	2	1	1	**0096L**	2	1	1
0021L	2	4	2	**0108L**	2	1	1	**0110L**	**2**	**1**	**1**
0037L	2	5	2	**0111L**	2	1	1	**0116L**	1	1	0
0041L	3	2	1	**1090L**	2	1	1				
0051L	3	4	2								
0068L	4	2	2								
0096L	2	1	0								
0104L	3	1	1								
0106L	3	2	1								
0110L	2	2	1								
0112L	1	2	1								
0114L	4	3	2								
0117L	4	2	2								

For Warsaw Bio-Base V2, the GoogleNet is the network with the most faults compared to ResNet networks, with less error rate and better performance.

For the GoogleNet scenario, samples (0012, 0017, 0021, 0051, 0068, 0114 and 00117) have multiple false negatives and discoveries. However, the only frequent fault sample among all scenarios is the 0021 sample with only one fault.

Table 5.11. Warsaw-CASIA "with colored samples" scenario analysis results.

GoogleNet				**ResNet50**				**ResNet101**			
Class	**Sum_r**	**Sum_c**	**TP**	**Class**	**Sum_r**	**Sum_c**	**TP**	**Class**	**Sum_r**	**Sum_c**	**TP**
0004C	3	1	1	**0022L**	4	2	2	**0003L**	4	2	2
0015C	2	1	1	**0035C**	2	1	1	**0016C**	2	1	1
0036L	4	2	2	**0070L**	2	3	1	**0028L**	2	1	1
0042L	4	4	2	**0115L**	2	2	1	**0111L**	3	5	2
0050C	2	7	2	**0249C**	1	2	1	**0115L**	2	1	1
0051C	2	4	2								
0052C	2	1	1								
0062C	2	1	1								
0070L	2	2	0								
0082L	3	4	2								
0091C	4	2	2								
0096L	3	3	1								
0099C	5	10	5								
0106L	4	2	1								
0108L	4	2	2								
0111L	3	1	1								
0115L	2	1	0								
0116L	2	1	1								
0117C	6	3	3								
0150C	2	4	2								
0155C	1	3	1								
0170C	7	3	3								
0190C	2	1	1								
0236C	1	1	0								
0245C	2	1	1								
1042L	4	2	2								
1090L	4	2	2								

For the mixed Warsaw-CAISA dataset scenario, the same conclusion of GoogleNet and ResNet is acquired. The most frequent fault in this scenario is sample 0115, in which there are one false negative and two false discoveries of the GoogleNet scenario.

On the other hand, there are only one false negative and one discovery error for ResNet scenarios.

The other frequent samples (0070 and 0111) have more error rates than sample 0115. For non-frequent fault samples, GoogleNet has the most significant number of samples with the most error rates. Table (5.12) includes the most frequent samples with the highest error rates of color-based scenarios.

Table 5.12. The most frequent samples with highest error rates in color scenarios.

Sample	**Eye Diseases**	**Number of scenarios/ models in which fault is detected**	**Number of faults (FNs) of all models/ number of samples**	**Number of faults (FDs) of all models/ number of samples**
0012	cataract, pseudophakic	2 scenarios/ 2 model**s**	GoogleNet: 1/4 ResNet: 0/2	GoogleNet: 8/11 ResNet: 2/4
0028	post-trauma cataract, anterior synechiae, iris scarring	2 scenarios/ 3 models	GoogleNet: 0/1 ResNet50: 0/1 ResNet101:1/2	GoogleNet: 2/3 ResNet50: 1/2 ResNet101:0/1
0096	retinal detachment surgery, aphakia, congenital cataract, anterior synechiae, distorted pupil, iridotomy, vitrectomy with oil replacement, rubeosis, and oil in the anterior chamber.	1 scenario/ 2 models	4/5	1/5
0110	secondary glaucoma, vitrectomy, oil in the anterior chamber, pseudophakia, blindness, aphakia, band keratopathy	1 scenario/ 2 models	GoogleNet: 1/2 ResNet: 1/2	GoogleNet:0/2 ResNet: 1/2
1090	uveitis, glaucoma, phacoemulsification with iris correction, aphakia, retinal detachment, fibers, opacified lens	2 scenarios/ 2 model	GoogleNet: 2/4 ResNet: 1/2	GoogleNet: 0/2 ResNet: 0/1

All scenarios showed a lower performance of GoogleNet against ResNets. GoogleNet has many samples with multiple false negatives and false discoveries.

The main idea is that these faults are not all repeated through scenarios. This concludes that GoogleNet performance is affected differentially by eye diseases due to different scenarios' conditions (splitting, adding more diseases, adding colored eye samples). On the other hand, ResNet shows a robust performance through all scenarios.

Regarding tables 4,8, and 12, the most frequent fault samples of all scenarios are listed in Table (5.13).

Table 5.13. The most frequent fault samples among all scenarios.

Sample	**Eye Diseases**	**Number of scenarios in which fault is detected**
0028	post-trauma cataract, anterior synechiae, iris scarring	Five scenarios / 3 models.
0090	intraocular foreign object, vitrectomy with oil and lens removal, corneal injury and sutures, oil in the anterior chamber, aphakia	Four scenario/ 3 models.
0110	secondary glaucoma, vitrectomy, oil in the anterior chamber, pseudophakia, blindness, aphakia, band keratopathy	Six scenarios/3 models.
1090	uveitis, glaucoma, phacoemulsification with iris correction, aphakia, retinal detachment, fibers, opacified lens	Six scenarios/3 models.

Table (5.13) proves that eye disease partially affects iris recognition. The most influential disease is those type of eye diseases that cover or change the structure of the iris partially or wholly. No singular disease can cause a big problem for the iris recognition system; for example, blindness people or those who have retinal detachment, injury, iris scarring, oily eyes, glaucoma, and synechiae affect the iris recognition partially by occurring some errors, but they do not limit or disable the iris recognition systems. For people with those diseases, iris recognition still works, but it needs more robust and high-performance systems.

5.2.4. Discussion of The Two-Layers Training Scenarios

In this part, the trained models of the two-layers training methodology will be considered. The previous discussion of the frequent fault will also be repeated for these models. Tables (5.14 and 5.15) show the fault samples with more than 50% FNR or 50% FDR of all 2-layer trained models of Warsaw V1 and V2 datasets.

Table 5.14. Warsaw V1 "Two-layers training" scenario analysis results.

GoogleNet				ResNet50				ResNet101			
Class	**Sum_r**	**Sum_c**	**TP**	**Class**	**Sum_r**	**Sum_c**	**TP**	**Class**	**Sum_r**	**Sum_c**	**TP**
0004	2	2	1	**0004**	2	1	1	**0004**	2	2	1
0006	2	1	1	**0018**	1	2	1	**0006**	2	1	1
0039	2	1	1	**0033**	2	1	1	**0039**	2	1	1
0052	2	1	1					**0052**	2	1	1
0053	2	1	1					**0053**	2	1	1

Table (5.14) shows that all frequent fault samples have a small number of false negatives and false discoveries for all scenarios. The most frequent fault is 0004, which, in the worst case, has only one false negative and one false discovery error.

Table 5.15. Warsaw V2 "Two layers training" scenario analysis results.

GoogleNet				ResNet50				ResNet101			
Class	**Sum_r**	**Sum_c**	**TP**	**Class**	**Sum_r**	**Sum_c**	**TP**	**Class**	**Sum_r**	**Sum_c**	**TP**
0004L	1	2	1	**0011L**	2	1	1	**0021L**	1	2	1
0005L	2	1	1	**0028L**	1	1	0	**0029L**	1	2	1
0017L	3	4	2	**0031L**	1	1	0	**0036L**	1	1	0
0021L	1	2	1	**0076L**	1	2	1	**0041L**	1	2	1
0022L	1	3	1	**0090L**	2	4	2	**0060L**	2	1	1
0023L	1	2	1	**1090L**	1	2	1	**0068L**	1	2	1
0031L	1	2	1					**0088L**	1	2	1
0039L	1	2	1					**0101L**	1	2	1
0060L	2	3	1					**0108L**	1	2	1
0063L	3	1	1								
0064L	4	8	4								
0071L	2	1	1								
0090L	2	1	1								
1111L	1	2	0								

Table (5.15) concludes that with more disease occurrences, the performance of GoogleNet becomes worse. However, this conclusion is not applicable for ResNets, which are not affected by eye diseases like GoogleNet.There are only two frequent-fault samples among GoogleNet and ResNet, "0090" and "0060" samples. Sample "0090" includes one false negative error in GoogleNet and two false discovery errors in ResNet50. On the other hand, sample "0060" includes one false negative and two false discovery errors in the case of GoogleNet. However, it includes only one false negative error in ResNet101.

In contrast, the ResNet results training scenario (Table 4.20) indicates no error records (FNR and FDR) for most data acquired during two different sessions. Thus, the findings indicate that if the treatment did not significantly alter the iris texture, it is possible to engage the individuals in the suggested models with no need to replace their samples even after treatment, for instance, the condition before and after surgery, the model successfully recognized the samples with individual 0090's and 0063's left eye, which had two sessions before and after cataract surgery.

5.2.6. Comparative Study

As a result, we can conclude that the ResNet models are less affected by eye diseases than GoogleNet in all training scenarios. Table (5.16) shows the iris testing accuracy attained by the proposed models compared with the related works.

Table 5.16. Results comparison of the current research and related works.

Author	Method	Dataset / Nu. Of Images	Dataset Challenge	Performance/ Remarks
Current Research	GoogleNet, ResNet50, ResNet101.	Warsaw V1/684 Images, Warsaw V2 1793 Images. CASIA V3/ 2639 Images.	Eye diseases Include many noise factors like Images with multiple Sessions, before and after treatment, illumination conditions, Occlusion by eyelids and eyelashes, and high dilated pupils.	For Warsaw V1 ResNet101=99.18%, ResNet50=98.5% GoogleNet=94.26% For Warsaw V2 ResNet50=97.26% ResNet101=96.75 GoogleNet=93.15% For CASIA ResNet101=99% ResNet50=98.49% GoogleNet=93.23
Trokielewicz et al. 2015 [11]	VeriEye, MIRLIN, and Biom-IrisSDK	Warsaw Bio-Base V2/ 1353 images of 219 individuals	Eye diseases	FTR (Obstructions of MIRLIN) =18.36% FTR (Obstructions of OSIRIS) =8.21% FTR (Geometry of VeriEye) =5.13%. The poor performance reason due to the segmentation errors.
Roizenblatt et al. 2004 [30]	Hamming distance	55 eye images	Cataract surgery	There were 6 cases in which the recognition failed.
Minaee and Abdolrashidi 2019 [33]	Pretrained ResNet50	IIT Delhi/ 2240 iris images of 224 Individual	No challenge was mentioned, except few samples differ in size and color distribution.	ACC=95.5% They used the raw images with no segmentation step but a saliency map to recognize the iris ROI utilized. Additionally, Only a few samples were used for testing.

Author	Method	Dataset / Nu. Of Images	Dataset Challenge	Performance/ Remarks
Trokielewicz et al. 2017 [38]	MIRLIN, VeriEye, OSIRIS and IriCore	1353 images of 219 individuals and excluded 11 distinct irises.	Eye diseases	Obstructions-related eye diseases were the main eye conditions that affected the entire iris recognition. The segmentation errors cause a performance drop.
Jia et al. 2022 [42]	ConvNet with a masking approach	ND-IRIS 0405, CASIA-IrisV4-Thousand, and CASIA IrisV4-Lamp/9,578, 1092, and 5321 iris images for training, validation, and test	Noise (Iris recognition under less restrictive environments)	FAR (CASIA Thousand) =10.41%. FAR (CASIA Lamp) =5.8%. FAR (ND-IRIS-0405) =5.49%.

5.3. CONCLUSION

In the iris segmentation step, a novel dynamic circular Hough transform algorithm is applied. Then, a new deep learning-based iris recognition system in the case of eye diseases is presented. While for the recognition part, three different deep learning models learning (GoogleNet, ResNet50, and ResNet101) are utilized using the transfer learning approach. The experiments are applied to three different datasets. The first dataset is the Warsaw Bio-Base V1 which includes 684 iris images with different eye diseases. The second dataset is the Warsaw Bio-Base V2 dataset, including 1793 iris images with more complex eye cases and a larger number of images. Two or three sessions are taken into account through the process of acquiring Warsaw Bio-Base V1 and V2 images. The third dataset is the CASIA iris dataset, consisting of 2639 healthy iris images under specific image conditions, through two sessions for most images.

Experiments are applied through different training scenarios. The proposed scenarios consider different deep learning models, different splitting criteria, colored and grayscale iris images, segmented and original iris images, and transfer learning as two layers of training. The result models are evaluated using many evaluation metrics: training accuracy, validation accuracy, test accuracy, TPR, FNR, PPR, FDR, and training time. The effect of eye diseases on iris segmentation and recognition performance is studied and analyzed. Results proved that in some cases, iris segmentation is affected significantly by eye diseases, especially in cases of mixed diseases, pupil problems, blindness, some retinal detachment, and bloody eye issues. The results also indicate that most eye diseases do not affect iris segmentation when they exist individually, like cataracts, glaucoma, blurry, some lens problems, and some corneal problems.

For the iris recognition part, the eye disease has less effect than the case of iris segmentation. Some eye blindness situations are recognized well. The most influential problem on iris recognition is the eye situation in which the iris is covered, or its structure is changed partially or entirely.

The results show no error recorded for most images acquired during two or three different sessions. The results also prove that most special cases can be included in iris recognition systems without real problems. However, the results also indicate that some other eye problems can affect the iris recognition and must be excluded or treated before using in the biometric systems.

5.4. FUTURE WORK

Next studies can focus on the performance of iris recognition systems in the case of other diseases. Other different deep learning models can be optimized and used for the same aim. Next research can deal with the problem of iris post-mortal effects on the iris recognition systems.

REFERENCES

1. Kakkad, V., Patel, M., and Shah, M., "Biometric authentication and image encryption for image security in cloud framework", ***Multiscale And Multidisciplinary Modeling, Experiments And Design***, 2 (4): 233–248 (2019).

2. Moses, Y., Adini, Y., and Ullman, S., "Face recognition: The problem of compensating for changes in illumination direction", ***Lecture Notes In Computer Science (Including Subseries Lecture Notes In Artificial Intelligence And Lecture Notes In Bioinformatics)***, 800 LNCS (7): 286–296 (1994).

3. Xie, X. and Lam, K.-M., "Face recognition under varying illumination based on a 2D face shape model", ***Pattern Recognition***, 38 (2): 221–230 (2005).

4. Mathematics, A., "STUDY ON THE DISEASES AND DEFORMITIES CAUSING FALSE REJECTIONS FOR FINGERPRINT AUTHENTICATION S.Rajarajan, S.Palanivel , K.R.Sekar, S.Arunkumar", 119 (15): 443–453, ***International Journal of Pure and Applied Mathematics***, (2018).

5. Tan, C. W. and Kumar, A., "Accurate Iris Recognition at a Distance Using Stabilized Iris Encoding and Zernike Moments Phase Features", ***IEEE Transactions On Image Processing***, 23 (9): 3962–3974 (2014).

6. Mayya, A. M. and Saii, M. M., "Iris Recognition Based on Weighting Selection and Fusion Fuzzy Model of Iris Features To Improve Recognition Rate", ***International Journal Of Information Research And Review***, 03: 2664–2680 (2016).

7. Trokielewicz, M., Czajka, A., and Maciejewicz, P., "Iris recognition under biologically troublesome conditions - Effects of aging, diseases and post-mortem changes", ***BIOSIGNALS 2017 - 10th International Conference On Bio-Inspired Systems And Signal Processing, Proceedings; Part Of 10th International Joint Conference On Biomedical Engineering Systems And Technologies, BIOSTEC 2017***, 4: 253–258 (2017).

8. Ravin, J. G., "Iris Recognition Technology (or, Musings While Going through Airport Security)", ***Ophthalmology***, 123 (10): 2054–2055 (2016).

9. Alonso-Fernandez, F. and Bigun, J., "Quality factors affecting iris segmentation and matching", ***Proceedings - 2013 International Conference On Biometrics, ICB 2013***, 0–5 (2013).

10. Trokielewicz, M., Czajka, A., and Maciejewicz, P., "Cataract influence on iris recognition performance", ***Photonics Applications In Astronomy, Communications, Industry, And High-Energy Physics Experiments 2014***, 9290: 929020 (2014)

11. Trokielewicz, M., Czajka, A., and Maciejewicz, P., "Assessment of iris recognition reliability for eyes affected by ocular pathologies", ***2015 IEEE 7th International Conference On Biometrics Theory, Applications And Systems, BTAS 2015***, (2015).

12. Trokielewicz, M., Czajka, A., and Maciejewicz, P., "Database of iris images acquired in the presence of ocular pathologies and assessment of iris recognition reliability for disease-affected eyes", ***Proceedings - 2015 IEEE 2nd International Conference On Cybernetics, CYBCONF 2015***, 495–500 (2015).

13. Omelina, L., Goga, J., Pavlovicova, J., Oravec, M., and Jansen, B., "A survey of iris datasets", ***Image And Vision Computing***, 108: 104109 (2021).

14. "CASIA-IrisV3 Interval, ***Chinese Academy of Science***. http://www.cbsr.ia.ac.cn/english/IrisDatabase.asp. [Accessed 1 12 2020]."

15. Fathee, H. and Sahmoud, S., "Iris segmentation in uncooperative and unconstrained environments: State-of-the-art, datasets and future research directions", ***Digital Signal Processing: A Review Journal***, 118: 103244 (2021).

16. Kaur, B., Singh, S., and Kumar, J., "Robust Iris Recognition Using Moment Invariants", ***Wireless Personal Communications***, 99 (2): 799–828 (2018).

17. Naji, S. A., Tornai, R., Lafta, J. H., and Hussein, H. L., "Iris recognition using localized zernike features with partial iris pattern", ***Communications In Computer And Information Science***, 1183 CCIS: 219–232 (2020).

18. Li, Y. H., Putri, W. R., Aslam, M. S., and Chang, C. C., "Robust iris segmentation algorithm in non-cooperative environments using interleaved residual u-net", ***Sensors***, 21 (4): 1–21 (2021).

19. Trokielewicz, M., Czajka, A., and Maciejewicz, P., "Post-mortem iris recognition with deep-learning-based image segmentation", ***Image And Vision Computing***, 94: 103866 (2020).

20. Sokolova, N., Taschwer, M., Sarny, S., Putzgruber-Adamitsch, D., and Schoeffmann, K., "Pixel-Based Iris and Pupil Segmentation in Cataract Surgery Videos Using Mask R-CNN", ***ISBI Workshops 2020 - International Symposium On Biomedical Imaging Workshops, Proceedings***, 2020–2023 (2020).

21. Agha, S. and Jan, F., "A low complexity Iris localization algorithm for Iris biometrics", ***Multimedia Tools And Applications***, (2022).

22. Malinowski, K. and Saeed, K., "An iris segmentation using harmony search algorithm and fast circle fitting with blob detection", ***Biocybernetics And Biomedical Engineering***, 42 (1): 391–403 (2022).

23. Nachar, R. and Inaty, E., "An effective segmentation method for iris recognition based on fuzzy logic using visible feature points", ***Multimedia Tools And Applications***, 81 (7): 9803–9828 (2022).

24. Daugman, J. G., "High Confidence Visual Recognition of Persons by a Test of Statistical Independence", ***IEEE Transactions On Pattern Analysis And Machine Intelligence***, 15 (11): 1148–1161 (1993).

25. Wildes, R. P., Asmuth, J. C., Green, G. L., Hsu, S. C., Kolczynski, R. J., Matey, J. R., and McBride, S. E., "System for automated iris recognition", ***IEEE Workshop On Applications Of Computer Vision - Proceedings***, 121–128 (1994).

26. Ma, L., Wang, Y., and Tan, T., "Iris recognition using circular symmetric filters", ***Proceedings - International Conference On Pattern Recognition***, 16 (2): 414–417 (2002).

27. Koh, J., Govindaraju, V., and Chaudhary, V., "A robust iris localization method using an active contour model and hough transform", ***Proceedings - International Conference On Pattern Recognition***, 2852–2856 (2010).

28. Francese, R., Frasca, M., and Risi, M., "Are IoBT services accessible to everyone?", ***Pattern Recognition Letters***, 147: 71–77 (2021).

29. Hu, J., Wang, L., Luo, Z., Wang, Y., and Sun, Z., "A Large-scale Database for Less Cooperative Iris Recognition", ***2021 IEEE International Joint Conference On Biometrics, IJCB 2021***, 1–6 (2021).

30. Roizenblatt, R., Schor, P., Dante, F., Roizenblatt, J., and Belfort, R., "Iris recognition as a biometric method after cataract surgery", ***BioMedical Engineering Online***, 3: 1–7 (2004).

31. Pierscionek, B., Crawford, S., and Scotney, B., "Iris recognition and ocular biometrics-the salient features", ***Proceedings - IMVIP 2008, 2008 International Machine Vision And Image Processing Conference***, 170–175 (2008).

32. Aslam, T. M., Shi, Z. T., and Dhillon, B., "Iris recognition in the presence of ocular disease", ***Journal Of The Royal Society Interface***, 6 (34): 489–493 (2009).

33. Minaee, S. and Abdolrashidi, A., "DeepIris: Iris Recognition Using A Deep Learning Approach", ***arXiv***:1907.09380v1 (2019).

34. Hsiao, C. S., Fan, C. P., and Hwang, Y. T., "Design and Analysis of Deep-Learning Based Iris Recognition Technologies by Combination of U-Net and EfficientNet", ***2021 9th International Conference On Information And Education Technology, ICIET 2021***, 433–437 (2021).

35. Omran, M. and Alshemmary, E. N., "An Iris Recognition System Using Deep convolutional Neural Network", ***Journal Of Physics: Conference Series***, 1530 (1): (2020).

36. Karn, P., He, X. H., Zhang, J., and Zhang, Y., "An experimental study of relative total variation and probabilistic collaborative representation for iris recognition", ***Multimedia Tools And Applications***, 79 (43–44): 31783–31801 (2020).

37. Babu, G. and Khayum, P. A., "Elephant Herding with Whale Optimization Enabled ORB Features and CNN for Iris Recognition", Multimedia Tools and Applications, ***Springer US***, 5761–5794 (2022).

38. Trokielewicz, M., Czajka, A., and Maciejewicz, P., "Implications of ocular pathologies for iris recognition reliability", ***Image And Vision Computing***, 58: 158–167 (2017).

39. Soni, A., Patidar, T., Kumar, M. R., Bharath, K. P., Balaji, S., and Rajendran, R., "Iris Recognition using Hough Transform and Neural Architecture Search Network", ***3rd IEEE International Virtual Conference On Innovations In Power And Advanced Computing Technologies, I-PACT 2021***, 1–5 (2021).

40. Borkar, K. and Salankar, S., "IRIS Recognition System", ***2021 IEEE International Conference On Mobile Networks And Wireless Communications, ICMNWC 2021***, (2021).

41. Devi, K., "An Effective Feature Extraction Approach for Iris Recognition System", ***Indian Journal Of Science And Technology***, 9 (1): 1–5 (2016).

42. Jia, L., Shi, X., Sun, Q., Tang, X., and Li, P., "Second-order convolutional networks for iris recognition", ***Applied Intelligence***, (2022).

43. Science, C. and Shah, K. B., "On human iris recognition for biometric identification based on various convolution neural networks", ***Gujarat Technological University*** (2022).

44. Wang, K. and Kumar, A., "Using Dilated Residual Features", ***IEEE Transactions on Information Forensics and Security*** 14 (12): 3233–3245 (2019).

45. Chen, Y., Wu, C., and Wang, Y., "T-Center: A Novel Feature Extraction Approach towards Large-Scale Iris Recognition", ***IEEE Access***, 8: 32365–32375 (2020).

46. Parzianello, L. and Czajka, A., "Saliency-Guided Textured Contact Lens-Aware Iris Recognition", ***Proceedings - 2022 IEEE/CVF Winter Conference On Applications Of Computer Vision Workshops, WACVW 2022***, 330–337 (2022).

47. Okokpujie, K., Noma-Osaghae, E., John, S., and Ajulibe, A., "An Improved Iris Segmentation Technique Using Circular Hough Transform", ***Springer, Singapore*** (2018).

48. Hapsari, R. K., Utoyo, M. I., Rulaningtyas, R., and Suprajitno, H., "Iris segmentation using Hough Transform method and Fuzzy C-Means method", ***Journal Of Physics: Conference Series***, 1477 (2): (2020).

49. Zhuang, F., Qi, Z., Duan, K., Xi, D., Zhu, Y., Zhu, H., Xiong, H., and He, Q., "A Comprehensive Survey on Transfer Learning", ***Proceedings Of The IEEE***, 109 (1): 43–76 (2021).

50. Pan, S. J. and Yang, Q., "A survey on transfer learning", ***IEEE Transactions On Knowledge And Data Engineering***, 22 (10): 1345–1359 (2010).

51. Mohammed Aarif, K. O. and Poruran, S., "OCR-Nets: Variants of Pre-trained CNN for Urdu Handwritten Character Recognition via Transfer Learning", ***Procedia Computer Science***, 171 (2019): 2294–2301 (2020).

52. Yin, X., Yu, X., Sohn, K., Liu, X., and Chandraker, M., "Feature transfer learning for face recognition with under-represented data", ***Proceedings Of The IEEE Computer Society Conference On Computer Vision And Pattern Recognition***, 2019-June: 5697–5706 (2019).

53. Ren, C. X., Dai, D. Q., Huang, K. K., and Lai, Z. R., "Transfer learning of structured representation for face recognition", ***IEEE Transactions On Image Processing***, 23 (12): 5440–5454 (2014).

54. Nirgude, M. A. and Gengaje, S. R., "Iris Recognition System Based on Convolutional Neural Network", ***Springer, Singapore*** (2022).

55. Niu, S., Liu, Y., Wang, J., and Song, H., "A Decade Survey of Transfer Learning (2010–2020)", ***IEEE Transactions On Artificial Intelligence***, 1 (2): 151–166 (2021).

56. Lecun, Y., Bengio, Y., and Hinton, G., "Deep learning", ***Nature***, 521 (7553): 436–444 (2015).

57. Wu, J., "Introduction to Convolutional Neural Networks", ***Introduction To Convolutional Neural Networks***, 1–31 (2017).

58. McCaffrey, J. D., ", “Convolution Image Size, Filter Size, Padding and Stride,” wordpress.", ***[Online] Available: Https://Jamesmccaffrey.Wordpress.Com/2018/05/30/Convolution-Image-Size-Filter-Size-Padding-And-Stride/.***, [Accessed 1 10 2021] .

59. C. Szegedy, W. Liu, Y. Jia, P. Sermanet, S. Reed, D. Anguelov, D. Erhan, V. V. and A. R., "Going Deeper With Convolutions", ***In Proceedings Of The IEEE Conference On Computer Vision And Pattern Recognition, Boston, Massachusetts.***, 1–9 (2015).

60. Wan, S., Liang, Y., and Zhang, Y., "Deep convolutional neural networks for diabetic retinopathy detection by image classification", ***Computers And Electrical Engineering***, 72: 274–282 (2018).

61. K. He, X. Zhang, S. R. and J. S., "Deep residual learning for image recognition", ***In Proceedings Of The IEEE Conference On Computer Vision And Pattern Recognition, Las Vegas, NV, USA.***, 770–778 (2016).

62. Khan, A., Sohail, A., Zahoora, U., and Qureshi, A. S., "A Survey of the Recent Architectures of Deep Convolutional Neural Networks", Artificial Intelligence Review, ***Springer Netherlands***, 5455–5516 (2020).

63. Maeda-Gutiérrez, V., Galván-Tejada, C. E., Zanella-Calzada, L. A., Celaya-Padilla, J. M., Galván-Tejada, J. I., Gamboa-Rosales, H., Luna-García, H., Magallanes-Quintanar, R., Guerrero Méndez, C. A., and Olvera-Olvera, C. A., "Comparison of convolutional neural network architectures for classification of tomato plant diseases", ***Applied Sciences (Switzerland)***, 10 (4): (2020).

64. Internet: Mathworks.com, "“googlenet.Html,” Mathworks, .", ***available: https://www.mathworks.com/help/nnet/ref/googlenet.html. .*** (2021).

65. Internet: Mathwork.com, "“resnet50,” Mathwork, .", ***available: https://www.mathworks.com/help/deeplearning/ref/resnet50.html;jsessionid=0997fbde6e724213cdf6a294bfa4.*** (2021).

66. "Biometrics and Machine Learning Group, “Warsaw-Bio-Base-Disease-Iris v1.0,”, ***Warsaw University of Technology,*** (2015)." .

67. "Biometrics and Machine Learning Group, “Warsaw-Bio-Base-Disease-Iris v2.1,”, ***Warsaw University of Technology,*** (2015)." .

68. Spaan, C., "The recognition of hand gestures by evaluating micro-vibrations using a single wrist-worn highly sampled IMU", ***University of Twente,*** (2018).

69. Internet: Mathwork, "Mathwork, “Assess Classifier Performance,” Mathwork, 2020. [Online].", **available: https://www.mathworks.com/help/stats/assess-classifier-performance.html** .

APPENDIX A.

WARSAW DATASET SEGMENTATION RESULTS

Table Appendix A.1 True and False iris segmentation results (WARSAW V1).

Left Eye				Right Eye			
Person ID	**Medical description - left eye**	**TSR**	**FSR**	**Person ID**	**Medical description - left eye**	**TSR**	**FSR**
0	pseudophakic since 2009, glaucoma, condition after acute glaucoma, iridectomy, ExPress implant placed in 2010, removed in 2011, trabeculectomy, capsulotomy, wide and unresponding pupil		6	0	cataract, glaucoma, iridotomy	6	
1	cataract	7		1	pseudophakic since 2012	8	
2	pseudophakic since 2012	5		2	cataract	7	
3	cataract	7		3	healthy	7	
4	cataract	7		4	cataract	3	
5	cataract	6		6	cataract, diabetic retinopathy	8	
6	cataract	8		7	pseudophakic since 2007, glaucoma, after acute glaucoma condition, iridotomy	8	
7	glaucoma, after acute glaucoma condition, iridotomy	7		8	cataract	6	
8	cataract	7		11	cataract, oval pupil after acute glaucoma condition, iridotomy	14	
11	cataract, after acute glaucoma condition, iridotomy, distorted pupil, posterior synechiae	8	6	12	cataract	7	
12	cataract	5	2	14	healthy	6	
14	retinal detachment	6		15	incipient cataract	7	
15	cataract after retinal detachment surgery with silicon oil	7		18	retinal detachment (with silicon oil)		8
18	healthy	7		19	cataract	9	
19	cataract	9		20	cataract	7	
20	cataract, corneal haze (at 1 o'clock)	6	1	22	cataract	7	
22	cataract	2		23	pseudophakic since 2012	7	
23	cataract	7		24	cataract, glaucoma	8	
24	incipient cataract, glaucoma	8		25	healthy	6	
25	pseudophakic since May 2013, after trauma, after	4		26	healthy	6	

Left Eye				Right Eye			
Person ID	Medical description - left eye	TSR	FSR	Person ID	Medical description - left eye	TSR	FSR
	retinal detachment surgery with the removal of the misplaced lens (earlier)						
27	anterior synechiae	7		27	anterior synechiae	6	
28	post-trauma cataract after removing a metal object from inside the eyeball, anterior synechiae, iris scarring (at 6 o'clock)	6	1	29	cataract	7	
29	pseudophakic since Oct 2013	6		31	cataract	5	
30	pseudophakic since 2012	6		33	cataract, glaucoma, oval pupil after acute glaucoma condition, iridotomy	5	
31	cataract	5		35	uveitis, secondary glaucoma, cataract, blindness		26
33	pseudophakic since 2001, after 2006 trabeculectomy, glaucoma	4		36	cataract, condition after central retinal artery embolism in 2006	6	
34	cataract	4		37	cataract	6	
35	uveitis, secondary glaucoma, cataract, iris sutures, small pupil	26		39	glaucoma, pseudophakic since 2009, session 1 and 2: routine examination	11	
36	cataract	5		41	secondary cataract, pseudophakic since 2011, posterior chamber implant, after posterior and anterior capsulotomy		
37	cataract	6		42	pseudophakic since Jul 2013, after retinal detachment surgery (with silicon oil, Jul 2013), distorted pupil	6	
1042	condition after iris trauma, iris defect, corneal limbus injury	7					
38	pseudophakic	5		43	session 1: post-traumatic cataract, session 2: after pupil dilation, session 3: pseudophakic, oval, unresponding pupil	19	

39	glaucoma, cataract, condition after retinal artery embolism, after two trabeculectomies in 1986 and 2011, iris dialysis, blindness, session 1 and 2: routine examination		10	45	cataract, iris nevus (7 o'clock), posterior synechiae, curled up edges of the iris	6	
40	session 1: cataract, posterior synechiae due to chronic uveitis, session 2: pseudophakic after cataract surgery, membrane in the iridocorneal angle	13		46	pseudophakic, after retinal detachment surgery (with silicon oil) in 2013	9	
42	incipient cataract, corneal haze	6		47	posterior synechiae	6	
45	pseudophakic since 2012, iris defects (12 o'clock and 2 o'clock)	6		48	rubeosis, synechiae	6	1
46	incipient cataract	7		51	anterior chamber lens implant	8	
48	healthy	7		52	silicon oil in the anterior chamber	6	
52	healthy	6		53	posterior synechiae	4	4
53	healthy	8		54	posterior synechiae, distorted pupil	7	
54	healthy	7		55	corneal haze	7	
55	corneal vascularization	7		57	healthy	11	
56	after corneal transplant, iris defect	7		59	glaucoma, pseudoexfoliation syndrome, opacified	6	
58	corneal vascularization	6		61	pseudophakic	6	
59	glaucoma, after 2006 trabeculectomy, cataract, iridectomy	6		63	healthy	14	
61	retinal detachment, cataract	5		1042	healthy	7	

Table Appendix A.2 True and False iris segmentation results (WARSAW V2).

Left Eye				Right Eye			
Person ID	**Medical description - left eye**	**TSR**	**FSR**	**Person ID**	**Medical description - left eye**	**TSR**	**FSR**
0	pseudophakic , glaucoma, iridectomy, ExPress implant, trabeculectomy, capsulotomy, wide and unresponding pupil, pupil dilation	0	6	0	cataract, glaucoma, iridectomy, phacoemulsification	6	
1	cataract, phacoemulsification	7		1	pseudophakic	8	
2	pseudophakic	7		2	cataract, phacoemulsification	7	
3	cataract	7		3	healthy	7	
4	cataract, phacoemulsification	7		4	cataract	3	
5	cataract	7		5	cataract, phacoemulsification	10	
6	cataract	8		6	cataract, diabetic retinopathy, pseudophakic	8	
7	glaucoma, acute glaucoma, iridotomy, cataract, pseudophakic	8		7	pseudophakic, glaucoma, after acute glaucoma condition, iridotomy	8	
8	cataract	7		8	cataract	7	
11	cataract, acute glaucoma, iridotomy, distorted pupil, posterior synechiae	8	6	11	cataract, oval pupil after acute glaucoma condition, iridotomy	14	
12	cataract, pseudophakic	5	2	12	cataract	7	
14	retinal detachment	6		14	healthy	6	
15	cataract, retinal detachment surgery with silicon oil, pseudophakic	7		15	incipient cataract	7	
16	pseudophakic, glaucoma	20		16	glaucoma, cataract, pseudophaki	23	
17	healthy	14	1	17	cataract, pseudophakic	12	3
18	healthy	7		18	retinal detachment		8
19	cataract	9		19	cataract, pseudophakic	9	
20	cataract, corneal haze	6	1	20	cataract, pseudophakic	7	
21	phacoemulsification, IOL PC	6		21	pseudophakic	5	
22	cataract	6		22	cataract, pseudophakic	7	
23	cataract, pseudophakic	7		23	pseudophakic	7	

24	incipient cataract, glaucoma	8		24	cataract, glaucoma	8	
25	pseudophakic, trauma, retinal detachment surgery	6		25	healthy	6	
26	aphaki, posterior and anterior synechiae, retinal detachment surgery, secondary cataract	6		26	healthy	6	
27	anterior synechiae	7		27	anterior synechiae	6	
28	post-trauma cataract, anterior synechiae, iris scarring	6	1	28	healthy	1	
29	pseudophakic	7		29	cataract	7	
30	pseudophakic	6		30	cataract	6	
31	cataract	6		31	cataract	6	
32	glaucoma, pseudoexfoliation syndrome, iridotomy, incipient cataract	13		32	cataract, glaucoma, pseudoexfoliation syndrome, iridotomy	13	
33	pseudophakic, trabeculectomy, glaucoma	6		33	cataract, glaucoma, oval pupil, acute glaucoma condition, iridotomy	5	
34	cataract	7		34	cataract	6	1
35	uveitis, secondary glaucoma, cataract, iris sutures, small pupil, ECCE + IOL PC + iris correction	26		35	uveitis, secondary glaucoma, cataract, blindness		26
36	cataract	6		36	cataract, central retinal artery embolism	6	
37	cataract	6		37	cataract, pseudophakic	6	
38	pseudophakic	6		38	cataract, phacoemulsification with IOL PC	6	
39	glaucoma, cataract, retinal artery embolism, iris dialysis, blindness	0	10	39	glaucoma, pseudophakic	12	
40	cataract, posterior synechiae, pseudophakic membrane in the iridocorneal angle	13		40	healthy	13	

41	blurred lens	7		41	secondary cataract, pseudophakic, posterior chamber implant, posterior and anterior capsulotomy	7	
42	incipient cataract, corneal haze	6		42	pseudophakic, retinal detachment surgery, distorted pupil	6	
43	healthy	19		43	post-traumatic cataract,pupil dilation, pseudophakic, oval, unresponding pupil	19	
45	pseudophakic, iris defects	6		45	cataract, iris nevus, posterior synechiae, curled up edges of the iris	6	
46	incipient cataract	7		46	pseudophakic, retinal detachment surgery	10	
47	iridectomy	6		47	posterior synechiae, iridotomy	6	
48	phacoemulsification, IOL PC	7		48	retinal detachment, aphakia, rubeosis, posterior synechiae, vascularization	6	1
51	healthy	6		51	after post-traumatic cataract, anterior chamber lens implant, heterotropia surgery	8	
52	healthy	6		52	retinal detachment surgery, pseudophakic, corneal haze, silicon oil in the anterior chamber	6	
53	healthy	8		53	retinal detachment surgery, pseudophakic, glaucoma, posterior synechiae, iridotomy, iris bombe, cataract	4	4
54	cataract	7		54	posterior synechiae, distorted pupil	7	
55	corneal vascularization, scarring, and haze	13		55	corneal haze	13	
56	corneal transplant, iris defect, corneal granular dystrophy	7		56	corneal transplant, granular corneal dystrophy	7	
57	corneal ulcer, haze, minor vascularization, pharmacological pupil dilation	11		57	healthy	11	
58	corneal vascularizationand haze, anterior synechiae, posterior synechiae, cataract	6		58	cataract	6	

59	glaucoma, trabeculectomy, cataract, iridectomy, phacoemulsification + IOL	6		59	glaucoma, pseudoexfoliation syndrome, opacified	6	
60	iridescent lens	13		60	cataract, phacoemulsification with IOL	12	1
61	after retinal detachment surgery, cataract, phacoemulsification + IOL	6		61	phacoemulsification + IOL, capsulotomy	6	
62	nuclear cataract	19		62	nuclear cataract, cataract surgery	17	2
63	cataract, secondary glaucoma, rubeosis, posterior synechiae, Express implant, trabeculectomy, corneal sweeling and haze	8	12	63	glaucoma, rubeosis	20	
64	corneal edema, iridotomy, posterior synechiae, acute glaucoma, phacoemulsification with trabeculectomy, iris pigment	17		64	cataract, glaucoma, corneal edema, iridotomy, posterior synechiae, acute glaucoma, blood in the anterior chamber, trabeculectomy, minor corneal sweeling	19	
65	corneal vascularization, swelling cataract, curled up edges of the iris, glaucoma, narrow iris	0	6	65	healthy	6	
66	glaucoma, phacoemulsification + IOL PC, iridotomy	12		66	glaucoma, pseudophakic, narrow horizontal pupil, lens material residue, iridotomy	12	
67	trabeculectomy, blood in the anterior chamber	6		67	trabeculectomy	6	
68	post-trauma, corneal inflammation, posterior synechiae	6		68	corneal defect and vascularization, cataract, corneal ulcer	6	
69	posterior synechiae, cataract	11		69	iridectomy	12	
70	after vitrectomy with oil, aphakia	1		70	retinal detachment, vitrectomy with oil, aphakia, distorted pupil, anterior synechiae	3	1

71	eye trauma and post-traumatic cataract, iris defect, lens implant with iris diaphragm	3	10	71	healthy	15	
72	healthy	6		72	retinalo detachment, vitrectomy with oil, secondary glaucoma, diabetic retinopathy, tabeculectomy, rubeosis iridis, posterior synechiae, oil and blood in the anterior chamber	6	
73	corneal ulcer, swelling, haze, posterior synechiae	6		73	healthy	6	
74	phacoemulsification with vitrectomy, lens implantation, retractor scars on the iris	6		74	phacoemulsification + IOL	6	
75	aphakia, glaucoma, distorted pupil	7		75	aphakia	7	
76	after trabeculectomy, iridectomy, cataract	6		76	trabeculectomy, iridectomy, blood in the anterior chamber	6	
77	healthy	7		77	rubeosis	7	
78	eye trauma, cornea injury suture, aphakia, corneal scarring	5	1	78	healthy	7	
79	intumescent cataract, acute glaucoma condition, aphakia, ECCE	5	1	79	cataract, iridotomy	6	
80	healthy	7		80	blunt trauma, blood spill into the anterior chamber	7	
81	healthy	6		81	narrow pupil with symphisis, iris nevus	4	1
82	glaucoma, pemphigoid, trabeculectomy, pseudophakic, corneal haze, vascularization	3	4	82	glaucoma, pemphigoid, trabeculectomy, pseudophakic, corneal haze, vascularization	3	
83	healthy	0	7	83	hypermature cataract		5
84	glaucoma, corneal haze, childhood ulcer	6		84	glaucoma, blurry	6	
85	sweeling and haze in the cornea, keratopathy, iris defect at the top, aphakia	0	5	85	iridotomy, posterior synechiae, blurry	5	
86	corneal ulcer, sediments, posterior synechiae	6		86	healthy	6	

87	after trabeculectomy, pseudophakic, iridectomy, iris suture	7		87	trabeculectomy, pseudophakic, corneal suture, iridectomies, capsulotomy, the upper part of the lens implant located in front of the iris	6	1
88	blurry	5		88	pseudophakic, trabeculectomy, corneal vascularization, cyst, iris suture, anterior synechiae	6	
89	removal of the conjunctiva hypertrophy near the corneal edge, amnion membrane transplantation, cataract	0	6	89	cataract, posterior synechiae, distorted pupil	6	
90	an intraocular foreign object, vitrectomy with oil and lens removal, corneal injury and sutures, oil in the anterior chamber, aphakia	10	1	90	healthy	11	
91	eye trauma, circular corneal haze, iris defects, lens implant with iris diaphragm, glaucoma	7		91	glaucoma, pseudophakic	7	
92	eye trauma, sclera suture, aphakia, anterior synechiae, corneal scarring, severely distorted pupil	4	1	92	healthy	5	
93	healthy	8		93	chemical (gas) burn to the cornea	4	1
94	healthy	6		94	intraocular foreign body in the cornea	6	
95	retinal detachment surgery, blindness, keratopathy, corneal haze	0	5	95	cataract	5	
96	retinal detachment surgery, aphakia, iridotomy, vitrectomy with oil replacement, rubeosis, oil in the anterior chamber, iridectomy	2		96	retinal detachment surgery, aphakia, congenital cataract, anterior synechiae, distorted pupil	4	2
97	trauma, corneal haze	0	6	97	healthy	6	

98	phacoemulsification and IOL PC, lens implant behind the iris, local iris atrophy	6		98	ECCE and IOL AC, anterior chamber lens implant	6	
99	eye trauma, ECCE, and IOL AC, retinal detachment surgery, vitrectomy with oil, trabeculectomy, corneal transplant with the removal of IOL AC, corneal haze, vascularization, cysts	0	7	99	healthy	7	
100	blurry	6	0	100	witrectomy with oil, blindness, keratopathy, rubeosis, posterior synechiae	0	6
101	vitrectomy with oil, aphakia, perforation in the lens capsul	6		101	glaucoma, cataract	6	0
102	embolism, corneal swelling, rubeosis, opacified lens, glaucoma	12		102	glaucoma, incipient cataract, opacified lens	12	
103	glaucoma, ECCE and IOL PC, iris suture, anterior synechiae	5	1	103	glaucoma, trabeculectomy, ECCE, IOL PC, capsulotomy, anterior synechiae, lens implant	6	
104	retinal detachment surgery removal of episcleral cerlage, cataract, posterior synechiae, distorted pupil	4	2	104	cataract	7	
105	corneal haze, opacification after corneal ulcer, corneal vascularization	3		105	cataract, phacoemulsification + IOL PC	3	
106	healthy	13		106	eye trauma, corneal laceration suture, blood in the anterior chamber		13
107	healthy	4	1	107	retinal detachment, vitrectomy with oil, aphakia, iridotomy, oil in the anterior chamber, glaucoma	4	1
108	phacoemulsification+ IOL PC, internal prolapse, distorted pupil, lens implant partially visible	6		108	healthy	6	

109	healthy	5	1	109	blunt wood trauma to the eye, blood in the anterior chamber	6	
110	secondary glaucoma, vitrectomy, oil in the anterior chamber, pseudophakia	6		110	blindness, aphakia, vitrectomy, band keratopathy of the cornea	2	4
111	retinal detachment and vitrectomy with oil, pseudophakic oil in the anterior chamber	4	1	111	healthy	5	
112	blood in the anterior chamber, corneal swelling, and vascularization	0	6	112	glaucoma	6	
113	corneal ulcer	6		113	healthy	6	
114	glaucoma, phacoemulsification +IOL PC, opacification of the cornea	8		114	glaucoma, cataract	4	
115	incipient cataract	5	1	115	swelling cataract, ECCE (with prolapse of the vitreous humor into the anterior chamber and bleeding)		8
116	ECCE and IOL PC, pseudophakic, capsulotomy	4	2	116	ECCE and IOL PL, pseudophakic, capsulotomy, oval pupil	2	4
117	posterior synechiae, iris pigment	8		117	iris pigment	5	
1042	iris trauma, iris defect, corneal limbus injury	7		1042	healthy	7	
1090	uveitis, glaucoma, phacoemulsification with iris correction, aphakia, retinal detachment, fibers	2	5	1090	opacified lens	7	
1111	healthy	7		1111	eye trauma, corneal suture, post-traumatic bleeding into the anterior chamber, anterior chamber irrigation	7	

RESUME

Abbadullah .H Saleh received a bachelor's degree in computer engineering from the University of Dijllah, Baghdad, Iraq, in 2010. He has long experience in his specialty, more than nine years. In 2010, he was engaged as a member of the IT Technical Committee. In 2015, he was the Head of the GIS Unit. In 2016, he was the Manager of the Pharmaceutical Company, responsible for many sectors, one of them is with the Designing and Development. In 2020, he moved to Turkey to pursue a master’s degree from the Faculty of Engineering, Karabuk University.